USING THE DYNAMIC GAS DISENGAGEMENT TECHNIQUE TO CHARACTERIZE GAS/LIQUID CONTACTING IN MICROBUBBLE-AERATED COLUMNS

by

Rong Leng

Submitted in partial fulfilment of the requirements
for the degree of MASTER OF APPLIED SCIENCE

at

Dalhousie University
Halifax, Nova Scotia
December 2021

TABLE OF CONTENTS

LIST OF TABLES

LIST OF FIGURES

ABSTRACT

Gas-liquid contacting plays a significant role in the chemical, petrochemical, mineral processing, and biochemical industries, where it is encountered in a wide range of operations. Generally, high volumetric mass transfer coefficients (k_La) are required to achieve better performance in such operations. Unfortunately, the contaminants present in virtually all natural and industrial streams result in lowering k_L values that are only a fraction of their original value in clean waters. This situation can be partially compensated for by using fine bubbles that generate large specific interfacial contact areas of contact between the phases. This approach is widely used to intensify multiphase operations. Regrettably, the techniques usually used to measure bubble size distributions, BSD, and the associated specific interfacial contact areas do not perform well for microbubble systems with large gas holdups and interfacial areas. An advanced version of the dynamic gas disengagement technique (often used to obtain a crude two-class approximation of the BSD) was therefore developed. It is capable of generating relatively reasonable and reproducible estimates of the fine BSDs and the ensuing large interfacial contact area encountered in microbubble-aerated columns.

This investigation was conducted using a pilot-scale bubble column, and contaminated systems exhibiting a wide range of coalescence-retarding characteristics were used to ensure the relevance of the findings to industrial practice. Microbubbles were generated using an innovative adjustable dual-phase venturi (ADPV) sparger operating over a broad range of conditions. It can also uninterruptedly alter the quality of the dispersion, thereby meeting the process control needs. The newly developed advanced DGD data analysis approach was applied to determine the BSDs prevailing in the two hydrodynamic regions observed in microbubble-aerated columns (the sparger region and that across the column). It is based on the use of several models describing the drag forces acting on a single bubble, combined with those accounting for the interaction between adjacent bubbles, to obtain highly-reproducible estimates of several multiphase characteristics (e.g., Φ_G, d_{10}, d_{20}, d_{30}, d_{32}, d_{43}, a, N_B).

This technique was used to successfully analyze 313 experimental runs with relatively high reproducibility. These experiments covered gas holdups varying between 0.2 - 35 % and estimated Sauter mean bubble diameter varying between 140 and 2,400 microns. Although this approach is somewhat limited in providing accurate values for the gas/liquid dispersion characteristics, most of these uncertainties disappear when addressing the relative changes achieved by varying operating and design parameters. As reported by many previous investigators, the estimated BSDs encountered in the microbubble-aerated column closely fit the Log-Normal, with the mean and variance of the distribution being affected by the system's physical properties and operating conditions of the gas/liquid contactor.

Finally, the proposed approach for intensifying gas/liquid contacting was found to be capable of generating interfacial areas as high as 5,470 m^2/m^3 and bubble population densities as high as $7.4*10^7$ m^{-3} in the region close to the sparger. Somewhat smaller values were observed in the whole column.

LIST OF ABBREVIATIONS AND SYMBOLS USED

A	Cross sectional area of flow	m^2
a	Specific interfacial area of contact between gas and liquid	m^2/m^3
Ar	Archimedes Number, $= \frac{{d_b}^3 {\rho_L}^2 g}{{\mu_L}^2}$	----
C_D	Drag coefficient of single bubble	----
C_{DSW}	Drag coefficient of bubble swarms	----
C_{SDS}	Liquid-phase SDS concentration	ppm
D	Diameter	mm
d_{10}	Number-mean bubble diameter	μm
d_{20}	Surface-mean bubble diameter	μm
d_{30}	Volume-mean bubble diameter	μm
d_{32}	Sauter mean diameter of bubbles	μm
d_{43}	De Brouke, or Volume-weighed mean bubble diameter	μm
d_B	Bubble diameter	μm
Eo	Eötvös number $= \frac{g(\rho_L - \rho_G){d_b}^2}{\sigma}$	----
g	Acceleration due to gravity	m/s^2
H_{Dis}	Gas-liquid dispersion height in the column (from two measuring points of the differential pressure sensor)	mm
k_La	Volumetric mass transfer coefficient of the gas/liquid dispersion	s^{-1}
L_{Th}	Throat length	mm
Mo	Morton number, $= \frac{g{\mu_L}^4(\rho_L - \rho_G)}{{\rho_L}^2 \sigma^3}$	----
N_B	Bubble population density	$1/m^3$
N	Number of bubble size classes used in the DGD analysis	----

N_{DGD}	Number of DGD points	----
$n_{1initial}$	Point to start the linear fit at the first disengagement time interval	----
$n_{1linest\_start}$	Number of points initially included in the linear fit	----
P	Absolute pressure	kPa
Q_G	Volumetric gas flow rate	L/min
Q_L	Volumetric liquid flow rate	L/min
Q_{LSp}	Volumetric liquid flow rate fed to the sparger	L/min
Re	Reynolds number, $= \frac{\rho_L U_s \mathrm{D}}{\mu_L}$	----
t_{SS}	Time allocated for collecting steady state data	s
t_0	Time at which gas feed is shut-off and DGD data collection starts	s
$t_{0Pseudo}$	Pseudo start time of the DGD region	s
t_1	Time at the end of the disengagement time interval 1	s
t_F	Final time boundary for the DGD data to be analysed	s
t_j	Time at the end of the disengagement time interval j	s
t_{LL}	Time at which the first point is below ΔP_{LL}	s
t_{LLE}	Time at which the first point is below ΔP_{LLE}	s
$\bar{U}_{LD}$	Superficial downward liquid velocity during the gas disengagement	m/s
U_{LDj}	Superficial downward Liquid velocity in disengagement time interval j	m/s
U_G	Superficial gas velocity at mid-height column conditions	m/s
$\bar{U}_{RBSW}$	Cross-sectional-average rise velocity of bubble swarms	m/s
$\bar{U}_{RBSWij}$	Cross-sectional average swarm rise velocity of bubble size class i in disengagement time interval j	m/s

$\bar{U}_{RBSWj}$	Cross-sectional average swarm rise velocity of bubbles in disengagement time interval j,	m/s
$\bar{U}_{SBSW}$	Cross-sectional average slip velocity of bubble swarms,	m/s
U_{TBSG}	Cross-sectional average terminal rise velocity of a single bubble	m/s
V	Volume	mm^3
$\dot{V}_G$	Volumetric gas flow during the gas disengagement	m^3/s
$\dot{V}_L$	Volumetric liquid flow during the gas disengagement	m^3/s
We	Weber number,$= \frac{\rho_L {V_T}^2 d_B}{\sigma}$	----
X_j	Fraction of disengagement time interval j corresponding to the entire DGD region	----

SUBSCRIPTS

Avg	Average
B	Bubble
C	Column
Disp	Dispersion
d	Downward
Dv	Divergent
G	Gas
Gap	Gap between sparger inner core and outer shell
Geo	Geometric
glob	Global
Hd	Hydraulic
i	Number of bubble size classes used in the DGD analysis
InCo	Inner Core

j	Number of disengagement time intervals used in the DGD analysis
L	Liquid
Loc	Local
Max	Maximum
Min	Minimum
OuSh	Outer Shell
Resid	Residual
S	Slip; Superficial
SS	Steady state
SW	Swarm
SG	Single
Sp	Sparger
SR	Sparger region
Sp2	Location 2 of the sparger
Sp3	Location 3 of the sparger
Sp4	Location 4 of the sparger
SpecLoc	Specified Location at any place in the sparger
Th	Throat
TL	Total
T	Terminal
V	Venturi

GREEK SYMBOLS

σ_L	Static surface tension of liquid	mN/m
μ_L	Liquid viscosity	Pa.s

Γ_G	Gibbs surface excess	mol/m^2
Γ_L	Surface Excess (Long-Term Approximately)	mol/m^2
Π	Surface pressure	mN/m
ΔP	Pressure difference	Pa
ΔP_{Sp}	Pressure drop across the sparger	kPa
ΔP_{LL}	Lower limit of the differential pressure sensor	Pa
ΔP_{LLE}	Experimentally-estimated lower limit of the differential pressure sensor	Pa
λ	Drag correction factor (accounting for the effect of adjacent bubbles)	----
ρ_G	Gas density	kg/m^3
ρ_L	Liquid density	kg/m^3
Φ_G	Gas holdup	% or –
Φ_{GC}	Gas holdup generated throughout the column	% or –
Φ_{Gglob}	Global gas holdup	% or –
Φ_{GLoc}	Local gas holdup	% or –
Φ_{GR}	Gas holdup in riser	% or –
Φ_{GSS}	Gas holdup at steady-state section	% or –
Φ_{GSp}	Gas holdup generated at sparger region	% or –
$\bar{\Phi}_{GC}$	Cross-sectional average gas holdup in the column	% or –
$\bar{\Phi}_{Gj}$	Cross-sectional average gas holdup in disengagement time interval j (including the contribution of all bubble size classes)	% or –
$\bar{\Phi}_{Gij}$	Cross-sectional average gas holdup in disengagement time interval j, corresponding to bubble size class i	% or –

$\bar{\Phi}_{\mathrm{Gi}}$	Cross-sectional average overall holdup contributed by bubble size class i (including all disengagement time intervals)	% or –

ABBREVIATIONS

ADPV	Adjustable dual-phase venturi
BSD	Bubble size distribution
CDF	Cumulative density function
CFD	Computational fluid dynamics
CI	Confidence interval
DGD	Dynamic gas disengagement
DP1	Differential pressure sensor for the measurements throughout the column
DP2	Differential pressure sensor for the measurement at sparger region
ERT	Electrical resistance tomography
N/A	Not available
PDF	Probability density function
SDS	Sodium dodecyl sulphate

ACKNOWLEDGEMENTS

I want to express my deep appreciation and gratitude to my research supervisor, Dr. A.M. Al Taweel, for his extensive guidance, strong encouragement, limitless patience, and criticism throughout the entire research. His enthusiasm and rigorous academic attitude motivated me to work hard, progress, and overcome difficulties during this research.

I am also grateful to Dr. G. Mazzanti for his help and guidance on the computation and program design of the new methodology developed for extracting BSDs from the experimental results and to Dr. A. Donaldson for his help and support regarding the instrumentation and software of the experiments. I wish to thank Dr. A. Ghanem, Dr. M. Walsh for their willingness to serve as the supervisory committee members

In addition, I would also like to acknowledge the assistance provided by Mr. R. Dube in building the experimental setup, Mr. S. MacKinnon for assistance with electrical and LabView software issues, Ms. D. Suresh in running the experiments and collecting the data. Furthermore, I greatly appreciate my colleagues, Mr. A.O. Idhbeaa, who worked with me as a group in commissioning and testing the experimental setup as well as designing and running the experiments. I would also like to thank all the faculty members and staff at the chemical engineering department for their help and cooperation.

The financial support from NSERC, Mitacs, and Dalhousie University, which make this work possible, is gratefully acknowledged. Moreover, many thanks to BC Research Inc. and Alpha Tau Ltd., who offered me internship opportunities and allowed me to gain experience with the industry.

Finally, special thanks are expressed to all my colleagues for their support, help, and companionship. I am also highly indebted to my parents, Mr. C. Leng and Mrs. Y. Gao, my sister, Mrs. N. Leng, for their love and support.

CHAPTER 1 INTRODUCTION

Gas-liquid contacting plays a significant role in the chemical, petrochemical, mineral processing, and biochemical industries, where it is encountered in a wide range of operations (absorption, distillation, wastewater treatment, fermentation, blood oxygenation, bio-reactions, heavy oil upgrading, etc.) [Anastasiou et al., 2010; Fei et al., 2014; Yasin et al., 2015]. Among the various gas-liquid contactor types, bubble column (BC) is one of the most commonly-used reactor types because of the many performances and operational advantages [Jin et al., 2013; Besagni & Inzoli, 2017; Adetunji & Rawatlal, 2018]:

- Simple construction and the absence of moving parts,
- Low energy consumption in the column,
- Relatively high mass transfer rate (large contact area between liquid & gas),
- High thermal stability,
- Relatively good but mild mixing,
- Economic consideration (low capital, maintenance & operating cost).

Generally, high volumetric mass transfer coefficients (k_La) are required to achieve better performance for the operations in bubble columns. Unfortunately, the contaminants present in virtually all natural and industrial streams result in lowering the value of the liquid side mass transfer coefficient, k_L, to a fraction of their original value in clean waters [Vasconcelos et al., 2002], a situation that can be partially compensated for by generating large specific interfacial area of contact between the phases, *"a"*. Moreover, the use of fine bubbles has been reported to be able to intensify multiphase operations in many applications, such as flotation operations. The grade/recovery performance of selective flotation can be significantly enhanced with the use of fine bubbles [Rulyov et al., 2018; Zhou et al., 2020]. Regrettably, the techniques usually used to measure bubble size distributions (BSDs) and the associated specific interfacial contact areas in pneumatically-agitated columns do not perform well for microbubble systems with large gas holdups [Luo et al., 1996; Boyer et al., 2002; Khalili et al., 2018]. Moreover, many non-invasive techniques are quite complicated and costly. It is, therefore, necessary to find a simple and easy-to-use technique for estimating BSDs for fine bubbles at high holdups and interfacial areas.

The dynamic gas disengagement technique (DGD) is traditionally used to estimate average bubble size or obtain a crude approximation of the BSD (reported usually by 2 to 3 classes, namely small and large bubbles and small, medium, large bubbles, respectively) [Patel et al., 1989; Lee et al., 1999; Krishna et al., 2001]. The objective of this investigation is, therefore, to develop an advanced DGD technique, which can provide relatively reasonable and reproducible estimates of the BSDs and the ensuing hydrodynamic parameters (various mean bubble diameters and interfacial contact area) encountered in microbubble-aerated columns. The data collection and analysis systems were designed as automatized as possible, and the investigation was conducted under a wide range of conditions to test the ability of this advanced DGD technique.

CHAPTER 2 CHARACTERIZING GAS/LIQUID CONTACTING: PREVIOUS INVESTIGATIONS

2.1 Methods/Techniques for Characterizing Gas/Liquid Contacting and Measuring Bubble Sizes

Several techniques have been used to characterize gas-liquid contacting. They can be classified as invasive techniques and non-invasive techniques. Each of these techniques has its advantages and disadvantages and can therefore be advantageously used in various applications based on the specific requirements. However, the measurements obtained from some invasive techniques like probe techniques may suffer from the probe's interference with the internal flow conditions, and the effectiveness of most of these techniques is limited to gas holdups (Φ_G) < 10-20 % [Macchi et al., 2001]. Furthermore, they are costly, complicated, laborious, and time-consuming, especially when only global information is needed. [Luo et al., 1996, Khalili et al., 2017].

The non-invasive techniques, such as photographic method, light attenuation, phase doppler velocimetry, were found to be not suitable for assessing the bubble size distribution encountered in flotation columns, and it was necessary to rely on a combination of continuous sampling and ex-situ image analysis in order to properly control the characteristics of the gas/liquid dispersion encountered in such devices [Rodrigues & Rubio, 2003; Vadlakonda & Mangadoddy 2017]. Similar difficulties are encountered in bioreactors where their productivity is usually limited by mass transfer limitations in the case of sparingly soluble gases. Moreover, many of these techniques need to be used in transparent columns. It is, therefore, desirable to find an accurate and easy-to-use technique for the in-situ characterization of gas/liquid dispersion, particularly those under process intensification conditions where high volumetric concentrations of finely-dispersed bubbles are often used [Utikar and Ranade, 2017].

Compared to the other non-invasive techniques discussed above, the dynamic gas disengagement technique, DGD, meets many of these requirements and is relatively cheap, safe, and easy to use, particularly under elevated gas holdup conditions. Unfortunately, it can be very laborious unless special data analysis approaches are used. It typically provides the only very crude characterization of gas/liquid dispersions (e.g., the gas holdup fraction of coarse and fine bubbles). This investigation was therefore undertaken to develop methodologies and algorithms that can enable for automating the conduct of such technique and enhancing its ability to characterize fine gas/liquid dispersions properly.

2.2 Previous Experience with the DGD Technique

Over the past 30 years, the dynamic gas disengagement (DGD) technique has been widely used to characterize gas/liquid dispersions (gas holdups, bubble rise velocities, BSDs, and the resulting interfacial areas of contact). This section presents a detailed discussion of the background of this technique, its historical evolution, as well as the limitations of the present state of knowledge.

2.2.1 Background & Development of the DGD Technique

The DGD technique was originally introduced by Sriram and Mann [1977] for measuring the characteristics of gas-liquid dispersion. In the process of conducting a dynamic gas disengagement test, the feed gas, or gas plus liquid, which is continuously injected into the contactor, is shut off, and the dynamic response of overall gas holdup during the gas disengagement is recorded as a function of time. The resulting temporal variation in gas holdup can then be used for estimating BSDs by applying empirical models. The interfacial areas of contact are then computed from the BSDs.

In the work of Sriram and Mann [1977], the disengagement process was recorded by visually tracking the change of the dispersion level in the column, and the technique was applied at low gas velocities and low gas holdups ($\Phi_G < 5\ \%$). Several researchers subsequently further investigated the mechanisms of the dynamic gas disengagement process and proposed/used a bimodal distribution to describe the dispersion. During the initial section of the gas disengagement process, the rapidly-rising large bubbles are quickly disengaged, followed by the much slower small bubbles [Vermeer & Krishna,1981, Schumpe & Grund, 1986]. Schumpe & Grund also significantly improved the accuracy of this technique by taking into account the effect of the downward-moving liquid (needed to compensate for the volume of the disengaged gas) on the bubble rise velocities. Shortly thereafter, Patel et al. [1989] were able to significantly expand the capabilities of this technique by generalizing the gas disengagement equations so that they can be used to multimodal bubble size distribution. The next significant improvement in the DGD technique was introduced by Daly et al. [1992], who used pressure transducer signals instead of visualization to monitor changes in the gas dispersion level. This eliminated the need to use transparent columns and significantly enhanced the accuracy and reproducibility of the technique.

Recently, several investigators combined electrical resistance tomography (ERT) with the DGD technique to gain better insight into the local and global variation in gas holdups in order to accurately characterize the gas-liquid dispersion [Fransolet et al., 2005, Jin et al., 2007, Babaei et al., 2015, Hashemi et al., 2016, Khalili et al., 2017, Adetunji & Rawatlal, 2017, Adetunji & Rawatlal, 2018 & Kazemzadeh et al., 2018]. Besides, several investigators used computational fluid dynamics (CFD) to analyze the DGD and ERT data to characterize the gas-liquid dispersions encountered in bubble columns and its axial distribution along with the column height, as well as obtaining good estimates of the bubble coalescence and breakage rates throughout the column [Vadlakonda & Mangadoddy, 2017, Kazemzadeh et al., 2018, Adetunji & Rawatlal, 2018]. Table 2.1 summarizes the contributions of the various investigators to the DGD technique.

Table 2.1 Summary of the contributions of the various investigators to the DGD technique.

Investigators	**System investigated**	**No. of Bubble size classes**	**Bubble sizes measured**	**d_{32}**	**Max. Φ_G**
Sriram and Mann (1977)	Air-Liquid	N/A	N/A	N/A	4.88 %
Vermeer & Krishna (1981)	Nitrogen-Turpentine 5	2	N/A	N/A	45 %
Sasaki et al. (1986)	Argon-Aqu. SHS	Multi-class	0 – 2 mm	N/A	N/A
Schumpe & Grund (1986)	Air / Tap Water	2	N/A	N/A	27 %
Patel et al. (1989)	Air / Tap Water	2	FB: 1.0-1.4 mm CB: 18 – 160 mm	1.4 - 5.2 mm	19 %
Daly et al. (1992)	Nitrogen-Molten wax	5	N/A	0.4 - 2.2 mm	27 %
Luo et al. (1996)	Air, N_2 / Tapwater; Salt water; Dodecylbenzene; Aqu. Propanol	1 - 6	Air-tap water: 4.3 – 22.1 mm	Air-tap water: 4.7 – 7.8 mm Other systems: 1.2 – 6.5 mm	45 %
Hyndman et al. (1997)	Air-Water	2	N/A	N/A	22 %
Krishna et al. (1997)	Air / Paraffin Oil / Slurry	2	N/A	N/A	50 %
Mikkilineni et al. (1997)	Air-Water	1 & 2	N/A	N/A	N/A
Camarasa et al. (1999)	Air / Tap water & Aqu. alcohol solutions	4 - 5	N/A	N/A	25 %

Investigators	System investigated	No. of Bubble size classes	Bubble sizes measured	d_{32}	Max. Φ_G
Lee et al. (1999)	Air / Tap water / Alumina particles	2 / 4	Four classes in the range of 3- 20 mm	N/A	19 %
Urseanu (2000)	Air / Water; Tellus oil; Aqu. Ethanol	2	N/A	N/A	42 %
Krishna et al. (2001)	Air / Paraffin oil; Slurry; Tellus oil; Demin. Water / Slurry	2	FB: 1-4 mm, CB:15-50 mm	N/A	35 %
Jordan et al. (2003)	N_2; He / Aqu. Ethanol; 1-Butanol; Toluene; decalin & tap water	2	N/A	N/A	38 %
Lemoine et al. (2004)	Air; N_2 / Organic liquids and solutions	Multi-class	1 - 80 mm	1-3.5 mm	47 %
Fransolet et al. (2005)	Air / Tap water; Air / Aqu. Xanthan	2-3	N/A	N/A	14.5 %
Jin et al. (2007)	Air / Tap water	5	N/A	2.3-6.5mm	21 %
Behkish et al. (2007)	N_2, He / Isopar-M / Alumina powder	Multi-class	0.2 - 100 mm	0.96-11 mm	62 %
Yang et al. (2010)	Air / Distilled water & polymer solutions	2	N/A	N/A	22 %
Jin et al. (2013)	Air / Tap water	4	Four classes in the range of 9- 30 mm	11-16 mm	22 %
Xing et al. (2013)	Air / Deionized water; Air / Aqu. Glycerol	2	N/A	N/A	32 %
Li et al. (2013)	Air / Tapwater / Spherical glass powder	2	N/A	N/A	61 %

Investigators	System investigated	No. of Bubble size classes	Bubble sizes measured	d_{32}	Max. Φ_G
Lim et al. (2013)	Air / Water; Aqu. CM & Ethanol sol.	2	N/A	N/A	24 %
Jhawar et al. (2014)	Air / Tap water	2	N/A	N/A	28 %
Parmar & Majumder (2015)	Air; N_2; CO_2; / Aqu. Surfactant solutions	1	17 - 32 μm	N/A	N/A
Babaei et al. (2015)	Air / MLSS	2	N/A	8 - 28 mm	3.2 %
Guo et al. (2016)	Nitrogen / Deionized water; Ethanol; Aqu. Alcohol sol.	2	N/A	N/A	62 %
Hashemi et al. (2016)	Air / Aqu. Corn syrup	3-4	N/A	0.8 - 3.3 mm	4.4 %
Parisien et al. (2017)	N_2 / Tap water; N_2 / Aqu. Ethanol	1 or Multi-class	N_2 - Aqu. Ethanol: 160 - 560 μm	N/A	40 %
Vadlakonda & Mangadoddy (2017)	Air / Water	Multi-class	N/A	5.2 - 8.8 mm	N/A
Adetunji & Rawatlal (2017)	Air / Water	Multi-class	N/A	2.3 – 25 mm	3 %
Adetunji & Rawatlal (2018)	Air / Water	30	N/A	4.8 - 15.9mm	4.7 %
Basha & Morsi (2018)	Catalyzed Fisher Tropsh Conditions	Multi-class	One example 3.3 - 12 mm	Over the exp. range 0.15 – 7.5 mm	N/A
Kazemzadeh et al. (2018)	Air / Water	N/A	N/A	6.5 – 26 mm	0.16 %

Investigators	System investigated	No. of Bubble size classes	Bubble sizes measured	d_{32}	Max. Φ_G
Khalili et al. (2018)	Air / Aqu. Xanthan gum	3	N/A	1.6 - 3.1 mm	6 %
Tao et al. (2019)	Air / Water	2	N/A	N/A	59 %
Möller et al. (2019)	Air/Deionized water	2	N/A	N/A	27 %
Bae et al. (2021)	Air-Water, Air-Kerosene	N/A	N/A	N/A	25 %

2.2.2 Limits of the Present State of Knowledge

Although several investigators contributed towards improving the capabilities of the DGD technique, there are still some issues/limitations encountered when applying this technique to characterize the gas-liquid dispersions. For instance, as shown in Table 2.1, about half of the investigations listed used this technique only to determine bubble rise velocities and gas holdup structures without any attempt to estimate the corresponding bubble sizes. Besides, around two-thirds of the works divided the ensuing BSD into 2 to 3 classes (large & small bubbles or large, medium & small bubbles). Furthermore, most of the investigations in which bubble sizes were estimated focus on large bubbles (around 1-160 mm) that are typically generated using inefficient spargers in conjunction with uncontaminated systems [Besagni et al., 2018]. Very few investigations involved bubble sizes smaller than 1 mm [Behkish et al., 2007, Parmar & Majumder, 2015, Parisien et al., 2017, Adetunji & Rawatlal, 2018].

Although Patel et al. [1989] developed the generalized equations for predicting multi-class bubble sizes, it is also important to note that they did not succeed in describing the DGD process with multi-class sizes of bubbles. This can most probably be attributed to their use of a rapidly coalescent system (tap water). On the other hand, most of the investigations in which multi-class BSDs were reported were conducted using slowly-coalescent contaminated systems capable of maintaining broad BSD throughout a large part of the column.

Furthermore, it is only over the past five years that the reproducibility of the gas holdup results obtained from the DGD technique has been discussed. The reproducibility values for gas holdup measurements reported by Jhawar et al. [2014] and Parisien et al. [2017] were 5 % and 1 %, respectively. The reproducibility for ERT measurements reported by Hashemi et al. [2016] was 1 %, the measurement results used to calculate gas holdups.

From the aforementioned discussion, it becomes obvious that although the DGD technique has been used for several decades to characterize gas-liquid dispersions, further investigation is needed to facilitate its application to the measurement of fine bubbles encountered in flotation and other applications where the use of microbubbles can be beneficial (e.g., chemical /biochemical reactors, wastewater treatment). Furthermore, the reproducibility of this technique and its ability to estimate BSDs should be quantified in order to enhance confidence in its output.

This investigation aims to develop methodologies and algorithms that will allow the DGD technique to characterize the G/L dispersions encountered at different locations throughout pneumatically agitated columns under process intensified conditions where the bubble sizes are mainly under 3,500 μm. To facilitate the use of this technique, it is desirable that the data collection and analysis can be as automatized as possible, and the outputs can be further used to assess the sparger performance, a factor now receiving greater significance, particularly under the contaminated conditions typically encountered in industry. In order to have a better understanding of the limit of the present stage of knowledge, models and simplifying assumptions used for analyzing DGD data are summarized in Table 2.2. Since some investigators included in Table 2.1 did not report any information on these aspects, they are not included in Table 2.2.

The DGD technique generates information concerning the volume fraction of bubbles classified according to their slip velocity relative to the liquid phase. This, in turn, is used to generate the BSDs based on advanced knowledge of the forces acting on bubbles rising in stagnant liquids and how they are affected by the size/shape of bubbles and the extent of interfacial contamination. As shown in section 3, this task is not simple considering the present state of knowledge of the various factors affecting it. Fortunately, this is rapidly improving. For example, selecting the appropriate drag coefficient expression is a difficult task, even in the homogeneous flow.

Table 2.2 Summary of assumptions and factors considered by previous investigators in their DGD data analysis.

Investigators	**Account for the effect of downward U_L**	**Drag model for estimating d_B**		**Assumptions for disengagement of different bubble classes**		
		Model Used	**If the model is used, Cont. level**	**Independent**	**Const. "Slip" Velocity**	**Sequential**
Sriram and Mann (1977)	Not mentioned	No	-	Yes	-	-
Vermeer & Krishna (1981)	Not mentioned	No	-	-	-	Yes
Schumpe & Grund (1986)	Yes	No	-	-	Yes	-
Patel et al. (1989)	Yes	Peebles & Garber (1953); Clift et al. (1978); Abou-el-Hassan (1983)	Not specified	Yes	-	Yes
Daly et al. (1992)	Yes	Clift et al. (1978); Abou-el-Hassan (1983)	Not specified	Yes	-	-
Luo et al. (1996)	Yes	Fan & Tsuchiya (1990)	Not specified	Yes	-	-
Hyndman et al. (1997)	Yes	No	-	Yes	-	-
Krishna et al. (1997)	Not mentioned	No	-	Yes	-	-
Kumar et al. (1998)	Not mentioned	No	-	-	-	Yes

Investigators	Account for the effect of downward U_L	Drag model for estimating d_B		Assumptions for disengagement of different bubble classes		
		Model Used	If the model is used, Cont. level	Independent	Const. "Slip" Velocity	Sequential
Camarasa et al. (1999)	Not mentioned	No	-	Yes	-	-
Lee et al. (1999)	Yes	No	-	Yes	Yes	-
Urseanu (2000)	Yes	No	-	-	Yes	-
Krishna et al. (2001)	Yes	No	-	Yes	-	-
Jordan et al. (2003)	Yes	No	-	-	Yes	-
Lemoine et al. (2004)	No	No	-	Yes	-	-
Jin et al. (2007)	Not mentioned	Mendelson (1967); Motarjemi & Jameson (1978)	Not specified	Yes	-	-
Behkish et al. (2007)	Not mentioned	No	-	Yes	-	-
Yang et al. (2010)	Yes	No	-	Yes	-	-
Jin et al. (2013)	Not mentioned	Motarjemi & Jameson (1978)	Not specified	Yes	-	-
Li et al. (2013)	Yes	No	-	Not mentioned		

Investigators	Account for the effect of downward U_L	Drag model for estimating d_B		Assumptions for disengagement of different bubble classes		
		Model Used	If the model is used, Cont. level	Independent	Const. “Slip” Velocity	Sequential
Parmar & Majumder (2015)	Not mentioned	Stokes (1851)	Rigid sphere	Not mentioned		
Parisien et al. (2017)	Yes	Tomiyama et al. (1998)	Fully contaminated	Yes	-	-
Vadlakonda & Mangadoddy (2017)	Not mentioned	Mendelson (1967); Motarjemi & Jameson (1978)	Not specified	Not mentioned		
Adetunji & Rawatlal (2017)	Yes	No	-	Not mentioned		
Adetunji & Rawatlal (2018)	Yes	No	-	Yes	-	-
Kazemzadeh et al. (2018)	Not mentioned	Schiller & Naumann (1935)	Rigid sphere	Not mentioned		
Basha et al. (2018)	No	Fukuma et al. (1987)	Not specified	Yes	-	-

It is, therefore, interesting to note that, as shown in Table 2.2, only about one-third of the previous investigators used a drag coefficient model for predicting bubble sizes. Of these, only one-third did clearly specify the contamination level of the model used.

In addition to the inconsistency with respect to the use of appropriate drag models for single spheres, many investigators neglected to take into account the effect of adjacent spheres. This is a factor that may be of limited importance in the case of large bubbles but can be of great significance in the case of small contaminated bubbles where large gas holdups can be achieved even at relatively small superficial gas velocities (U_G). Only four investigators took that factor into consideration in their simple data analysis approach, namely: Patel et al. [1989], Luo et al. [1996], Urseanu [2000], and Parisien et al. [2017]. On the other hand, these factors were implicitly included by those who used CDF in their analysis, but inadequate attention was given to the selection and specification of complete and relevant models.

The actual DGD process is so complicated that it is difficult to analyze without simplifying assumptions. Some of the assumptions most commonly used by previous investigators are:

- The gas holdup corresponding to different size classes/fractions of bubbles are assumed to be axially uniformly distributed prior to the interruption of gas flow; the gas holdup structure at any cross-section is constant.
- No coalescence or breakup happens during the gas disengagement,
- The disengagement rate of each bubble size class is constant throughout the whole disengagement process. This corresponds to the assumption that all bubble classes disengage independently of any other bubble classes.

Although the first two assumptions have been adopted by most previous investigators, all experimental investigations and CFD simulations suggest that this is rarely the case since all gas-liquid dispersions are thermodynamically unstable and bubbles tend to break up and coalesce as they ascend through the column. Whereas bubble breakage rates are quite large in large-scale bubble columns operating at high U_G values, bubble breakage rates are expected to be minimal under the very small energy dissipation rates encountered during the disengagement period. Similarly, bubble coalescence rates are very high in slightly-contaminated systems (e.g., tapwater) operating at the relatively elevated energy dissipation rates encountered at high U_G values used in conventional bubble columns. The situation is significantly different in the case of microbubble-aerated columns operating at much lower superficial gas velocities and contaminated systems. Under such conditions, the hydrodynamic conditions are expected to be coalescence-dominated, with the coalescence rate being controlled by the nature and concentration of contaminants present in the system. This can significantly affect flow regime transitions and the gas holdup encountered in such columns [Idhbeaa et al., 2022, In Preparation]. However, a significant difference in the mixing patterns can exist between the sparger region and that prevalent throughout the rest of the column [Anastasiou et al., 2013; Mouza et al., 2018].

Furthermore, there is a disagreement on how the different bubble size classes disengage. Few investigators argued that during the gas disengagement period, the small bubbles could only disengage after the large bubbles are completely disengaged (usually referred to as sequential disengagement) [Vermeer & Krishna, 1981; Kumar et al., 1998]. However, the use of this assumption was found to underestimate the gas holdup of the small bubbles that get drawn into the wake of large bubbles and are disengaged together with large bubbles [Jordan et al., 2003].

The assumption that the disengagement rate of each bubble size class is constant throughout the disengagement period (i.e., all bubbles disengage independently) has been accepted by many investigators. However, Schumpe & Grund [1986] pointed out that the downward flow of liquid during the large bubble disengagement period will adversely affect the rise velocity of small bubbles, a factor which is neglected by assuming independent bubble “rise” velocity. They overcame this problem by assuming that the “slip” velocity of each bubble size class remains constant during the gas disengagement period. Although most investigators have accepted the effect of downward liquid velocity on bubble rise velocities, some investigators draw attention to the mechanism by which the presence of large bubbles could entrap smaller bubbles in their wake, thereby accelerating their rise velocity [Luo et al., 1996, Yang et al., 2010, Parisien et al., 2017]. As a result, they suggested that the aforementioned acceleration of the small bubble rise velocity could compensate for the lowering rise velocity of small bubbles due to the downward liquid velocity during the large bubble disengagement. Furthermore, the small bubble gas holdups predicted by these two assumptions (constant slip velocity and independent disengagement) were compared [Jordan et al., 2003]. The comparison was conducted at high-pressure operations in an N_2-Butanol system. They found that both assumptions yield quite similar holdups of small bubbles, especially when U_G < 50 mm/s. Although the deviation increased with increasing superficial gas velocity, the difference between the results was still low even at U_G = 200 mm/s (less than 6 %).

Although the output from the DGD test could be an empirical representation of BSD (typically represented by a set of average bubble diameters: d_{10}, d_{20}, d_{30}, d_{32}, d_{43}), there is a growing realization that the BSD generated by a wide range of G/L contactors follow well-established distributions such as the Log-Normal or the Rosin-Rammler distribution (often referred to as the Weibull distribution) [Adetunji & Rawatlal, 2017, Adetunji & Rawatlal, 2018, Basha et al., 2018]. This has the advantage of presenting the central tendency, the spread around the mean, as well as scoliosis at once using only two parameters.

The present stage of the DGD data analysis program will therefore characterize the BSD using these two distributions. This will be accomplished by conducting a preliminary assessment of how well these distributions fit the cumulative and distributive BSD using Excel sub-functions. Further quantification of the BSD fits, in terms of mean, variance, skewness, and goodness of fit, is recommended to be conducted using commercial software (e.g., OriginLab or SPC Excel) in future work.

The newly-developed DGD data collection/data analysis algorithm was tested using a tall large-diameter unit in order to ensure the relevance of the results obtained to industrial practice [Rollbusch et al., 2015]. Furthermore, there is a growing awareness of the critical role that spargers play in determining the G/L contacting characteristics in pneumatically-agitated columns, particularly in contaminated systems [Besagni & Inzoli, 2017]. The output from the DGD data analysis program can therefore be used to characterize a wide range of parameters that are critical to the development of a better understanding of the behaviour of gas/liquid contacting in industrially relevant systems and the development of more effective G/L contactors:

- **Local and average values in the contacting vessel:** gas holdups throughout the column, energy dissipation rates, estimated BSD and various average bubble sizes, maximum stable bubble size in different parts of the column, flow regime assessment parameters (drift flux and pressure fluctuations).
- **Sparger performance:** (e.g., BSD and various average bubble sizes generated by the sparger, location of the standing sonic wave, interfacial area of contact in the dispersion generated,
- **Bubble coalescence tendencies:** with some minor modification of the present setup, it becomes possible to assess the temporal and axial variation of the estimated BSD. These can then serve as an indicator of the coalescence tendencies of the system.

CHAPTER 3 EFFECT OF CONTAMINANTS ON THE SLIP VELOCITY OF SMALL BUBBLES

3.1 Introduction

Gas-Liquid interfaces play an important role in a wide range of industrial operations, as well as many natural systems with the environmentally critical gas exchange processes taking place between air and large bodies of water being but an example [Pereira et al., 2018]. However, virtually all naturally-occurring water bodies, as well as the process streams encountered in the chemical/biochemical/process industries, contain amphiphilic contaminants (such as alcohols, surfactants, organic acids, electrolytes, amines, glycols, proteins, phenols), the presence of which can significantly affect the hydrodynamic and mass transfer performance [Besagni & Inzoli 2017, Gemello et al., 2018; Rivas-Interián et al., 2018], even finely divided particulates can act in a similar manner [Binks, 2002]. The importance of taking this factor into account when considering inter-phase mass transfer can best be illustrated by the findings of the meticulous investigation conducted by McKenna & McGillis [2004], where they reported more than a 4-fold reduction in gas transfer velocity across flat interfaces in the presence of contaminants. They also found that both distilled and filtered deionized water can still contain significant levels of surface-active organics, whereas some commercially available spring waters, while not being surfactant-free, contain very low amounts of organics and can be significantly cleaner than laboratory distilled water.

Consequently, something as simple as quantifying the rise velocity of a single bubble in contaminated aqueous systems is complicated by the strong interaction between hydrodynamic and interfacial forces involved in such systems. This topic has been the subject of many investigations over the past several decades [Clift et al., 1978]; however, recent investigations enhanced our understanding of the factors affecting bubble rise velocity [Tomiyama et al., 1998; Yan et al. 2018] as well as those affecting the diffusion and adsorption of the contaminants at the gas/liquid interface of the rising bubble [Alves et al., 2005; Mehrabadi, 2009; Jarek et al., 2016; Tanaka et al., 2019].

As seen from Table 3.1, many models are commonly used to predict/correlate the drag coefficients on a single bubble rising in liquids of varying degrees of contamination (uncontaminated, partially-contaminated, contaminated systems, and rigid bodies). To facilitate understanding of the limits within which each equation can be used in the newly-developed DGD data analysis program, information pertaining to the systems investigated. In this way, the program user can select the drag model closest to the situation being investigated.

Table 3.1 Built-in expressions for the drag on single bubbles.

A. Correlations for rigid spheres

Investigators	**Equations/Correlations**	**Remarks**
Stokes (1851)	$C_D = \frac{4}{3}\frac{(\rho_L-\rho_G)}{\rho_L}\frac{gd_B}{{U_{TBSG}}^2}$; $U_{TBSG} = \frac{{d_B}^2 g(\rho_L-\rho_G)}{18\mu_L}$	Spherical particles, applicable for homogeneous flow
Schiller & Naumann (1935)	$C_D = \max\left\{\frac{24}{Re}(1+0.15Re^{0.687}), 0.44\right\}$	Spherical particles

B. Correlations for uncontaminated bubbles

Investigators	**Equations/Correlations**	**Remarks**
Hadamard–Rybczynski (1911)	$C_D = \frac{4}{3}\frac{(\rho_L-\rho_G)}{\rho_L}\frac{gd_B}{{U_{TBSG}}^2}$, $U_{TBSG} = \frac{{d_B}^2 g(\rho_L-\rho_G)}{12\mu_L}$.	Fully-mobile bubbles in uncontaminated systems
Jamialahmadi et al. (1994)	$C_D = \frac{4}{3}\frac{(\rho_L-\rho_G)}{\rho_L}\frac{gd_B}{{U_{TBSG}}^2}$, $U_{TBSG} = (\frac{2.14\sigma}{\rho_L d_B} + 0.505gd_B)^{0.5}$.	Distilled water
Tomiyama et al. (1998)	$C_D = max\left\{min\left[\frac{16}{Re}\left(1+0.15Re^{0.687}\right), \frac{48}{Re}\right], \frac{8}{3}\frac{Eo}{Eo+4}\right\}$	Water carefully distilled two or more times used.

Investigators	Equations/Correlations	Remarks
Baz-Rodriguez et al. (2012)	$U_{TBSG} = \frac{1}{\sqrt{\frac{1}{U_{TBSG1}{}^2}+\frac{1}{U_{TBSG2}{}^2}}}$, $U_{TBSG1} = U_{TBSG_{pot}}\left[1 + 0.73667\frac{(gd_B)^{1/2}}{U_{TBSG_{pot}}}\right]^{1/2}$, $U_{TBSG_{pot}} = \frac{1}{36}\frac{(\rho_L-\rho_G)gd_B{}^2}{\mu_L}$, $U_{TBSG2} = (\frac{3\sigma}{\rho_L d_B} + \frac{(\rho_L-\rho_G)gd_B}{2\rho_L})^{1/2}$.	For uncontaminated systems. Applicable for a wide range of bubble equivalent diameters following the combination of viscous effect and surface tension effect.

C. Correlations for contaminated bubbles

Investigators	Equations/Correlations	Remarks
Ishii & Zuber (1979)	$C_D = max\left\{\frac{24}{Re}(1 + 0.15Re^{0.687}), min\left[\frac{2}{3}Eo^{0.5}, \frac{8}{3}\right]\right\}$	0.1 wt % of Aqu. SDS and Na_2SO_4, 0.001 wt % of Aqu. Isoamyl alcohol, isobutanol.
Karamanev et al. (1996)	$C_D = max\left\{\frac{24}{Re}(1 + 0.173Re^{0.657}) + \frac{0.413}{1+16300Re^{-1.09}}, 0.95\right\}$	Fully-contaminated Newtonian liquids
Tomiyama et al. (1998)	$C_D=max\left\{min\left[\frac{24}{Re}(1+0.15Re^{0.687}), \frac{72}{Re}\right], \frac{8}{3}\frac{Eo}{Eo+4}\right\}$	Partially contaminated (Water with a purity level varying between double distilled and tap water)
Tomiyama et al. (1998)	$C_D = max\left\{\frac{24}{Re}(1 + 0.15Re^{0.687}), \frac{8}{3}\frac{Eo}{Eo+4}\right\}$	Fully contaminated (Tap water and other fully contaminated. systems)

Investigators	Equations/Correlations	Remarks
Nguyen et al. (1998)	$C_D = \frac{4}{3}\frac{(\rho_L-\rho_G)}{\rho_L}\frac{g d_B}{{U_{TBSG}}^2}$, $U_{TBSG} = \frac{{d_B}^2 g(\rho_L-\rho_G)}{18\mu_L} \cdot \left(1 + \frac{\frac{Ar}{96}}{(1+0.079Ar^{0.749})^{0.755}}\right)^{-1}$. $Ar = \frac{{d_B}^3 {\rho_L}^2 g}{{\mu_L}^2}$,	Water with frothers, applicable for Re < 130
Ng et al. (1999)	$C_D = \frac{4}{3}\frac{(\rho_L-\rho_G)}{\rho_L}\frac{g d_B}{{U_{TBSG}}^2}$, $U_{TBSG} = \frac{{d_B}^2 g(\rho_L-\rho_G)}{18\mu_L}\left(\frac{7}{6}Re^{0.15} + 0.02Re\right)^{-1}$.	Contaminated bubbles. Used for calculating the mass of bitumen contained in the bitumen-air aggregates

The advanced DGD program developed in this investigation is designed to allow the users to choose any of the above-listed models based on their needs. However, attention is focused on small bubbles (50-3,500 μm) because of:

- Their relevance to the approach commonly used for intensifying gas/liquid mass transfer where large interfacial areas of contact are generated by the formation of fine and ultrafine bubbles [Bando et al., 2008; Terasaka, 2011; Baz-Rodrigues et al., 2012; Azizi and Al Taweel, 2015; Jang et al., 2018; Yasin et al., 2018]. That bubble size range is also of particular interest to flotation operations, where it is well known that the recovery and selectivity of fine particulates are enhanced by using fine bubbles [Rulyov et al., 2017].
- The uncertainties/difficulties associated with using the concepts developed in this investigation in conjunction with bubbles larger than the aforementioned size limits.

3.2 Effect of Contamination on the Rise Velocity of Single Small Bubbles

The rise velocity of bubbles is known to be slowed down in the presence of contaminants, with the impact being strongly affected by the nature and concentration of the contaminant. This is generally attributed to the accumulation of contaminant entities at the bubble’s gas/liquid interface and their tendency to interfere with the Hadamard-Rybczynski internal circulation within the bubble. For contaminated bubbles, the uneven distribution of the contaminants is driven by the surface advection generated by the liquid flow in the regions adjacent to the bubble. This results in the contaminants tending to concentrate in the tail-end stagnation point and the formation of tangential stress (commonly referred to as the Marangoni stress). These tend to counteract the flow-induced shear stress resulting in increasing the drag coefficient value. The formation of a dynamic adsorption layer of contaminants around the bubbles and the development of the forces acting on a contaminated Taylor bubble were numerically simulated by [Hayashi & Tomiyama, 2012]. They found the interfacial distribution of contaminants to be strongly dependant on contaminant properties and the Hatta number where the latter is the ratio of the rate at which the contaminants are being supplied to the interface by diffusion/adsorption, relative to that at which they are removed by advection. Similar conclusions were reported by Ramírez-Muñoz et al. [2012], who numerically determined the impact of contamination on the Reynolds number values under which a recirculating zone is formed behind a spherical bubble.

It is, however, important to realize that the time scales involved in the aforementioned processes are very small relative to the rise velocities of bubbles. Thus, for example, the dynamic surface tension measurements conducted using the maximum bubble pressure technique indicate that the process of contaminant diffusion/adsorption from the bulk of the liquid onto the gas/liquid interface is virtually completed within 1 second for a wide range of contaminated systems in spite of the very large surface expansion rates encountered in this technique [Djuve et al., 2001]. Similar time scales were reported while investigating the temporal variation in bubble velocity and shape [Krzan and Malysa, 2012; Zawala et al., 2015]. The much longer times needed to achieve equilibrium rise velocities observed by Alves et al. [2005] and Mehrabadi [2009] could have been caused by large bubble acceleration times or the presence of slowly-adsorbent contaminants.

Because of the formation of a dynamic adsorption layer on bubbles rising in contaminated liquids, the experimentally observed terminal bubble rise velocities were found to be strongly dependent on the purity of the liquid used, particularly for the small spherical/ellipsoidal bubbles encountered in the range of interest of this investigation (d_B < 3,500 μm). For example, whereas bubble slip velocities in excess of 360 mm/s were reported for bubbles rising in ultra-clean water [Duineveld, 1995; Sanada et al., 2008], it is reduced to half that value in the case of tap water. This significant change in the terminal rise velocity is usually attributed to the adsorption of contaminants at the gas/liquid interface the presence of which results in partial or complete immobilization of the interface [Clift et al., 1978, Kugou et al., 2003; Alves et al., 2005; Mehrabadi, 2009; Haapala, 2010]. The presence of these contaminants not only results in reducing the rise velocity of bubbles but can also significantly retard bubble coalescence and interphase mass transfer, with up to a 7-fold reduction in the value of the liquid side mass transfer coefficient being reported in the case of 1 mm bubbles [Vasconscelos et al., 2002; Deng et al., 2011; Aoki et al., 2015; Tanaka et al. 2019]. However, the impact of interfacial contamination is most pronounced in the case of bubble-coalescence time, where up to three orders of magnitude changes were observed in the presence of contaminants [Liu et al., 2019].

3.3 Accuracy of Bubble Rise Velocity Prediction: Comparison with Experimental Results

The topic of bubble rise velocity and how it is affected by the size of bubbles and the presence of contaminants that immobilize the interface is a topic of great significance in the chemical and biochemical process industry, mineral processing, wastewater remediation and is a necessary tool in order to understand the factors affecting interphase mass transfer in natural systems where bubbles are encountered. It has therefore received much attention many decades ago, with the work presented by Clift et al. [1978] being the primary source of information. However, as mentioned in section 3.2, recent advances in measurement technology and data analysis provided a large database of new experimental results that were obtained under well-controlled hydrodynamic and interfacial conditions that provided additional insight into the detailed motion of bubbles as they rise in stagnant liquids (including the periodic changes in shape factors, wobbling, zig-zag). Several new models and correlations were also proposed to predict the rise velocity of bubbles and how it is affected by the various degrees of contamination. In this investigation, attention is focused on fine and ultrafine bubbles, as they represent one of the most promising avenues for intensifying multiphase operations.

It was, therefore, necessary to conduct a comparative evaluation of all the pertinent correlations using the more accurate recent data. Attention was focused on the range of bubble sizes under mainly two contamination levels:

- Very small bubbles (0 - 140 μm) moving under different degrees of contamination
- Fully-contaminated bubbles (0 - 3,500 μm)
- Un-contaminated bubbles (0 - 3,500 μm)

Results obtained at different degrees of contamination were not included to avoid further confusing the issue. The data used for that purpose, and the conditions under which they were obtained, are given in Table 3.2.

Table 3.2 Summary of experimentally measured terminal velocities of single bubbles with known bubble sizes from previous investigations.

A. Uncontaminated systems

Investigators	**Investigated Range of d_B**	**Remarks**
Okazaki (1964)	320 - 1,820 μm	Distilled water
Duineveld (1995)	670 - 1,950 μm	Clean water
Kelsall et al. (1996)	30 - 110 μm	Aqu. $NaClO_4$ Sol. became surfactant-free only after 3 h purging
Leifer et al. (2000)	670 - 2,580 μm	Ultrapure water
Tomiyama et al. (2002)	600 - 700 μm	Distilled water
Wu & Gharib (2002)	1,060 - 2,100 μm	Clean water

Investigators	Investigated Range of d_B	Remarks
Alves et al. (2005)	1,120 - 3,540 µm	Distilled & Millipore water
Takahashi (2005)	12 - 51 µm	Distilled water
Parkinson et al. (2008)	18 - 115 µm	Ultra-clean water
Sanada et al. (2008)	400 - 1,750 µm	Super-purified water
Krzan & Malysa (2012)	1,480 µm	Distilled water
Tan et al. (2013)	1,450 µm	Water
Yan et al. (2017)	1,850 - 3,200 µm	Deionized water
Ziegenhein and Lucas (2017)	2,130 - 3,570 µm	Purified water
Nüllig & Peters (2018)	1,280 - 1,700 µm	Distilled water (fast bubbles without accumulation of impurities in the water)
Tanaka et al. (2019)	12 - 96 µm	Ultrapure Water

B. Contaminated systems

Investigators	Investigated Range of d_B	Remarks
Okazaki (1964)	730 – 2,630 µm	0.00288 wt.% & 0.0288 wt.% of aqu. SDS Sol.
Kelsall et al. (1996)	30 - 260 µm	0.0012 wt.% of Aqu. $NaClO_4$ Sol.
Kugou et al. (2003)	2,200 - 5,400 µm	3.29 % Salinity of Seawater, 3.41 % Salinity of Artificial Seawater
Okawa et al. (2003)	670 – 3,440 µm	An open vessel filled with distilled water (water may get contaminated with changes of time)
Alves et al. (2005)	500 µm - 2,650 µm	Water got progressively contaminated with time
Henry et al. (2008)	40 µm - 90 µm	1.105 wt.% of aqu. $HClO_4$, 2.816 wt.% of Aqu. $NaClO_4$ solutions
Mehrabadi (2009)	1,450 & 1,850 µm	0.025 wt.% & 0.027 wt.% of Aqu.1-Pentanol solutions
Haapala et al. (2010)	100 - 650 µm	0.0926 wt.% of Aqu. Butanol
Krzan & Malysa (2012)	1,480 µm	0.144 wt.% of Aqu. SDS Sol.
Tan et al. (2013)	1,450 µm	0.004 wt.% of Aqu. 1-Hexanol Sol.

Investigators	Investigated Range of d_B	Remarks
Nüllig & Peters (2018)	560 - 2,005 μm	Distilled water. Bubbles were slowed down due to the accumulation of impurities

Figure 3.1 mainly focuses on the comparison for bubble sizes less than 140 μm. As can be seen from Figure 3.1, the rise velocities of microbubble followed the predictions of the Hadamard-Rybczynski model for fully mobile interfaces only for those investigations in which extra care was exercised to ensure that the interfaces were not contaminated [Kelsall et al., 1996; Parkinson et al., 2008]. Surprisingly, the data obtained by Henry et al. [2008] for microbubbles immersed in aqueous solutions of $HClO_4$ and $NaClO_4$ behaved as fully mobile interfaces in spite of the electrolyte's ability to change the bubble coalescence behaviour from coalescent to virtually non-coalescent over the same concentration ranges. In a fashion similar to Kelsall et al. [1996], this behaviour was attributed to the use of prolonged sparging with clean N_2 gas whereby the bubbles collect the surface-active contaminant and deposit it on the glass above the liquid interface (which becomes noticeably hydrophobic as evidenced by dewetting of the aqueous solution).

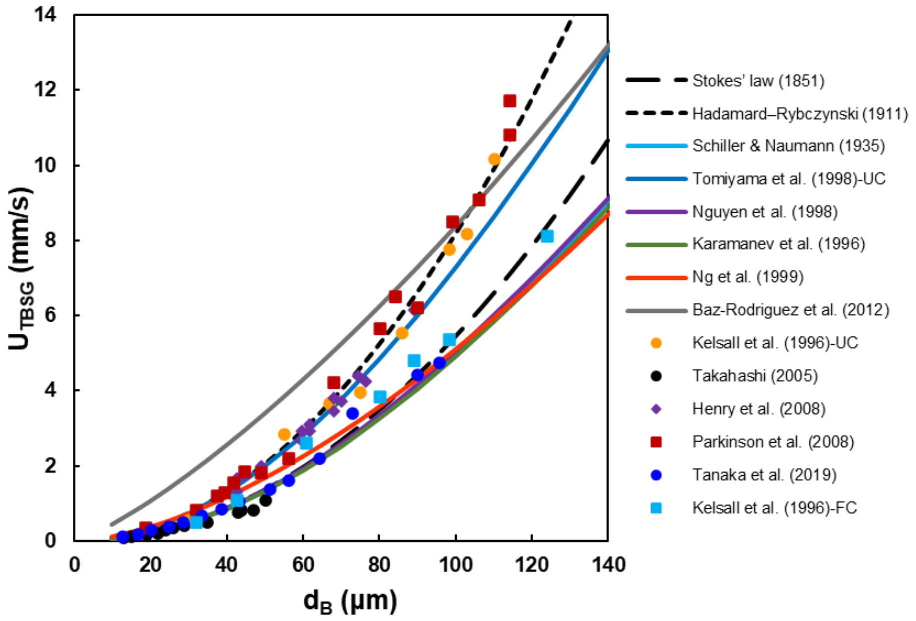

Figure 3.1 Comparison of drag models with experimental results for bubble sizes below 140 μm (for both contaminated and uncontaminated bubbles)

On the other hand, the rise velocities obtained by Takahashi [2005] for microbubbles rising in distilled water were lower than those predicted by Stokes law, presumably because they did not take extra precautions to strip the trace contaminants from the water. Similar trends were reported by the other two authors where the terminal bubble rise velocity of fully-contaminated microbubbles closely matches the Stokes law predictions [Kelsall et al. 1996, Tanaka et al., 2019].

Although it is well known that the use of very fine microbubbles (< 100 μm) results in significant improvement in mass transfer [Bando et al., 2008; Terasaka, 2011; Yao et al., 2016], the energy needed to generate such bubbles may be quite high. Many investigators, therefore, focused on the use of somewhat larger bubbles ($100 < d_B < 3{,}500$ μm) that are significantly smaller than those encountered under conventional operation even in the presence of strong coalescence-retarding systems [Besagni et al., 2017a, Besagni and Inzoli, 2017b]. Consequently, the effect of contamination on the bubble rise velocity is presented in Figures 3.2 and 3.3.

As seen in Figure 3.2, which represents a compilation of data selected from different publications, almost all the recent experimental results were obtained under carefully controlled conditions to ensure non-contamination of the system closely followed a singular trend until a bubble size of 1,300 μm. However, the experimental results diverge for bubbles larger than 1,300 μm in a fashion that clearly distinguishes between those who realized the difficulties associated with the generation and maintenance of uncontaminated systems and took extra care to achieve this and those who underestimated the effort needed.

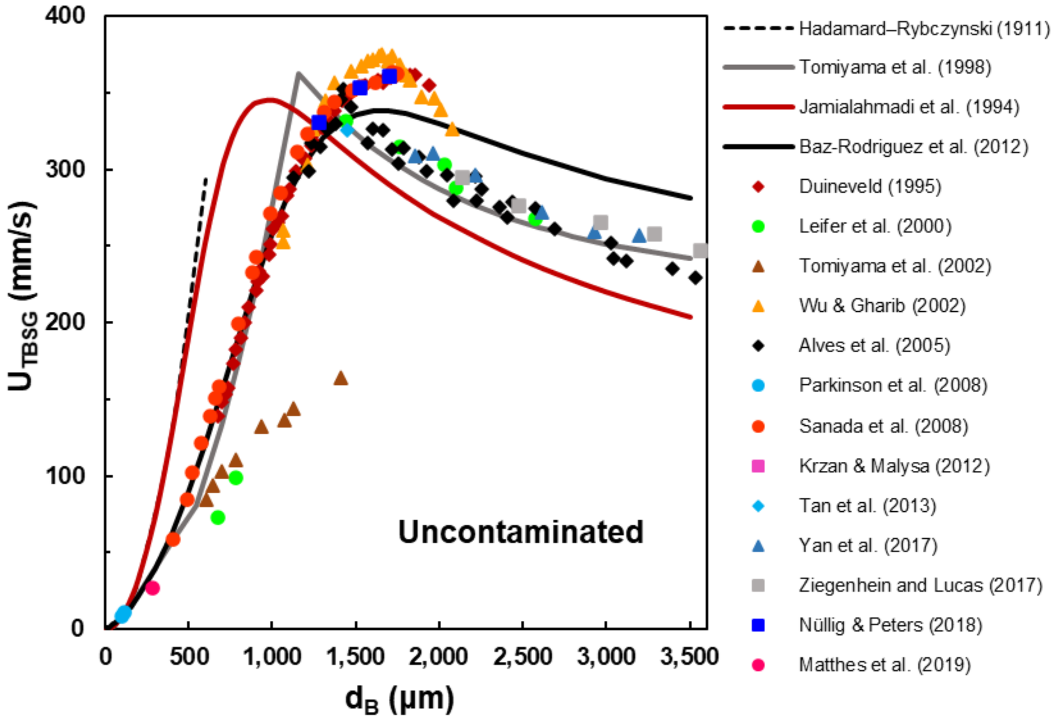

Figure 3.2 Comparison of drag models with experimental results obtained from uncontaminated systems for bubble sizes up to 3,500 µm.

In Figure 3.3, the plenty of experimental results reported by various investigations obtained under contaminated systems was compared to the drag models. As seen from Figure 3.3, almost all the drag models followed the same trend up to $d_B \approx$ 1,200 µm. Also, the experimental results fit quite well to the drag models up to this bubble size. An exception was found for Stokes' law, which is only available for Re < 1. After this bubble size, the drag model proposed by Karamanev et al. [1996] started deviating from other models. For 1,200 µm < d_B < 2,500 µm, the experimental results obtained from various investigations were found to cover the difference between the two groups of models. This can be attributed to different contamination levels under which these results were generated. For large bubble sizes (> 2,500 µm), very few experimental results were reported, which results in more uncertainties in this range.

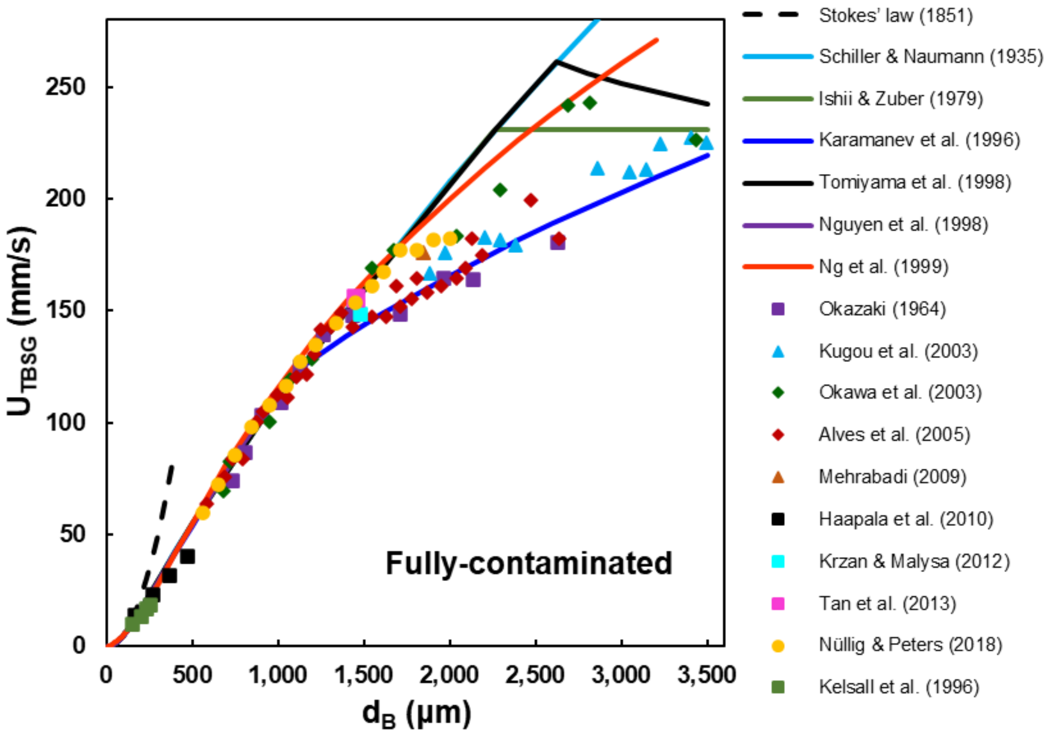

Figure 3.3 Comparison of drag models with experimental results obtained from contaminated systems for bubble sizes up to 3,500 μm.

3.4 Limits of the Drag Models for Estimating Bubble Sizes

In the DGD technique used in this investigation, bubble sizes are estimated using the experimentally determined terminal rise velocities of bubble classes. This process is the inverse of the commonly used process where the bubble size is known, and its rise velocity needs to be predicted. With this process, some models show a limit on estimating bubble sizes. For instance, as seen in Figure 3.4, a widely known drag model developed by Tomiyama et al. [1998] is used. A maximum U_{TBSG} is found, above which multiple bubble sizes can depict the same terminal velocity. By applying this maximum velocity, the limit of Tomiyama's uncontaminated model to estimate bubble sizes is up to about 920 μm in pure water at atmospheric conditions. Its fully-contaminated model can estimate bubble sizes up to about 2,250 μm with a surface tension of 72.8 mN/m in water at atmospheric conditions. The maximum velocity for estimating bubble sizes varies with both the model used and the system properties (e.g., liquid density, liquid viscosity, gas density, and surface tension). Therefore, the DGD data analysis program developed in this investigation has a built-in subroutine capable of identifying such limits for different models at various conditions and ensures that they are not exceeded if the user selects models that are not appropriate for the experimental results obtained. However, the values listed in Table 3.3 can act as a rough guide for the range of applicability of several commonly used models when dealing with contaminated aqueous media.

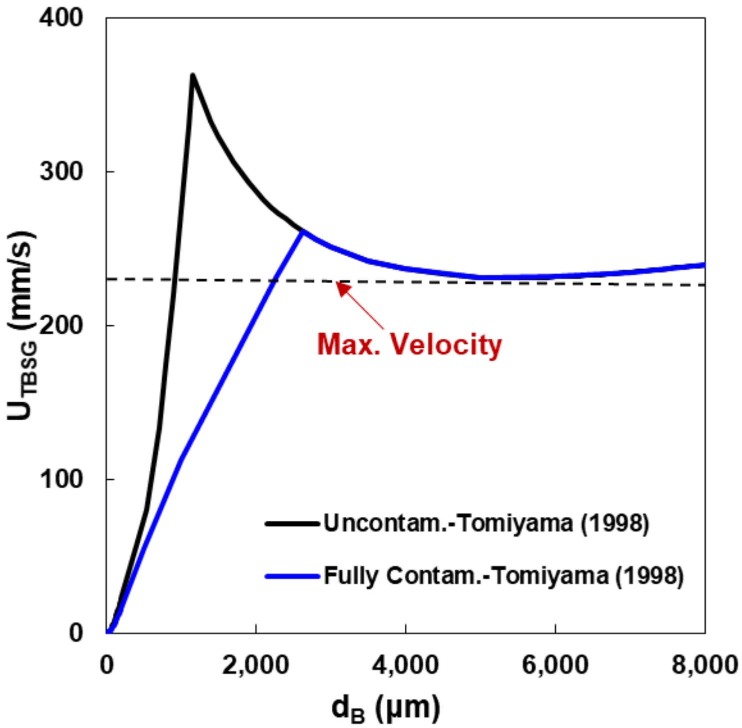

Figure 3.4 Effect of drag model on the limits imposed for its use in the DGD technique.

Table 3.3 The applicable range for the models used in contaminated systems with d_B < 3,500 μm.

Model proposed by	Approximately velocity limit
Schiller & Naumann (1935)	No limit
Ishii & Zuber (1979)	230 mm/s
Karamanev et al. (1996)	No limit
Tomiyama et al. (1998)	240 mm/s
Nguyen et al. (1998)	120 mm/s

3.5 Effect of Adjacent Bubbles on the Drag Force Acting on Single Bubbles

It is well known that the rise velocity of individual bubbles is strongly influenced by the presence of adjacent bubbles as well as by the flow regime through which they rise. The total shear rate experienced by a bubble can, therefore, be assumed to include liquid-, bubble-, and swarm-induced shears [Aliseda & Lasheras, 2011; Buffo et al., 2016; Loisy & Naso, 2017]. This approach results in the drag coefficient acting on a bubble rising in a swarm being expressed by the following general expression that accounts for these factors [Behzadi et al., 2004; Simonnet et al., 2008; Buffo et al., 2016]

$$\mathrm{C_D} = \mathrm{C_{D0}} * \int (\Phi_G) * \int (Turb.) \tag{3.1}$$

where

C_D is the drag coefficient associated with a bubble rising in a G/L dispersion,

$\int(\Phi_G)$ is a factor accounting for the effect of adjacent bubbles, and

$\int(Turb.)$ is a factor accounting for the impact of micro-scale turbulence in the bubble's vicinity.

The latter term can play a very significant role in retarding the slip velocities of bubbles/drops and particles and is usually taken into account by using an effective viscosity of the media, a parameter that takes into account the turbulence characteristics using the κ–ε turbulence model [Brucatto et al., 1989, Scargiali et al., 2007]. In the case of conventional pneumatically-agitated columns, one encounters significant energy dissipation rates in the liquid phase, particularly when the column is operated at elevated gas velocities [Besagni & Inzoli, 2017]. On the other hand, the results obtained in this investigation [Idhbeaa et al., 2022, In Preparation] suggest that the average energy dissipation rates encountered throughout the whole column is relatively low at the superficial gas velocities used in the present investigation (0.5 mm/s to 50 mm/s), and most of the experimental runs were observed to occur within the homogeneous flow regime (both true-homogeneous and pseudo-homogeneous). This conclusion is supported by the recent findings recently reported by Buffo et al. [2016], suggest that whereas the effect of turbulence on the bubble terminal rise velocity needs to be taken into consideration in the case of stirred-tank reactors (where large energy dissipation rates are induced by the externally driven mechanisms), it may not be necessary in the case of conventional bubble columns where energy dissipation rates are internally generated, relatively low, and where the crowding effect plays a more important role in reducing the effective terminal velocity. Finally, the DGD investigation is only concerned with small bubbles rising into still water where turbulence is virtually non-existent. It is, therefore, rather safe to assume that the impact of the turbulence factor on bubble drags does not play a significant role in analyzing DGD results and can be neglected in our analysis.

On the other hand, it is well known that the rise velocity of individual bubbles is strongly influenced by the presence of adjacent bubbles, with the effect being strongly a function of the gas holdup, bubble size distribution, and the rheological properties of the liquid. Since all the systems discussed in the present investigation are relatively low viscosity Newtonian liquids, attention in the following section will focus on how bubble crowding can reduce the rise velocity of bubbles. This is very often referred to as the effective drag coefficient of bubble swarms, C_{DSW}.

The drag coefficient of bubble swarms is significantly different from that of single bubbles due to the complex interactions taking place between the bubbles as well as the interactions between the bubbles and the liquid (turbulence modulation). The latter includes both the reduction of turbulence intensity at higher frequencies and the intensification of turbulence intensity at lower frequencies [Al Taweel and Landau, 1977]. This area of research is presently receiving much attention because of its relevance to the accurate simulation of multiphase systems [Simonnet et al., 2007, Roghair et al., 2011; Lane et al., 2016; Yang et al., 2018], and the state of knowledge in this field is rapidly changing. However, no general agreement on the most suitable models to be used under different hydrodynamic conditions has yet evolved, particularly in the case of small contaminated bubbles.

As can be seen from Figure 3.5, the presence of adjacent bubbles usually results in decreasing the rise velocity of small bubbles as they start moving closer to each other [Rusche and Issa, 2000; Zenit et al., 2001; Behzadi et al., 2004, Acuña & Finch, 2010, Buffo et al., 2016]. On the other hand, the average rise velocity of small bubbles can be enhanced as a result of:

- The tendency of the small bubbles to get entrapped in the wake of adjacent rapidly-rising larger bubbles, as shown in Figure 3.5 [Krishna et al., 1999; Vassallo and Kumar, 1999; Acuña and Finch, 2010; Yan et al., 2018].
- The tendency of the small bubbles to move together in the form of multi-bubble clusters, the rise velocity of which is larger than that of single bubbles [Takagi & Matsumoto, 2011; Roghair et al., 2013; Chen et al., 2015; Passos et al., 2015; Kong et al., 2019].

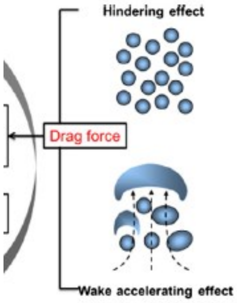

Figure 3.5 Effect of adjacent bubbles on the drag force acting of a single bubble (from Yang et al., 2018)

Consequently, the program for analyzing the DGD results was designed in a fashion to allow the user to select amongst a wide range of presently available models, and newly-developed ones can be easily incorporated.

As stated above, the average rise velocity of bubble swarms can be affected by either the hindering effect of small bubbles moving close to each other or by the wake-accelerating effect of large bubbles. Most of the earlier models focused on the interaction between small bubbles and closely followed the pioneering work of Richardson and Zaki [1954], who established the dependence of the relative velocity of solid particles in batch fluidization and sedimentation experiments. They expressed the effect of dispersed phase holdup on the relative velocity between the phases by,

$$\mathrm{U}_{SBSW} = \mathrm{U}_{TBSG} * (1 - \Phi_G)^n \tag{3.2}$$

where,

n is often referred to as "the Richardson and Zaki exponent" and is a function of the particle Reynolds number, and

U_{TBSG} is the terminal rise velocity of an isolated bubble in a quiescent liquid

Several investigators dealt with that topic using the average, or global, gas holdup value for bubbles rising in the homogeneous flow regime:

- Griffith and Wallis (1961) $\mathrm{U}_{SBSW} = \mathrm{U}_{TBSG} * (1 - \Phi_{Gglob})$ (3.3)
- Bridge et al. (1964) $\mathrm{U}_{SBSW} = \mathrm{U}_{TBSG} * (1 - \Phi_{Gglob})^{1.39}$ (3.4)
- Marrucci (1965) $\mathrm{U}_{SBSW} = \mathrm{U}_{TBSG} * (1 - \Phi_{Gglob})/(1 - \Phi_{Gglob})^{5/3}$ (3.5)

Lockett and Kirkpatrick [1975] suggested a modification to the Richardson and Zaki correlation that takes the bubble deformation into consideration. For a swarm of bubbles with $d_B = 5$ mm, and $\Phi_G < 66\%$, they obtained,

$$\mathrm{U}_{SBSW} = \mathrm{U}_{TBSG} * (1 - \Phi_{Gglob})^{1.39} * (1 + 2.55\Phi_{Gglob}) \tag{3.6}$$

Ishii and Zuber [1979] studied the drag force for a wide range of dispersed phase fractions and Reynolds number and proposed several correlations based on an extensive experimental database. Their correlations are still based on the global void fraction and are applicable to both the homogeneous and heterogeneous flow conditions (Stokes, viscous, distorted particle, and churn turbulent flow regimes). However, the critical gas holdup value for the flow regime transition must be specified to allow for the transition from one expression to the other.

Several recent investigations implemented the correlation accounting for adjacent bubbles in a CFD code and tested with experimental results under air-water and various contaminated systems [Behzadi et al., 2004; Roghair et al., 2011; Buffo et al., 2016]. The model proposed by Behzadi et al. [2004] was implemented in a CFD code and tested for bubbly flow through a sudden pipe expansion:

$$\mathrm{U}_{SBSW} = \mathrm{U}_{TBSG} * (e^{3.64\Phi_G} + {\Phi_G}^{0.864})^{-(1/2)} \tag{3.7}$$

Roghair et al. [2011] proposed a simple correlation for a mono-disperse swarm, and it is valid for 1 < Eo < 5 and Φ_G < 50%,

$$\mathrm{U}_{SBSW} = \mathrm{U}_{TBSG} * (1 + \left(\frac{18}{Eo}\right)\Phi_G)^{-(1/2)} \tag{3.8}$$

In the work of Buffo et al. [2016], an empirical drag model accounting for the effect of bubble crowding and micro-scale turbulence in the bubbly flow regime ($\Phi_G \leq$ 10%) was proposed,

$$\mathrm{U}_{SBSW} = \mathrm{U}_{TBSG} * (1 - \Phi_G)^{1.3/2} \tag{3.9}$$

This model was validated by comparing the experimental results obtained in bubble columns and stirred tanks with a broad range of operating conditions.

The problem with all the preceding correlations is that the crowding effect should be based on the local void fraction rather than on the global one since inter-bubble interaction is governed by local conditions. The global gas holdup could, however, be used to predict the crowding effect under conditions where the local and global gas holdups are close, and the bubbles are uniformly distributed over the column volume. For example, Garnier et al. [2002] measured the relative velocity in a highly controlled system where the bubble size is uniform and without variations in local void fraction. For d_B < 5.5 mm and Φ_{GLoc} < 0.35, they found the following correlation,

$$\mathrm{U}_{SBSW} = \mathrm{U}_{TBSG} * (1 - \Phi_{GLoc}{}^{1/3}) \tag{3.10}$$

The suitability of this correlation was confirmed by Guet et al. [2004] using another experimental system where d_B < 6 mm and Φ_{GLoc} < 0.20.

In the work of Simonnet et al. [2007], the local void fraction was used to account for the crowding effect. They concluded two behaviours for the variation of the bubble relative velocity with the local void fraction from their experimental results:

- For small bubbles ($d_B \leq 7$ mm), the bubble relative velocity decreases up to high void fractions (Φ_{GLoc} < 30 %),
- For large bubbles (d_B > 7 mm), the bubble relative velocity decreases up to about Φ_{GLoc} = 15 %,and increases beyond.

The latter behaviour can most probably be attributed to the onset of instability of flow regime at Φ_{GLoc} = 15 %. Moreover, they found that adding butanol to demineralized water could contribute to reducing the bubble size, and the bubble relative velocity kept increasing up to Φ_{GLoc} = 35 %. In this investigation, our focus is for d_B < 3.5 mm in contaminated systems, and the homogeneous flow regime was observed in most of the runs. It is, therefore, not necessary to consider the instability effect considered in Simonnet's model. A second-order polynomial fit to Simonnet's model (based on Φ_{GLoc} < 15 %) was thus built into the program to represent the conditions where the impact of flow instabilities on bubble drags can be neglected. A graphical representation of the aforementioned models is presented in Figure 3.6.

Table 3.4 summarizes these models and the range of conditions for which they have been tested/verified.

Table 3.4 Built-in expressions for the drag on bubble swarms.

Investigators	Drag coefficient correction equation	Remarks
Richardson & Zaki (1954)	$\frac{C_{DSW}}{C_D} = [(1-\Phi_G)^{\mathrm{m}-1}]^{-2}$	Not available
Griffith & Wallis (1961)	$\frac{C_{DSW}}{C_D} = (1-\Phi_G)^{-2}$	Air-Water (hot and cold)
Bridge et al. (1964)	$\frac{C_{DSW}}{C_D} = [(1-\Phi_G)^{1.39}]^{-2}$	$\Phi_G \leq 45$ %; Air and various contaminated aqueous systems
Marrucci (1965)	$\frac{C_{DSW}}{C_D} = [(1-\Phi_G)^2/(1-{\Phi_G}^{5/3})]^{-2}$	Correlation proposed based on a spherical cellular model (1 << Re < 300)
Lockett & Kirkpatrick (1975)	$\frac{C_{DSW}}{C_D} = \left[(1-\Phi_G)^{1.39}(1+2.55{\Phi_G}^3)\right]^{-2}$	$\Phi_G \leq 66$ %; $d_B = 5$ mm; Air bubbles rising in tapwater & distilled water.
Garnier et al. (2002)	$\frac{C_{DSW}}{C_D} = \left[1-{\Phi_G}^{1/3}\right]^{-2}$	$\Phi_G \leq 43$ %; $d_B = 3.3 - 4.5$ mm; Validate in air-demineralized water.
Behzadi et al. (2004)	$\frac{C_{DSW}}{C_D} = (e^{3.64\Phi_G} + {\Phi_G}^{0.864})$	Implemented in a CFD code and tested for bubbly flow through a sudden pipe expansion (air-water).
Simonnet et al. (2007)	$\frac{C_{DSW}}{C_D} = [(1-\Phi_G)^m + \left(4.8\frac{\Phi_G}{(1-\Phi_G)}\right)^m]^{-2/m}$	$\Phi_G \leq 30$ %; m =25 $d_B = 5 - 10$ mm; air- demineralized water, air-Aqu. butonal.

Investigators	Drag coefficient correction equation	Remarks
Roghair et al. (2011)	$\frac{C_{DSW}}{C_D} = 1 + (\frac{18}{Eo})\Phi_G$	$\Phi_G \leq 50$ %;d_B = 3 - 6 mm; 1 < Eo < 5; Implemented in a CFD code using air-water, and more viscous liquids
Buffo et al. (2016)	$\frac{C_{DSW}}{C_D} = (1 - \Phi_G)^{-1.3}$	Applicable for $\Phi_G \leq 10$ % Implemented in a CFD code and tested in stirred tanks and bubble columns under air-water and air-Aqu. NaCl systems.

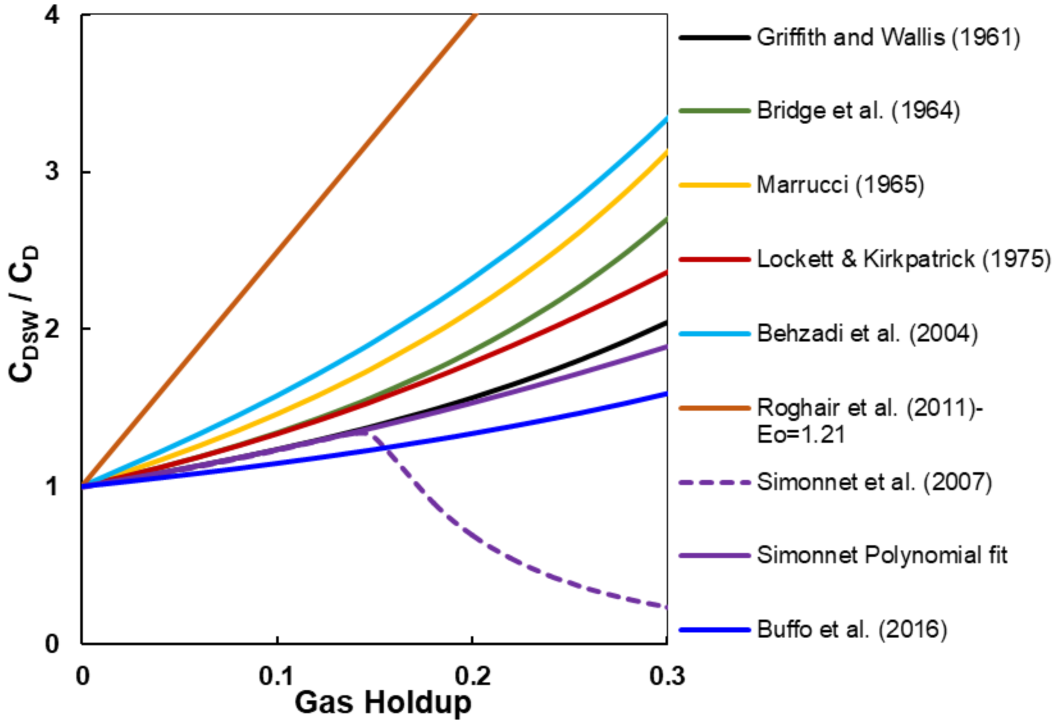

Figure 3.6 Graphical representation of several swarming drag correction models.

Most of the aforementioned investigations dealing with the effect of adjacent bubbles were conducted assuming the mono-disperse in the column. This is not very relevant to this work which focuses on estimating polydisperse BSDs in contaminated systems. On the other hand, the recent findings of McClure et al. [2017] put into question much of the common understanding concerning the bubble swarming effect. They used an extensive database of experiments conducted using a well-instrumented pilot-scale bubble column and a wide range of experimental conditions (air-water, Φ_{GLoc} = 0.03–0.38 and $4 < d_B < 10$ mm, polydispersion). The value of the correction term $f(\Phi_G)$ on the bubble relative velocity was found to depend not only on the local volume fraction (which had been assumed by most previous investigators) but also on the mean bubble diameter and the dispersity of the BSD. In their work, no hindered bubble rise was observed over the experimental conditions they examined, which suggested that the bubble crowding effect may be restricted to monodisperse systems with relatively narrow BSDs.

CHAPTER 4 EXPERIMENTAL

In this Chapter, several items related to the experiments (including experimental setup, system investigated, experimental conditions & procedures, measurement techniques, sources of error, and typical steady-state and transient gas holdup results) will be discussed. This was a team effort between several graduate students. The setup was designed by Dr. Al Taweel and benefited from the experience gained from using pilot-scale ALR units. The setup construction was done by Mr. R. Dube (Smart ltd., Timberly NS) and managed by Mr. Idhbeaa, who also managed and completed the startup and commissioning together with me. The Labview data collection and control program was designed by Mr. Idhbeaa with assistance from Mr. S. MacKinnon. The experiments were designed and implemented as a group effort between three graduate students using the facilities discussed below. The information generated by this effort was therefore commonly used by all three students provided proper recognition for the efforts is maintained. As shown in this thesis, the focus of my R&D activities was the development of a software program that can utilize the results generated by the well-known dynamic gas disengagement technique, DGD, to achieve reasonably good estimates of the bubble size distribution in the G/L dispersion maintained throughout the column. This information is critical for developing a good understanding of the impact of various design and operating factors on the characteristics of gas/liquid dispersions. Dr. G. Mazzanti contributed significantly to the computation and program design of the new methodology used for extracting BSDs from the experimentally obtained temporal variation of gas holdups.

4.1 Experimental Setup

4.1.1 Gas-Liquid Contactor

The multipurpose, multi-configurational experimental setup used is schematically depicted in Figure 4.1.

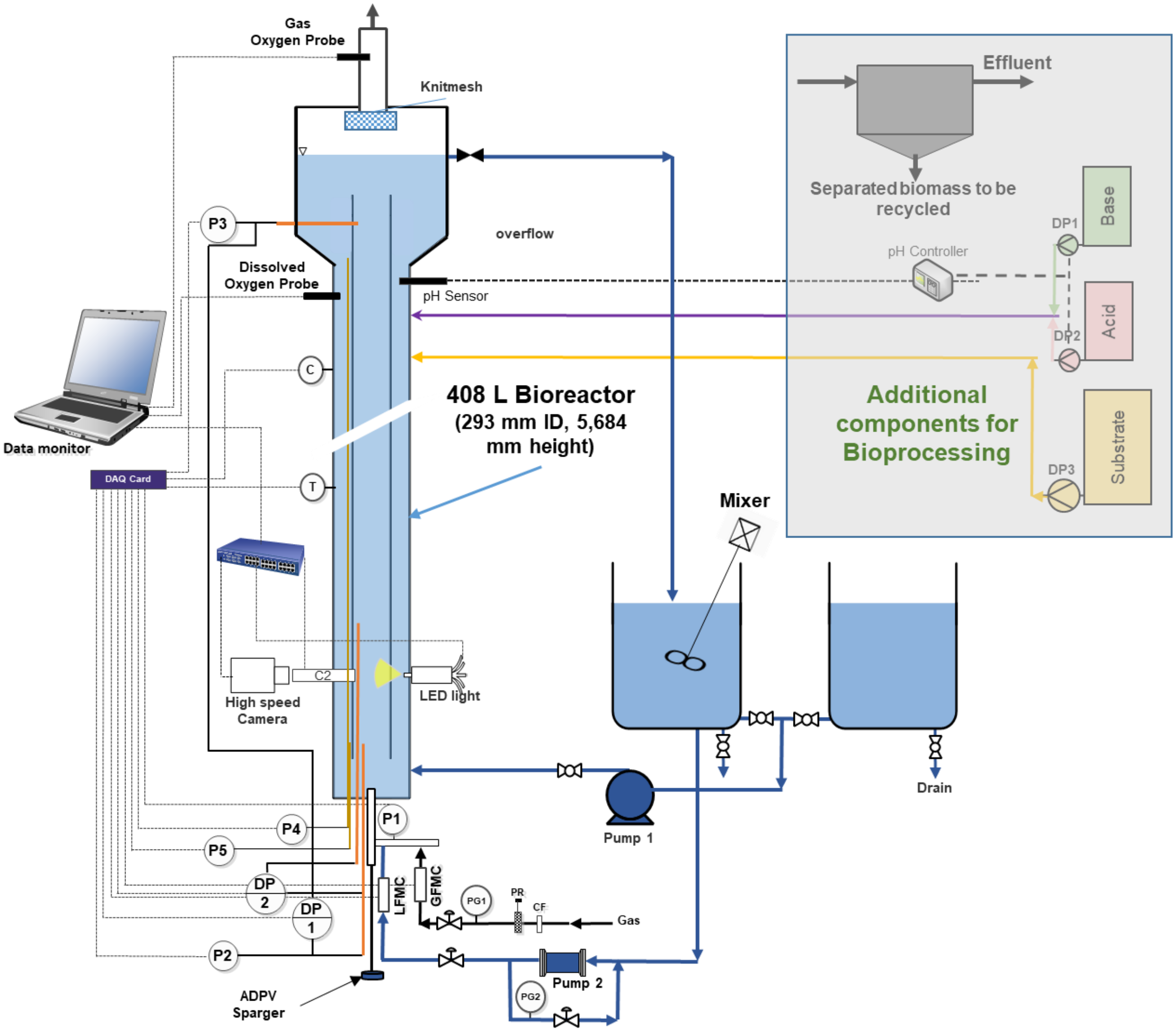

Figure 4.1 Schematic diagram of the gas-liquid contacting setup.

(CF: Carbon Filter; DP1: Differential Pressure Sensor (in the riser); DP2: Differential Pressure Sensor (near the sparger); GFMC: Gas Flowmeter Controller; LFMC: Liquid Flowmeter Controller; P1: Pressure Sensor (at sparger inlet); P2: Pressure Sensor (at the riser inlet); P3: Pressure Sensor (at riser outlet); P4: Pressure Sensor (at the downcomer inlet); P5: Pressure Sensor (at the downcomer outlet), PR: Pressure Regulator; PG 1 & 2: Pressure Gauges; Pump 1: Centrifugal Pump; Pump 2: Positive Displacement Pump; T: Thermocouple).

The G/L contactor, a main part of the setup, is a multi-sectional 408 L pilot-scale pneumatically agitated contactor made of a transparent polyacrylic column in order to allow for visually inspecting the flow patterns in different parts of the column and taking pictures of the bubbles prevailing near the wall. An adjustable dual-phase venturi (ADPV) sparger is used to produce the gas-liquid dispersions in the contactor. This contactor was designed in a fashion that provides a large degree of flexibility that enables it to be operated as:

- Bubble column (Figure 4.3),
- Airlift reactor,
    - Internal loop reactor (Figure 4.1)
    - External loop reactor
- Packed column (with the packing occupying the whole cross-sectional area, or only the downcomer section).

It can also be used as a bioreactor, which can take advantage of the enhanced inter-phase mass transfer to facilitate the dissolution of sparingly soluble gases such as Oxygen, Ozone, Carbon monoxide, Hydrogen, Methane. The setup is, therefore, equipped with three feed tanks and computer-controlled dosing pumps (PULSAtron, LME4TA-PTC1 Serial No: 0601101564; 0602101649; 0506104630, 100 psi, 44 GPD) that can be used to introduce the substrate at the desired flow rate and control the pH in the reactor by the introduction of acid/alkali.

The gas/liquid contactor is made up of four flanged cylindrical sections (1,200 mm high and 293 mm ID, 6.35 mm wall thickness, 12 mm flange thickness) stacked on top of each other and equipped with four 51 mm thick solid inter-flange spacers made from high-density polyethylene (HDPE) (Figure 4.2). The spacers between the sections are used to provide means for introducing various instruments (e.g., probes to measure liquid velocity in the downcomer, pressure transducers, thermocouples, conductivity probes, DO meter sensors as well as ports for observation/photographing) to monitor the hydrodynamic, mixing and mass transfer performance of the G/L contactor at different locations along with the column. A 103 L cylindrical gas-liquid separator (498 mm ID and 476 mm high, provided with a conical bottom (293 mm ID and 108 mm high) and an adjustable-level overflow arrangement) is attached to the top of the column. The exiting gas vent is provided with a port for measuring the oxygen concentration in the gas phase (Optical Oxygen sensor, PreSens Precision Sensing, EOM PG2 PSt3). A knit-mesh separator is installed upstream of the sensor to reduce/eliminate entrained droplets that can affect the accuracy of the oxygen measurements.

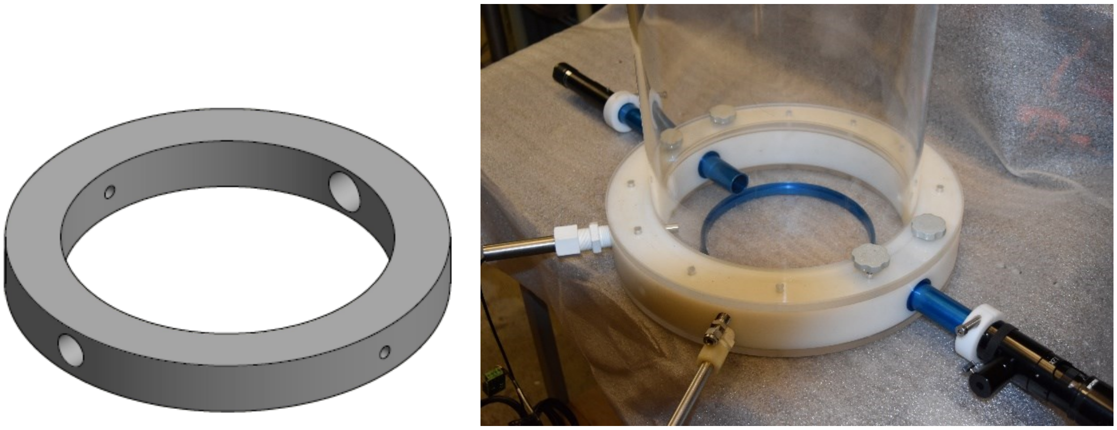

Figure 4.2 The inter-flange spacers (provided with ports to hold a wide variety of instruments at 4 locations along with the height of the contactor).

The level of the overflow port can be changed from 200 to 150 mm below the top of the separator chamber. The height of the liquid in the column can thus be adjusted from 5,484 to 5,534 mm, which results in the overall liquid volume of the gas/liquid contactor varying between 408 to 418 litres when the 293 mm ID column is used, and between 167 to 169 litres when only the 197 mm ID internal column is used.

The bottom of the inner column (riser) is mounted within a specially designed configuration that reduces the friction losses and the generation of shear stresses associated with the flow around sharp corners. This arrangement also allows for adjusting the bottom clearance between the riser and the bottom flange. This, in turn, allows for controlling the liquid circulation rate between the riser and downcomer regions. In all of the investigations conducted in the present study, the bottom clearance was zero, thereby eliminating liquid circulation between the riser and downcomer.

In order to convert the aforementioned setup into an airlift reactor configuration, it is equipped with two 5,300 mm high risers (197- and 248-mm ID). One can, therefore, change the riser to the downcomer flow-area ratio between 0.83 and 2.7

by altering the size of the riser. The geometric characteristics of this airlift reactor configuration are given in Table 4.1.

Table 4.1 Geometric characteristics of the gas-liquid contactor shown in Figure 4.1.

Items	**Contactor Dimensions**	**Units**
Outer Column Diameter, ID	293	mm
Inner Column (Riser) Diameter, ID	197	mm
Riser Height	5,300	mm
Downcomer Height	5,100	mm
Liquid Height in Downcomer	4,900 -5,100	mm
Overall Contactor Height	5,684	mm
Bottom Clearance	0 – 200	mm
Riser Volume	162	litre
Contactor Volume (Column + Separator)	447	litre
Separator Cylinder Height	476	mm
Separator Cylinder Diameter	498	mm
Separator Cone Height	108	mm
Separator Cone Top Diameter	498	mm
Separator Cone Bottom Diameter	293	mm
Height at Liquid Overflow	5,484 - 5,534	mm
Liquid Volume in Contactor	408 - 418	litre
Spacer Thickness	51	mm
Cross-Sectional Area in Contactor	67,391	mm^2
Cross-Sectional Area in Riser	30,465	mm^2

Items	Contactor Dimensions	Units
Cross-Sectional Area in Downcomer	36,926	mm^2

Furthermore, one can investigate the hydrodynamics of bubble columns having a diameter of 197 mm by lowering the riser to a point where no circulation between the riser and downcomer regions is allowed. The schematic drawing of this bubble column used in this investigation is depicted in Figure 4.3. The characteristics are concluded in Table 4.2. Figure 4.4 shows the pictures of this bubble column. All the experiments in the present investigation were done using this bubble column configuration. The gas introduced into the gas/liquid contactor is pre-dispersed using a 25 mm diameter adjustable dual-phase venturi sparger, the top of which is placed 50 mm above the surface of the bottom flange.

Table 4.2 Geometric Characteristics of the bubble column shown in Figure 4.3.

Items	Column dimensions	Units
Column Diameter, ID	197	mm
Column Height	5,684	mm
Column Volume	173	litre
Height at Liquid Overflow	5,484	mm
Liquid Volume in Column	167	litre
Separator Cylinder Height	476	mm
Separator Cylinder Diameter	498	mm
Separator Cone Height	108	mm
Separator Cone Top Diameter	498	mm
Separator Cone Bottom Diameter	293	mm

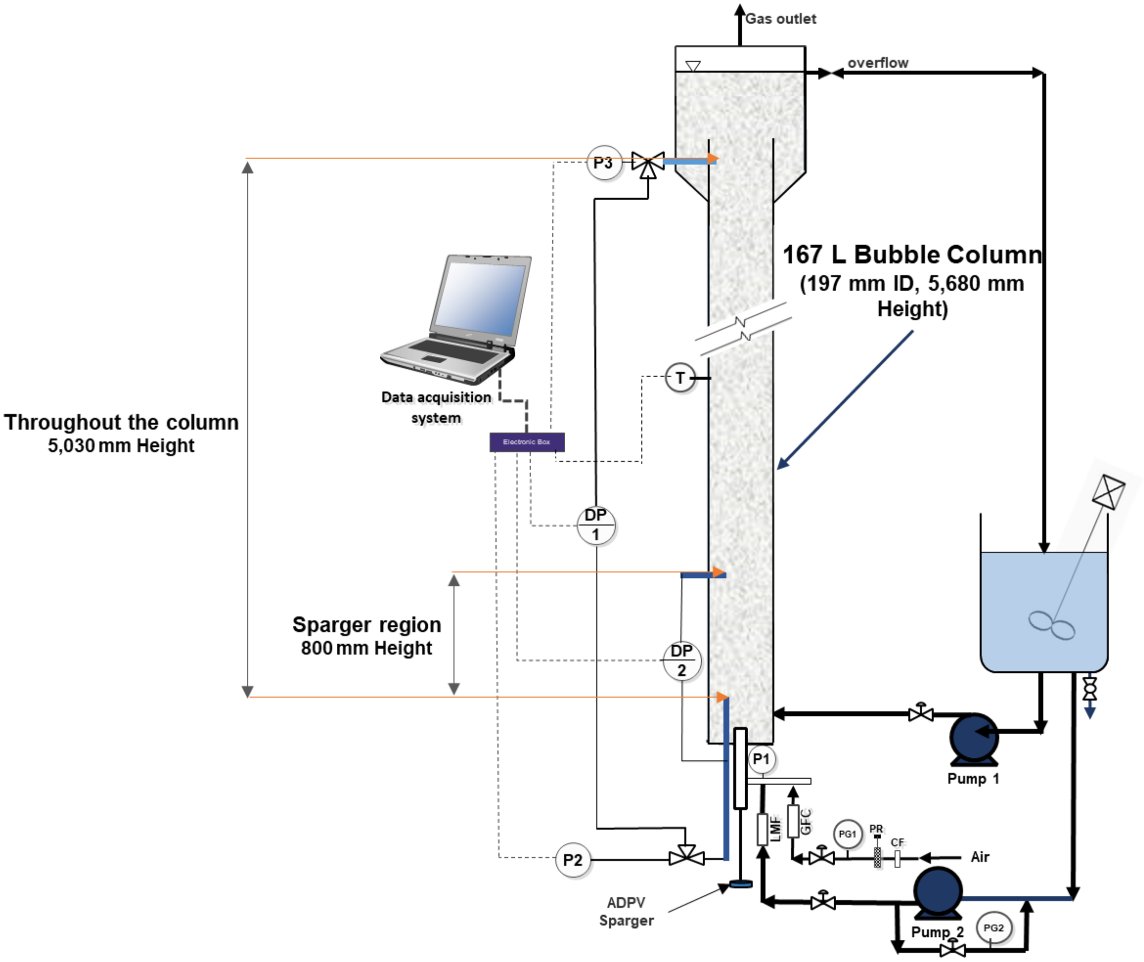

Figure 4.3 Schematic diagram of the pneumatically agitated bubble column.

(CF: Carbon Filter; DP1: Differential Pressure Sensor (in the column); DP2: Differential Pressure Sensor (near the sparger); GFMC: Gas Flowmeter Controller; LFMC: Liquid Flowmeter Controller; P1: Pressure Sensor (at the sparger inlet); P2: Pressure Sensor (at the column inlet); P3: Pressure Sensor (at the column outlet); PR: Pressure Regulator; PG 1 & 2: Pressure Gauges; Pump 1: Centrifugal Pump; Pump 2: Positive Displacement Pump; T: Thermocouple at the column mid-height.)

Figure 4.4 The bubble column used in the present experiments.

4.1.2 The Adjustable Dual-Phase Venturi Sparger

The original concept of using a venturi-type sparger to generate fine bubbles utilized a fixed-throat venturi [Al Taweel et al., 1996; Ramadan, 1996]. It resulted in the formation of fine bubbles (200 μm ≤ d_{32} ≤ 5,000 μm), achieving very large interfacial areas of contact (*up to* 2,700 m^2/m^3) in a co-currently-operated 100 mm ID bubble column, as well as in maintaining relatively large gas holdups ($\overline{\Phi}_{GC}$ up to 0.20 at U_G = 12.4 mm/s) in batch liquid flow. The results obtained using different throat diameters operated at a constant trans-sparger pressure drop, suggesting that significantly enhanced gas-phase dispersion can be achieved by using larger throat cross-sectional areas. It was, therefore, desirable to develop a sparger in which the throat area could be continuously adjusted without having to interrupt the operation. This need was addressed by developing a venturi-type sparger in which the cross-section of the circumferential throat can be adjusted by using a regulating rod. By using a screw arrangement, the position of this regulating rod can be adjusted along the axis of the sparger. Consequently, the cross-sectional area of the throat increases as the regulating rod is pushed further into the divergent section of the venturi and decreases as it is pulled back to the throat. Very good gas/liquid dispersion (25 μm < d_{32} < 8,700 μm and interfacial areas up to 5,400 m^2/m^3) was achieved by using this new design in the presence of 50 ppm of SDS [Luo, 2002]. The same sparger was also recently used to experimentally investigate the hydrodynamic factors affecting bubble coalescence in tap water [Luo & Al Taweel, 2017].

The 25 mm ADPV sparger used in this investigation is a modified version of the 12.5 mm ADPV sparger developed for the multiphase mixing and separation lab and used for inline aeration purposes [Al Taweel et al., 2003]. In addition to having a discharge opening of 25 mm instead of 12.5 mm in the previous one, the throat length was increased from 15.2 mm to 25.4 mm while keeping the same angle from the vertical. The ability of this sparger to enhance inter-phase mass transfer was assessed using a 200 L pilot-scale (2.5 m high) airlift reactor, and the results obtained showed significant improvement of the hydrodynamic and mass transfer performance of the ALR. The effect of two contaminants (SDS and Salt) on the hydrodynamic and mass transfer performance of the ALR was investigated. High gas holdups ($\overline{\Phi}_{GR} \leq 0.2$ at U_{GMidH} = 28.5 mm/s), good liquid phase mixing rates (liquid circulation velocity, $U_{LR} \leq 1.5$ m/s at U_{GMidH} = 28.5 mm/s), and elevated volumetric mass transfer coefficients ($k_La \leq 0.14\ s^{-1}$ at U_{GMidH} = 28.5 mm/s), were achieved using this innovative approach in the presence of contaminants [Pallapothu, 2006; Idhbeaa, 2009; Pallapothu & Al Taweel, 2012; Al Taweel et al., 2013].

Since a significant part of the pressure drop across the ADPV sparger is expected to stem from the energy losses as the gas-liquid dispersion flows through the narrow throat, it was decided to investigate the effect of reducing the length of the venturi throat on the sparger performance [Idhbeaa et al. 2022, In Preparation]. As seen from Figure 4.5, this was accomplished by reducing the throat length from 25.42 mm to 12.72 mm then further down to 6.36 mm.

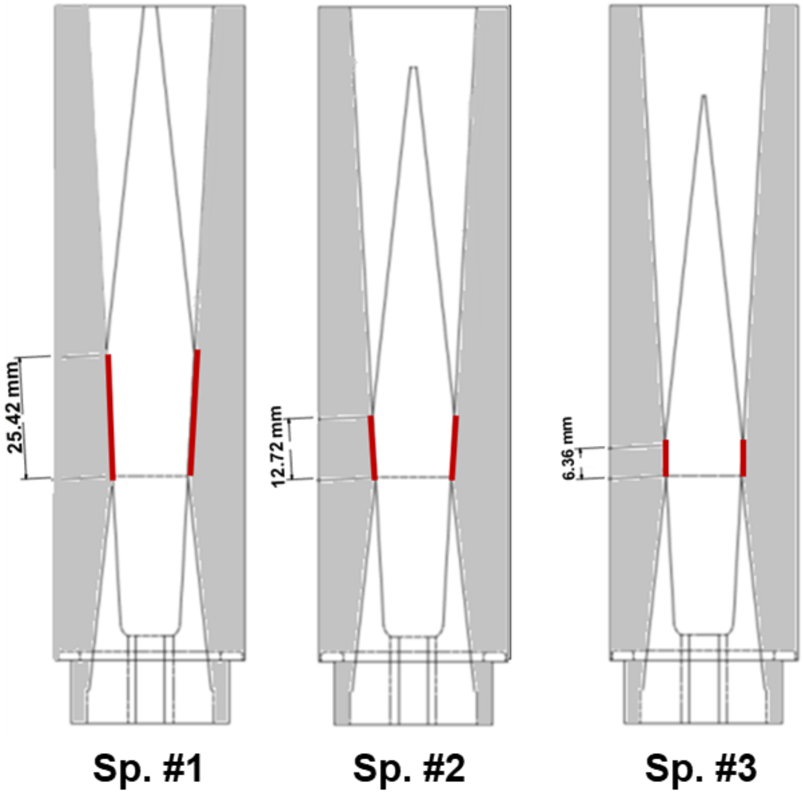

Figure 4.5 Diagram of the ADPV sparger with different throat lengths.

As shown in Figure 4.6, three different inner cone geometries were made to assess the impact of varying the length of the circumferential throat on the characteristics of the G/L dispersion generated. The geometrical configuration of the circumferential gap used in this investigation to generate microbubbles is significantly different from the tubular geometry used by virtually all previous investigators [Anastasiou et al., 2010; Passos et al., 2015 McClure et al., 2016; Besagni & Inzoli, 2017]. Whereas previous investigators used a constant rectangular, or round, cross-sectional area, the throat geometry encountered in the ADPV sparger is ring-shaped, the diameter and CSA of which varies as the flow progresses downstream along the length of the throat. Furthermore, the CSA of flow can be manually or automatically controlled by moving the adjustment rod inwards or outwards. This allows for a broader operating range while predispersing the gas. A physical expression of the ADPV sparger used in this investigation is shown in Figure 4.7.

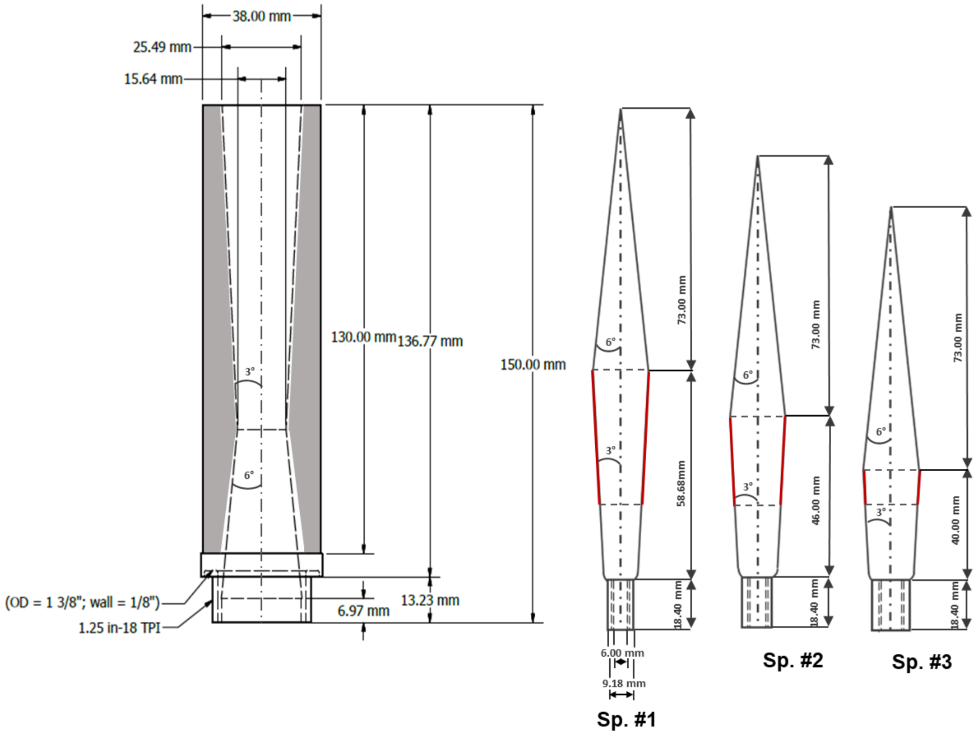

Figure 4.6 Dimensions of the three adjustable regulating rods and the encasing section.

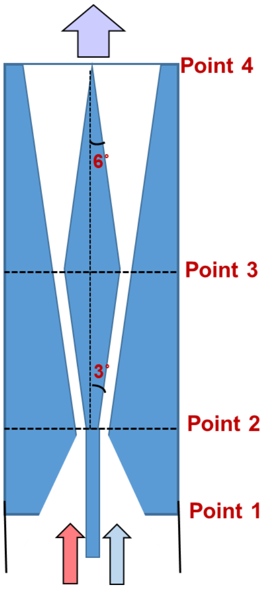

Figure 4.7 Physical expression of the sparger (Point 1: Sparger entrance; Point 2: Throat entrance; Point 3: Throat exit; Point 4: Sparger exit).

A simple program was, therefore, developed to calculate the hydraulic equivalent diameter of the circumferential gap under different operating and design conditions. Figure 4.8 depicts the equivalent geometry of the ADPV sparger varies throughout the whole sparger, (a) is for the geometric equivalent diameters and (b) is for hydraulic equivalent diameters. The calculations for different equivalent diameters of the ADPV sparger are presented and discussed in Appendix A. The EXCEL program performing such calculations ("Calculations of Sparger Parameters") was incorporated as a part of the software used for analyzing and interpreting the data collected. This parameter allows for comparison with the results obtained by other investigators using fixed throat spargers.

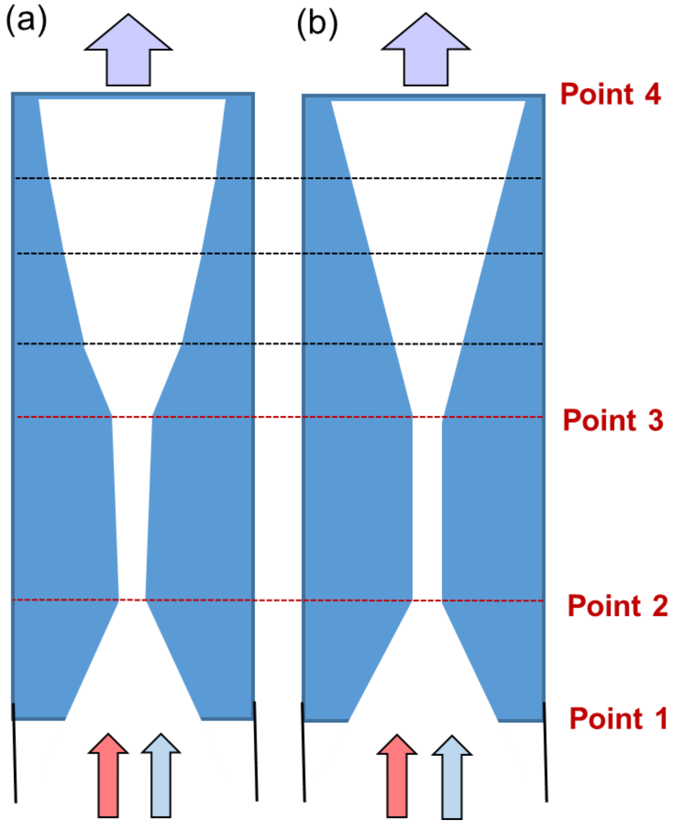

Figure 4.8 Equivalent geometry of the sparger modified from Figure 4.6, (a) geometric equivalent diameters, (b) hydraulic equivalent diameters. (Point 1: Sparger entrance; Point 2: Throat entrance; Point 3: Throat exit; Point 4: Sparger exit; black dotted lines: diameters at any locations in the divergent section).

In a fashion similar to that reported by Ramadan [1996] and Luo [2003], the pressure drop across the sparger is affected by:

- The gas flow rate passing through the sparger,
- The liquid flow rate, passing through the sparger (which is determined by the gas to liquid flow ratio, G/L ratio),
- The throat cross-sectional area.

In the case of the ADPV sparger, the latter can be adjusted by moving the regulating rod inwards or outwards, which, in turn, enlarges or decreases the circumferential gap width. As shown in the results given in Chapter 6, this can beneficially impact the generation/maintenance of fine gas/liquid dispersions. The pictures of the ADPV sparger used in the experiments are depicted in Figure 4.9.

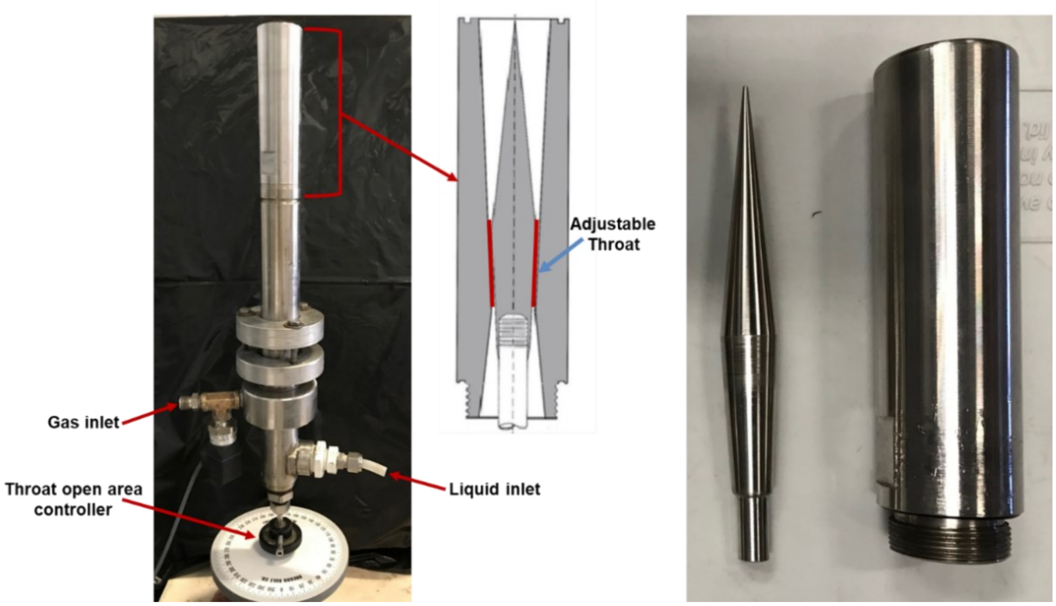

Figure 4.9 Pictures of the ADPV sparger used in the experiments.

4.1.3 Gas and Liquid Feeding Systems

All experimental runs were conducted using the Halifax city water that is relatively low in dissolved solid concentration and total organic carbon. The coalescence-retarding tendency of such water was altered by adding minute amounts of Sodium Dodecyl Sulfate (SDS) ($C_{12}H_{25}SO_4Na$, 288.38 g/mol, Product No. L-5750 Lot # BCBS411V, made by Sigma Chemical Co., 92-100.5 % based on alkyl sulphate basis content), which is well known to alter the gas/liquid interface and retard bubble coalescence [Anastasiou et al., 2010; Pallapothu & Al Taweel, 2012]. The liquid to be tested in any particular experiment was prepared by filling one of the two polyethylene storage tanks shown in Figure 4.1 (500 Liters each) with tap water up to the 490-litre level. Based on the volume of the water added, the necessary amount of the additive SDS was weighed and mixed into the water using an off-center portable mixer (Model No: NS-1VM, TPR, 1/3 HP, 1725 RPM, GREEY Mixing Equipment Limited, LIGHTNIN, Toronto, Canada).

A high-capacity centrifugal pump (Rockingham Hardware Limited; 85 GPM; 85 Psi) is used to fill the columns, circulate liquid through the contactor, with the overflow being returned to the tank. The flow rate of the aqueous solution is manually controlled and monitored using an inline liquid flow meter (GPI US Model No: 01N31GM, 0-95 LPM, ±3% FS). At the end of each series of experimental runs, the whole system (column, storage tanks, interconnecting piping) was drained, and the setup was thoroughly washed at least five times using tap water in order to eliminate the presence of contaminants in the system in a fashion that may affect future runs.

The liquid phase, fed to the ADPV sparger, is delivered at the desired flow rate (varying from 3 to 7 LPM) using a high-pressure positive displacement pump (Thermo Dynamics Ltd, 100 Psi, Model No:111A100F11AA, Procon Pump, 1-8 LPM). The amount of liquid fed to the sparger is measured by a liquid flow meter (Proteus Industries Inc. Model No: 04004SN2 (NEMA 4X), 9.5 LPM, ±1.5% FS). Although the liquid flow rate was controlled manually using bypass and needle valves, the liquid flow was switched on/off automatically to provide an automatic shut-off system for the dynamic gas disengagement (DGD) technique.

The setup is provided to be able to select amongst a wide range of compressed gas sources (e.g., air, N_2, or CO_2). The selected gas is mixed with the desired quantity of liquid and introduced to the contactor through the ADPV sparger. The flow rate of the selected gas is measured using two mass flow meters/controllers (Aalborg GFC 37 0-20 SLMP, ±1.5 % FS and Aalborg GFC 47, 0-100 SLMP,

±1.5 % FS). The reason for using two mass flow controllers with low and high flow ranges is to minimize the experimental error. Therefore, they were connected in parallel in order to be used separately or together to provide the desired range of superficial gas velocities for the experiments and were controlled by the computer. In this regard, by using the LabVIEW program, the user sets the desired mass flow rate enabling the analog output channel to send a signal to the target device, allowing the analog output channel to be supplied with the data obtained.

4.1.4 Instrumentation

As shown in Figures 4.1 & 4.3, the G/L contactor is equipped with a thermocouple (K type Cole-Parmer Instruments, Model: 08404-10, +/- 1.1˚C) to monitor the temperature at the mid-height of the contactor. This parameter is used to calculate and adjust the gas flow rate so that the superficial gas velocity under the mid-height conditions prevailing in the G/L contactor meets the value specified in the input data.

The pressure measurements conducted in the gas/liquid contactor shown in Figure 4.1 were made using several pressure sensors (P1-P5 and DP1) listed in Table 4.3. The average pressure values measured at these locations were used to determine:

- The mean gas holdups and energy dissipation rates achieved in the column, which covers a height of 5,030 mm between two pressure measuring locations in the column (P2 to P3 and DP1),
- The mean gas holdups and energy dissipation rates obtained at the sparger region, which covers a height of 800 mm measured by the differential pressure sensor (DP2). This measurement was driven by the observation reported by Mouza et al. [2005] that the mixing pattern in the region near the fine bubble generator may be significantly different from that encountered throughout the rest of the column.
- Two accurate and sensitive differential pressure transducers (DP1 and DP2) were also used to measure the temporal variation of gas holdups

within the aforementioned two regions of the column. The outputs as a function of time were used to estimate BSDs using the DGD technique.

Table 4.3 Details of pressure measurement instrumentation.

Sensor Symbol	Model NO. and range	Measuring Location	Accuracy
P1	Pressure Transducer Wika, Germany, A-10, S# 1A001DTLF2Z, 0-60 psig	Sparger Inlet	±0.5% FS
P2	Cole-Parmer, RK-68075-42, 0-10 psig	the inner column, 200 mm above the bottom flange	±0.25% FS
P3	Honeywell, FPG2AT,2D5B6Q, 060-E748-09, 0-5 psig	the inner column, 5,300 mm above the bottom flange	±0.25% FS
P4	Honeywell, FPG2AT, 2D5B6Q, 060-E748-09, 0-5 psig	outside the inner column, 5,300 mm above the bottom flange	±0.25% FS
P5	Cole-Parmer, RK-68075-42, 0-10 psig	outside the inner column, 200 mm above the bottom flange	±0.25% FS
DP1	Omega, PX409-005DWUV, 0-5 psig	Differential pressure between the locations of P2 & P3.	±0.08% FS
DP2	Omega, MMDWB10WBIV10P3C6T1A2CE, 0-0.36 psig	Differential pressure between the location of P2 and 1,000 mm above the bottom flange (inside the inner column)	±0.08% FS

In order to achieve accurate measurements of the temporal variation in pressure differences, it is essential to use a pressure sensor with the proper response time, especially in cases where the measured pressure changes rapidly. Therefore, rapidly-responding absolute pressure transducers (with a response time of 10 ms) were used to measure the hydrostatic pressure at the riser inlet (P2) and outlet (P3).

The differential pressure transducers used to measure pressure fluctuations have a response time of less than 1 ms. The justification for choosing the 1 ms sensor at the sparger region stems from the fact that the sudden change in the flow from the smaller sparger diameter to the larger bubble column diameter will induce faster pressure change characteristics. Whereas the choice of the 10 ms sensor stems from the fact that in the whole column, the flow is reasonably uniform to minimize more rapid pressure change characteristics. Signals from the two types of differential pressures were used to identify the flow regime transitions using several techniques, such as statistical analysis of the signal (mean, variance, standard deviation), bubble average swarm velocity method, drift flux method. It will use the extensive database of experimental results (each run having 30,000 pressure differential data points collected at the rate of 100 Hz).

4.1.5 Data Acquisition System

The experimental setup is connected to a computer/data acquisition and control system that facilitates the conduct of the experiments at the desired pre-set experimental conditions. It also records the values of several manually-adjusted operating parameters as well as the temporal variation of the various parameters during the steady-state operation as well as during the DGD run. This was accomplished using three National Instruments data acquisition boards.

The first board is NI PCI-E-6321, with 16 analog input channels and 2 analog output channels, with a sampling rate of up to 250 k samples/s and a resolution of 16-Bit, 24 DIO. The second one is a NI USB-6001 with 8 analog input channels and 2 analog output channels, with a sampling rate of up to 20 ksamples/s and a resolution of 14-Bit,13 DIO. The differential pressure signals obtained from DP1 and DP2 were samples using the National Instruments board NI-9237, 4 AI, operating at the rate of 50 k samples/s. These are used to acquire the signals from the sensors/instrumentations and interface with the PC.

A computer program was developed in the LabVIEW that reads the input data (run number, operator, date, contactor type, sparger number, set point for the desired gas flow rates, SDS concentrations) and accordingly sets the operating conditions in the unit (superficial gas velocities, liquid flow rates, G/L ratio, pressure drops across the sparger (ΔP_{Sp}), cross-sectional area of the throat of the sparger (A_{Th})). A typical example of the input datasheet for a regular run is provided in Appendix B. A few operating parameters (liquid flow rates, ΔP_{Sp}, and A_{Th}) had to be manually adjusted. For instance, ΔP_{Sp} had to be adjusted by changing the axial location of the regulating rod of the sparger, and consequently, A_{Th}.

The output signals from 11 points in the setup (i.e., gas flow rates, liquid flow rates, riser inlet pressure, riser outlet pressure, downcomer inlet pressure, downcomer outlet pressure, the pressure at sparger entrance, differential pressure obtained throughout the column, differential pressure obtained at sparger region, and mid-height temperature, conductivity) are continuously monitored at an adjustable rate. Their corresponding values are stored on the hard drive in Excel files. For example, during the initial steady-state period, the signal representing the pressure difference for the whole column was monitored at the rate of 100 Hz in order to enhance the accuracy by which advanced signal processing techniques (e.g., information entropy concept and the Kolmogorov entropy algorithm) can be used to identify the flow rate at which transition from homogeneous to heterogeneous flow takes place. On the other hand, excessive pressure fluctuations are detrimental to accurately estimating the BSDs using the DGD technique. Although the data collection system must respond rapidly to the monotonic variations in the hydrodynamic pressure difference (up to 250 kHz for DQ1, 20 kHz for DQ2, and 50 kHz for DQ3), the data acquisition/storage rates were reduced to 60 Hz in order to reduce data manipulation effort (corresponding to the blue lines shown in Figure

4.10) This resulted in lowering some of the differential pressure signal noise, as well as some of the fluctuations stemming from the operating system.

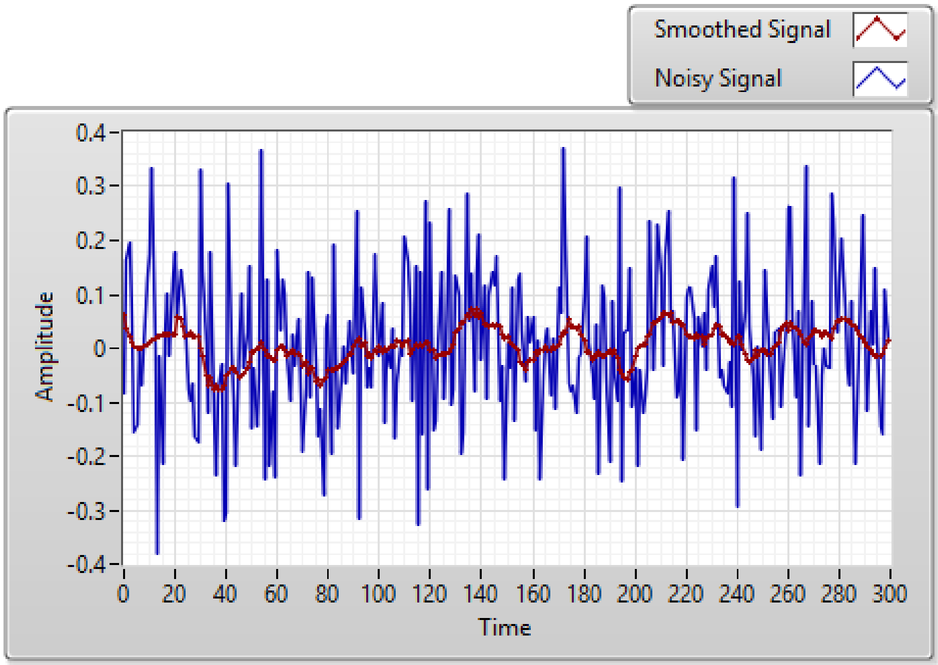

Figure 4.10 Typical example of both unsmoothed pressure signals and smoothed pressure signals.

The data shown in Figure 4.10 depict both the original pressure differential signal data (collected at the rate of 60 Hz), as well as the time-smoothed signal (generated by taking a moving average of 100 data points collected at a frequency of 60 Hz, i.e., over a time interval of 1.5 s). This was accomplished with the help of a built-in subroutine that is available in LabVIEW “Configure Filter sub VI”. Although an additional reduction in the fluctuations can be achieved by prolonging the time interval over which the moving average is taken, this may result in unnecessary damping of the rapid changes in pressure fluctuations.

4.2 Systems Investigated

Tap water from the city of Halifax was used throughout this investigation because of its relatively low dissolved solids (A typical analysis of which is presented in Appendix C). However, minute quantities of an anionic surfactant (0 to 100 ppm; Sodium Dodecyl Sulfate, SDS) were added to the tap water to simulate the coalescence retardation phenomenon encountered in most industrial and natural streams. The SDS ($C_{12}H_{25}S0_4Na$) used was supplied by Sigma Chemical Corp. (Product No. L-5750 Lot # BCBS411V) is 92-100.5 % based on an alkyl sulphate basis content. This chemical was chosen because it is the most common surfactant encountered in virtually all wastewater treatment plants. It is also commonly used to test the effect of interfacial properties on the performance of gas-liquid contactors [Al-Masry & Dukkan, 1997; Al Taweel et al., 2003; Moraveji et al., 2012], and its static and dynamic interfacial properties are well known (Table 4.4). Six levels of the surfactant concentrations were used in the experiments conducted in this investigation.

4.3 Experimental Conditions & Procedures

In order to meet the needs of the three graduate students involved in this study, a total of 508 experiments were conducted covering a broad range of conditions in order to properly assess the effect of various design and operating factors on the hydrodynamic characteristics of the gas-liquid dispersions generated by the ADPV sparger, as well as that maintained in the bubble column. Of these, about 313 DGD experiments were conducted under various experimental conditions, which were used to estimate BSDs at different column regions (across the column and sparger region). In order to identify the flow regimes in the whole column, 56 experiments were conducted. Furthermore, around 90 experiments (5 replicates conducted under 18 different conditions) were conducted to determine the reproducibility of the gas holdup measurements and corresponding BSD results. The ranges of each parameter investigated in this work are shown in Table 4.5. All the DGD experiments analyzed in this investigation were conducted using the ADPV Sparger with a throat length of 6 mm.

Table 4.4 Static and dynamic interfacial characteristics of dilute aqueous SDS solution (in Tapwater) [Luo, 2002].

SDS Conc., ppm	**0**	**2**	**5**	**10**	**20**	**50**
C_0, mM	0.0	0.00694	0.0173	0.0347	0.105	0.173
σ_∞, mN/m	72.0	66.2	64.1	61.4	47.8	44.1
Π, mN/m	0.0	5.8	7.9	10.6	25.2	27.9
Γ_G, 10^{-6} mol/m^2	0.0	0.506	1.01	1.50	1.92	2.25
Γ_∞, mol/m^2	4.18×10^{-6}	4.18×10^{-6}	4.18×10^{-6}	4.18×10^{-6}	4.18×10^{-6}	4.18×10^{-6}
Expression for σ_t, N/m (0.08 s< t< 6 s)	σ_t = 0.072	$\sigma_t = 0.0657 + 9.50\times10^{-4}\, t^{-0.5}$	$\sigma_t = 0.0638 + 9.10\times10^{-4}\, t^{-0.5}$	$\sigma_t = 0.0609 + 10.1\times10^{-4}\, t^{-0.5}$	$\sigma_t = 0.0471 + 11.4\times10^{-4}\, t^{-0.5}$	$\sigma_t = 0.0433 + 12.8\times10^{-4}\, t^{-0.5}$
$d\sigma_t/dt^{-1/2}$	0	9.50×10^{-4}	9.10×10^{-4}	10.1×10^{-4}	11.4×10^{-4}	12.8×10^{-4}
Γ_L, 10^{-6} mol/m^2	0	0.208	0.323	0.480	0.98	1.21
Maximum elasticity	0.0	2.8	3.2	5.1	8.7	13.7

Table 4.5 Range of experimental conditions tested.

Design/operating parameter	Range	Unit
L_{Th}	6, 12, 25	mm
A_{Th} (Applicable only to constant throat CSA tests)	11, 22, 33	mm^2
U_G	0.5 – 50	mm/s
Q_{LSp}	3 – 7	L/min
C_{SDS}	0 – 50	ppm
ΔP_{Sp} (Applicable only to constant throat ΔP tests)	210 – 350	kPa
G/L vol. ratio	0.2 – 16	-
Φ_{GZ1}	0.2 - 35.4	%
Φ_{GZ2}	0.15 - 35.1	%

The steps involved in running a DGD experiment are shown in the logic flow diagram below (Figure 4.11). The overall experimental run involved data collection under steady-state operation followed by collecting data under the non-steady conditions associated with the DGD testing. In this investigation, the focus is on the analysis of the DGD data. Detailed analysis of the data collected within the DGD segment is discussed in Chapter 5.

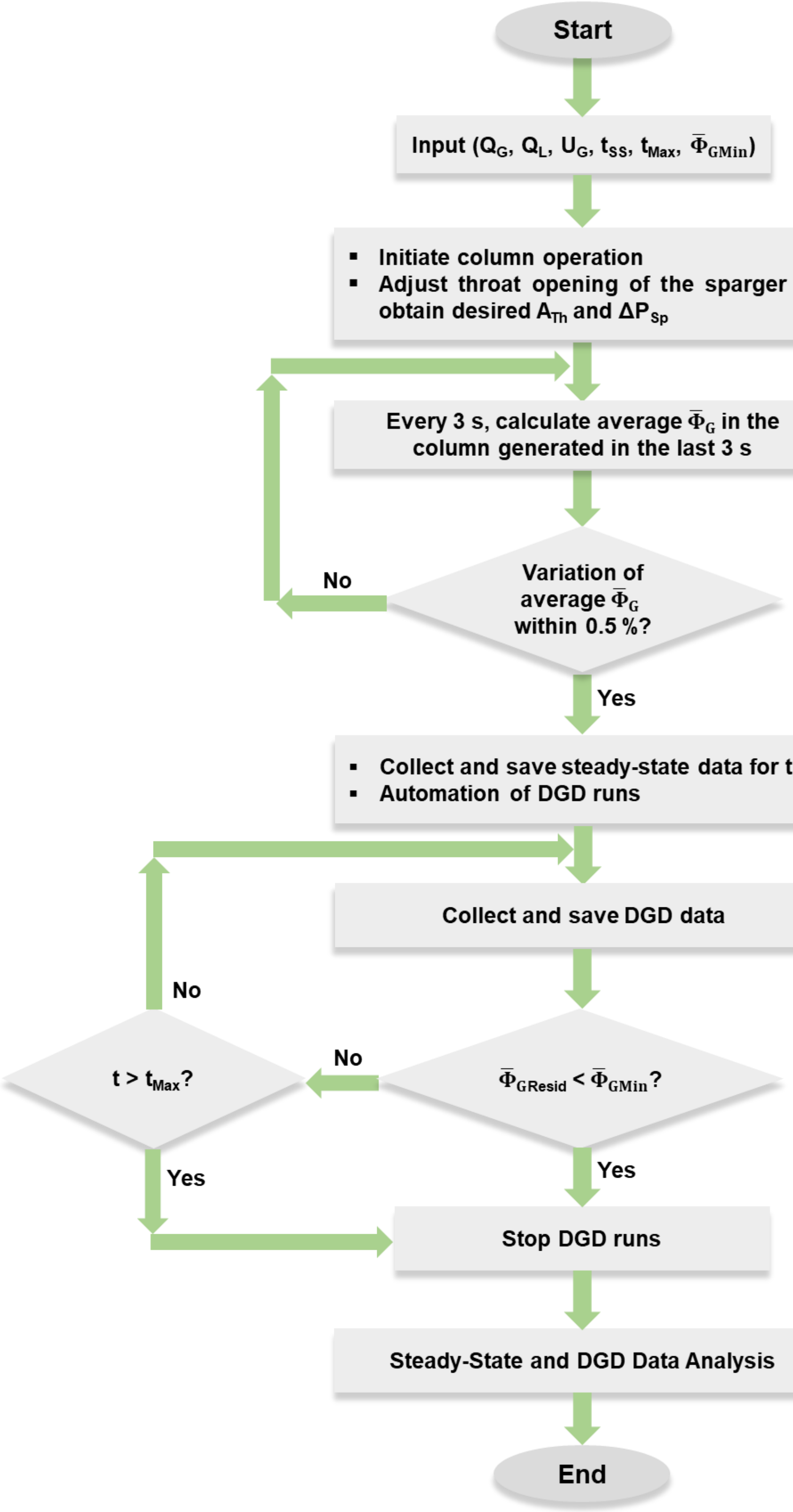

Figure 4.11 Logic flow diagram of data collection & analysis program.

4.4 Measurement Techniques

In this section, the methods by which gas holdups were calculated from the measured parameters (average and time-dependent pressure values measured at two regions in the column) will be discussed.

During the DGD experiments, the dynamic changes of the pressure difference were measured by the differential pressure sensors (DP1 and DP2). The gas holdups of each region were calculated by the pressure differences measured at that region, liquid density, gas density corrected by the mid-height conditions of that region, as well as the dispersion height of that region. The expressions are shown below:

$$\Phi_{GC} = \frac{\Delta P_C}{(\rho_L - \rho_{GC}) \cdot g \cdot H_{DispC}} \tag{4.1}$$

$$\Phi_{GSR} = \frac{\Delta P_{SR}}{(\rho_L - \rho_{GSR}) \cdot g \cdot H_{DispSR}} \tag{4.2}$$

4.5 Sources of Error

In the experiments, several sources of error can result from the measuring instrumentations, including gas mass flow controllers, the liquid mass flow meter, thermocouples, differential pressure transducers and absolute pressure transducers. The errors produced by these measuring instrumentations are listed in Table 4.6.

Table 4.6 Errors generated by measuring instruments.

Instrument	Measuring Range	Error
Gas Flowmeter Controller (GFC 1)	0 – 100 L/min	± 1.0 % FS
Gas Flowmeter Controller (GFC 2)	0 – 20 L/min	± 1.0 % FS
Liquid Flow Meter	0- 10 L/min	± 1.5 % FS
Thermocouple (K type)	-58 – 1999˚F	± 4.7 ˚F

Instrument	Measuring Range	Error
Pressure Transducer (P1)	0-60 psi	± 0.5 % FS
Pressure Transducer (P2)	0-10 psi	± 0.25 % FS
Pressure Transducer (P3)	0-5 psi	± 0.25 % FS
Differential Pressure Transduce (DP1)	0–5 psi	± 0.08 % FS
Differential Pressure Transducer (DP2)	0–10 inch	± 0.08 % FS

4.6 Typical Steady-State & DGD Gas Holdup Results

Figure 4.12 depicts typical test results obtained under homogeneous and pseudo-homogeneous conditions for both the steady-state and the DGD periods.

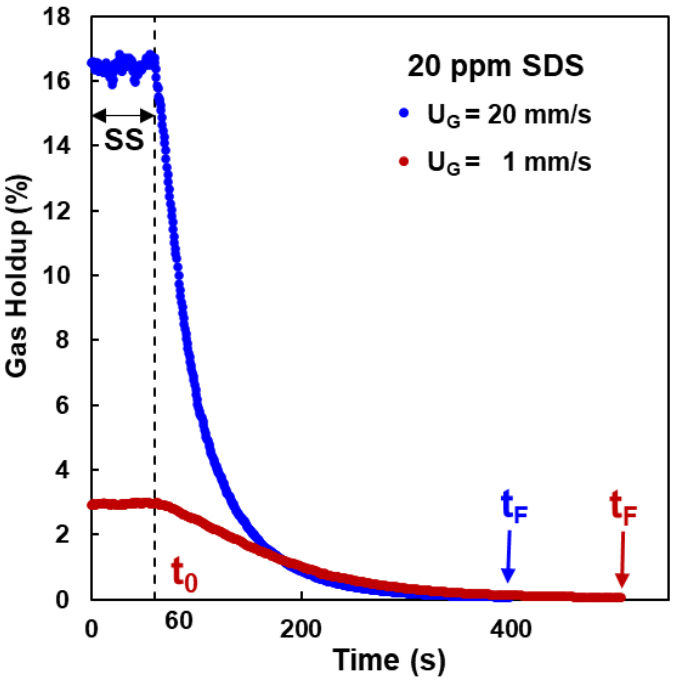

Figure 4.12 Typical steady-state and DGD results obtained across the column (C_{SDS} = 20 ppm, ΔP_{Sp} = 210 kPa, Q_L = 7 L/min)

CHAPTER 5 AN ADVANCED METHOD FOR ANALYZING DGD DATA

The dynamic gas disengagement technique, DGD, was introduced by Sriram and Mann in the late 1970s and has since been used to estimate the bubble size distribution encountered in gas-liquid contactors operating in the homogeneous and heterogeneous flow regimes. With few exceptions, it classifies the BSD into two to three main classes (namely coarse and fine or large, middle and small), a simplistic approach that is extensively used in many CFD analyses. It is based on relatively simple assumptions, and its accuracy was significantly improved by taking into account the effect of the downward-moving liquid flow needed to compensate for the volume of gas disengaged [Schumpe & Grund, 1986]. A general approach for extracting multi-class BSD from the DGD results was developed by Patel et al. [1989] and used by Daly et al. [1992] and Basha and Morsi [2018] to determine multi-class BSD encountered in pilot-scale bubble column reactors filled with relatively viscous paraffin wax. To enhance the accuracy and reliability of this technique, several investigators recently combined electrical resistance tomography (ERT) with the DGD technique to gain better insight into the gas holdup present in the vessel and its axial and radial distribution. This enhancement helped identify the practical limits beyond which the fundamental assumptions on which the DGD technique is based are not met [Adetunji & Rawatlal, 2018; Khalili et al., 2018; Basha & Morsi, 2018; Kazemzadeh et al., 2018; Tao et al., 2019]. However, it is interesting to note that most of these investigations yielded BSD based on only 2 or 3 classes, even with such sophisticated equipment.

Recently, some investigators used CFD to analyze the DGD and ERT data and achieved reasonably good estimates of the BSD and the bubble breakage/coalescence rates throughout the column [Adetunji & Rawatlal, 2018; Kazemzadeh et al., 2018; Tao et al., 2019]. Adetunji & Rawatlal [2018] used population balance modelling, in combination with the experimental ERT measurements, to interpret their DGD data and develop BSD estimates. This provided a clearer insight into the mechanisms involved. Unfortunately, their gas holdup data clearly show that their measurements were conducted in the expanding jet region, where a very large radial variation in the gas holdup exists. This violates one of the fundamental foundations upon which the DGD technique is based (namely radially uniform gas holdups). The limited information concerning the factors involved in analyzing and interpreting the data in real industrial systems is most probably the main factor responsible for the difficulties observed in the work of Tao et al. [2019]. Although the BSD was represented by only two or three classes, both the bubble drag model and the maximum stable bubble size had to be empirically modified to achieve good correspondence with the experimentally determined holdups.

Unfortunately, most previous investigations were conducted using rapidly-coalescent systems (typically deionized water or tap water) in columns operated under conditions where heterogeneous flow regimes prevail. Consequently, the BSD encountered in the gas/liquid dispersions are typically reported as the volume fractions corresponding to only two bubble sizes, namely, coarse and fine bubbles. Few authors tried to enhance the technique's capabilities, but the overall limitations to its widespread use in conjunction with small bubbles are still significant.

On the other hand, the recent findings of Basha and Morsi [2018] used the DGD technique to provide extensive information concerning the factors affecting the BSD achieved in slurry bubble column reactors. Special attention was focused on the catalytic Fischer-Tropsch process, which is operated in the churn-turbulent flow regime. The approach used by these investigators is based on an estimate of the maximum stable bubble size that can be achieved in turbulent flow encountered in a mechanically agitated slurry reactor. It then uses an iterative energy balance algorithm that is based on the transient experimental pressure drops and the forces exerted on bubbles in the disengagement cell. BSDs were described using log-normal distribution functions, and the mean and variance were determined for each DGD of 720 runs. The mean and variance of the log-normal distribution were correlated as functions of the system's physical properties and operating conditions and were used to predict d_{32} values with an absolute average relative error of ≈12%. Unfortunately, the "Maximum Stable Bubble Size" criterion used by these investigators to estimate the largest bubble size in the distribution is very difficult to predict, particularly in the case of industrial streams, because of the impact of contaminants have on interfacial elasticity.

The approach developed in this investigation builds on the work done by several previous investigators and takes into consideration the rapidly improving understanding of the hydrodynamic and interfacial factors affecting bubble dynamics. It uses a modular approach for selecting the models describing the drag on bubbles and how it is affected by the presence of contaminants and adjacent bubbles (i.e., gas holdup); thus providing the flexibility of using a wide base of fundamental information that enables for its use over a wide range of contaminated systems.

5.1 Assumptions Involved in the DGD Data Analysis

Conventional methods for analyzing DGD data are based on three main assumptions:

1. The gas holdups corresponding to different size classes/fractions of bubbles are assumed to be uniformly distributed throughout the column prior to gas flow interruption.
2. No bubble coalescence or breakup takes place during the gas disengagement test,
3. The disengagement rate of each bubble size class is constant throughout the whole disengagement process. This corresponds to the assumption that all bubble classes disengage independently of any other bubble classes.

In general, the ability to meet these assumptions is strongly affected by:

- The superficial gas velocity used, which, in turn, determines the flow regime, local energy dissipation rate, and gas holdup prevailing in the column.

- The type of sparger used to disperse the gas feed into bubbles that rise under the action of gravity. This strongly affects the BSD of the dispersion fed at the base of the column.
- The interfacial characteristics of the gas-liquid system. In combination with the previous factors, these characteristics strongly affect the BSD of the dispersion and the rate at which it changes as the gas phase ascends through the column.

Although most previous investigators have adopted the first assumption, many experimental investigations and CFD simulations clearly show the tendency of large bubbles to concentrate near the center of the column. This is usually attributed to the lateral lift forces that push large bubbles rising through a velocity gradient field to move towards the center. However, this problem appears not to play as significant a role in the case of small, contaminated bubbles. Several investigators studied the impact of lift forces on the radial distribution of gas holdup and found it approached zero for small bubble sizes, particularly at high contaminant concentrations where small Reynolds numbers are encountered [Takagi and Matsumoto, 2011; Hayashi and Tomiyama, 2018; Shi et al., 2020; Hessenkemper et al., 2022]. This is supported by the recent observation [Idhbeaa et al., 2022, In Preparation] that most of the experiments conducted in the present investigation are in the true-homogeneous or pseudo-homogeneous flow regimes. Under such conditions, the flow patterns in the column are determined by the primary bubble size formed at the sparger and by the coalescence-retarding characteristics of the gas/liquid systems [Nedeltchev, 2020]. The turbulence is mainly attributed to bubble drag, resulting in a liquid microcirculation, gentle agitation of the gas-liquid dispersion, and the consequent formation of a radially uniform gas holdup profile. This situation is very similar to that observed by Besagni and Inzoli [2016] at very low superficial gas velocities, where the BSD encountered in the column's core is not significantly different from that present near the walls.

The second assumption on which the traditional DGD technique is based suggests that no bubble coalescence or breakup takes place during the gas disengagement test. This requirement is very hard to fully meet since all gas-liquid dispersions are thermodynamically unstable, and the bubbles tend to break up and coalesce as they ascent throughout the column, under the influence of the turbulent field present in the liquid phase. However, the second DGD requisite can be approached under conditions where bubble breakage and coalescence rates are very small. In the present investigation, such conditions are met in situations where the gas feed is pre-dispersed into small bubbles (d_B < 3,500 μm), and the superficial gas velocity is kept sufficiently low to maintain homogeneous or pseudo-homogeneous flow conditions. The very mild turbulence generated under such conditions is mainly attributed to bubble drag and the gentle agitation of the gas-liquid dispersion. It thus results in low bubble collision frequencies and lower bubble coalescence efficiencies. This situation contrasts with the large bubble breakage/coalescence rates encountered in most conventional bubble columns studies. These are often operated using slightly contaminated systems (e.g., deionized water or tap water), and large bubbles are typically formed using perforated spargers. Highly-turbulent heterogeneous flow conditions are typically encountered at the high U_G values used in such situations, and the resulting large energy dissipation rates result in accelerating bubble breakage/coalescence rates [Camarasa et al., 1999; Mouza et al., 2005; Besagni & Inzoli, 2017].

The third fundamental supposition on which conventional DGD data analysis assumes that the disengagement rate of each bubble size class is constant throughout the whole DGD process. This corresponds to the assumption that all bubble classes disengage independently of any other bubble classes surrounding them no matter what their concentration is. Because of the idealized concept, some investigators argued that the small bubbles present in a bimodal bubble size distribution (coarse and fine bubbles) could only disengage after the large bubbles are completely disengaged (usually referred to as sequential disengagement) [Vermeer & Krishna, 1981; Kumar et al., 1998]. However, this demarcation between large and small gas bubbles is subjective and was found to underestimate the gas holdup of the small bubbles, particularly those that get drawn into the wake of large bubbles and are disengaged together with large bubbles [Jordan et al., 2003].

Consequently, the third assumption ignores the effect of bubble swarms on bubble rise velocities by most investigators. Because of the mathematical difficulties associated with the more exact representation, few investigators included the effect of gas holdup while calculating the bubble swarm rise velocity in the DGD analysis [Patel et al., 1989; Luo et al., 1996; Urseanu, 2000; Parisien et al., 2017]. However, they used the time-varying average gas holdup throughout the column while accounting for the swarming effect, although it is well known that significant axial variation in gas holdup has been reported.

The axial variation in the gas holdup, and its variation during the DGD run, is clearly shown in Figure 5.1. At the beginning of the DGD process, the gas dispersion is uniformly distributed throughout the column. However, during the DGD run, bubbles of different sizes disengage with varying disengagement rates. Consequently, with the progression of time, the various bubble size classes tend to segregate because of their widely different rise velocities. This is clearly shown in the RHS of Figure 5.1, where the gas holdup observed at the lower regions of the column (mostly composed of fine bubbles) are much smaller than those encountered near the top of the column (which has a wider range of bubble sizes).

Consequently, the approach adopted in the present investigation addresses many of the shortcomings associated with previous investigators by taking into account both the temporal and axial variation of the gas holdup associated with various bubble size classes as well as the downward liquid velocity that is driven by bubble disengagement. For situations where the first aforementioned two assumptions are satisfactorily approached, the use of the newly-developed approach will provide bubble size estimates that are close to those obtained using CFD analysis, particularly when a relatively large number of bubble size classes are used. Details concerning this methodology are provided in section 5.2.

Figure 5.1 Gas structures in the column at different stages of the DGD process.

5.2 Procedures for Estimating Bubble Size Distributions from the Measured DGD Data

In order to estimate BSDs from the experimentally measured DGD data (varying gas holdup as a function of time), a series of algorithms were developed as automated as possible in Excel VBA. The overall logic flow diagram is shown in Figure 5.2.

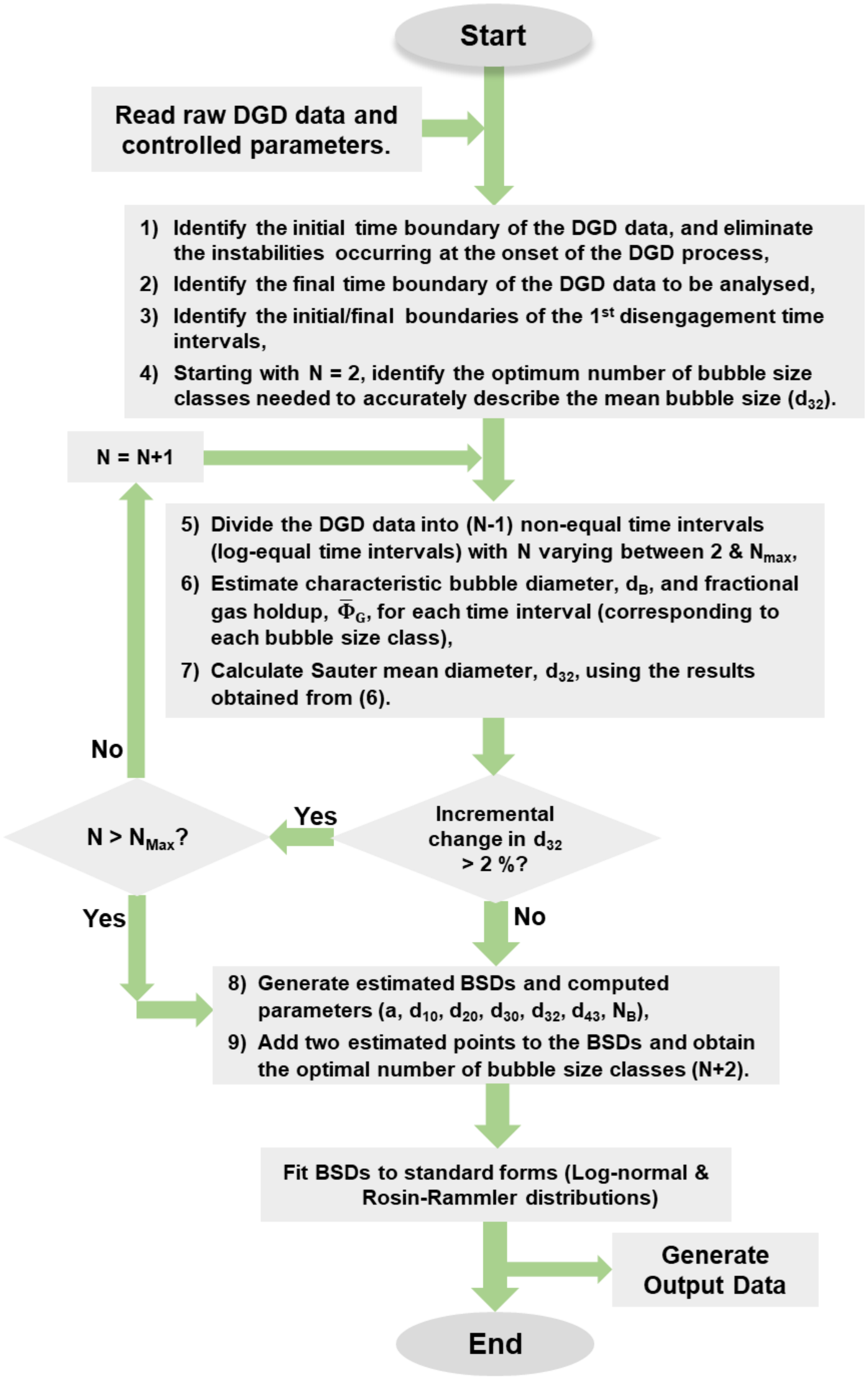

Figure 5.2 Logic flow diagram of the DGD data analysis program.

A list of inputs, as shown below, was used for the program to get the BSD estimation.

- Operating conditions: Run number, Sparger number, U_G, Q_L, G/L ratio, ΔP_{Sp}, A_{Th}, C_{SDS},
- Experimentally determined parameters for both the whole column and the sparger region: Mid-height temperature, Mid-height pressure, Static surface tension of the liquid, Dispersion height,
- Time at which the feed to the sparger (gas and liquid) is shut-off and DGD data collection starts, t_0,
- The drag model of single bubbles for estimating bubble sizes,
- The drag model that accounts for the bubble swarming effect.

Therefore, the outputs (including the whole column and the sparger region) estimated from the DGD data analysis program are listed below:

- Average steady-state gas holdups,
- Estimated bubble size distributions,
- The optimal number of bubble size classes,
- Computed parameters from the estimated BSDs,
  - Interfacial areas of contact,
  - Mean bubble diameters (d_{10}, d_{20}, d_{30}, d_{32}, d_{43}),
  - Bubble number density,
- Fit estimated BSDs to standard distributions (e.g., Log-Normal or Rosin-Rammler distributions).

The details of the procedures and mathematical computations for estimating BSDs from the experimentally determined temporal variation of gas holdups are discussed in Sections 5.2.1 to 5.2.9.

5.2.1 Identifying the Initial Time Boundary of the DGD Data and Eliminate Initial Instabilities

As seen in Figure 5.3, the data at the steady-state section is collected from 0 to t_0. At t_0, the feed to the sparger (gas and liquid) is shut-off. Therefore, t_0 corresponds to the initial time boundary of the DGD data.

The average gas holdup obtained at the steady-state section is used as the initial gas holdup for the DGD data analysis. The standard deviation around the steady-state average gas holdup is represented by 95 % of the confidence interval of this gas holdup.

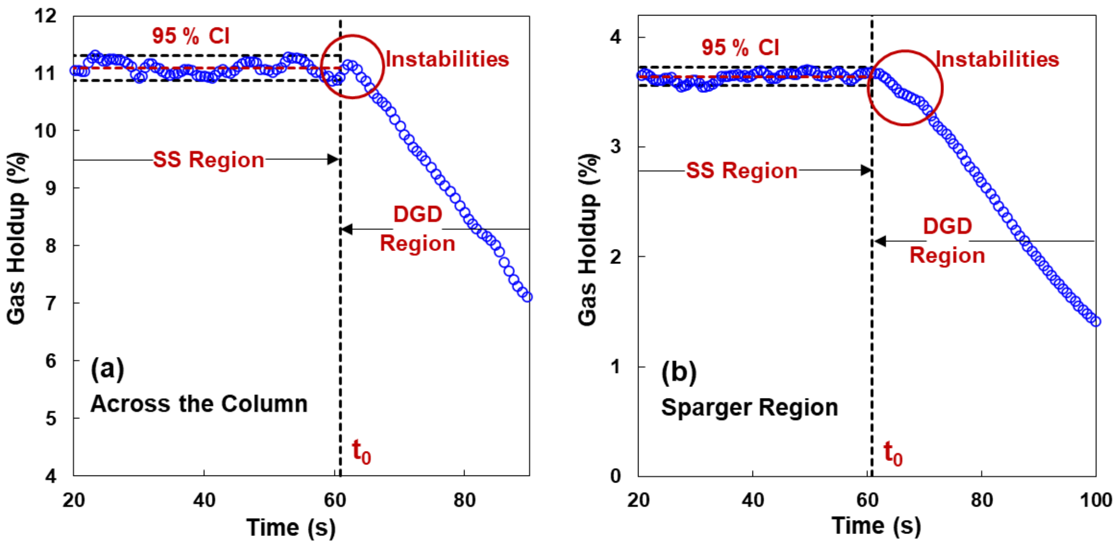

Figure 5.3 Graphical expression of the instabilities after shutting off the feed, experimental conditions: ΔP_{Sp} = 210 kPa, C_{SDS} = 20 ppm, (a) U_G = 10 mm/s, (b) U_G = 1 mm/s.

After identifying the initial time boundary, it is clear that some instabilities occur at the beginning of the DGD process (immediately after t_0). The disengagement trend of these instabilities is different from the trend of the following curve. In some conditions, the gas holdup has a jump first and then decreases, as shown in Figure 5.3a. However, in some other conditions, as seen in Figure 5.4b, instead of having a jump, the gas holdup decreases with a slower disengagement rate compared to that of the following curve. The reasons for these instabilities can be most probably explained by the sudden hydrodynamics change in the column (e.g., the effect of eddies or turbulence near the pressure sensor, a time delay due to the strong liquid downward velocity at the initiation of the DGD process). Therefore, these instabilities are not considered as a part of any disengagement time intervals.

By reviewing a large amount of the experimental runs done in this investigation, the durations of these instabilities are about 3.5 s for the measurements throughout the column and about 2.5 s for the sparger region. Therefore, these instabilities in most runs were eliminated automatically in the advanced DGD data analysis program.

5.2.2 Identifying the Final Time Boundary of the DGD Data

The differential pressure sensors used in the experiments have their measuring limits. The one used for measurements throughout the column ranges from 0 to 34.5 kPa with a measuring error of 0.08 % of the full scale, corresponding to +/- 28 Pa. The other one used in the sparger region measures from 0 to 2.5 kPa. The measuring error is 0.08 % of the full scale as well and, as a result, corresponds to +/- 2 Pa.

It is hard for the differential pressure sensors to give accurate measurements once the measured differential pressures are below 28 Pa in the whole column and below 2 Pa at the sparger region. Therefore, those differential pressure data generated beyond the sensor limit need to be removed. As seen in Figure 5.4a below, the 1st data point below the sensor lower limit (ΔP_{LL}) is identified, which corresponds to t_{LL}, then remove all the data after this time.

In some cases, as seen in Figure 5.4a, after removing the data below ΔP_{LL}, although the data are above the sensor limit, the variances of the data points were found to be within the standard deviation (95 % of CI) around the mean. Thus, these data points were statistically changing as a function of time. The second step is, therefore, to check if the gas holdup is statistically decreasing as a function of time. This can be done by the following steps:

1) The calculations start from the last data point, "N_{DGD}", and are done backwards,
2) Firstly, calculate the average gas holdup and its standard deviation (95 % CI) of Group "n" (from "N_{DGD}" to "N_{DGD} - 30"),
3) Then, calculate the average of gas holdup and its standard deviation (95 % CI) for the Group "n-1" (from "N_{DGD} - 30" to "N_{DGD} - 60"),
4) Compare their average gas holdups and standard deviations,
    - If the average gas holdup of Group "(n-1)" is higher than the upper limit of Group "n" (the upper limit is equal to the average gas holdup plus its standard deviation (95 % CI)), then calculate the intersection of these two groups, which corresponds to t_F. Then, remove all the data after this time. So, t_F is the final time boundary for the DGD data to be analyzed.
    - If not, then repeat the steps from 1 to 4.

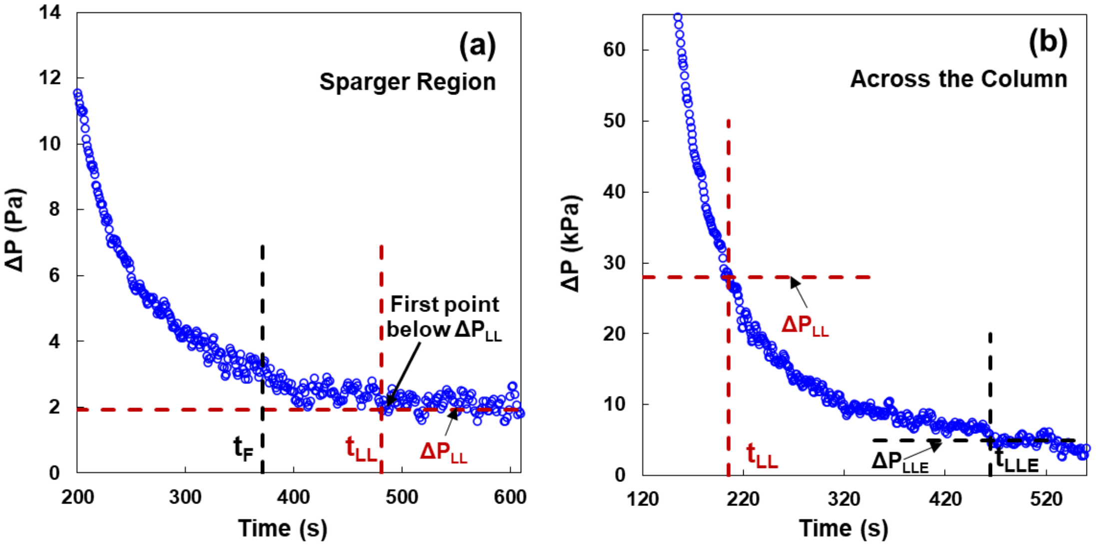

Figure 5.4 Graphical expression of finding the final time boundary for the DGD data to be analysed. Experimental conditions: (a) U_G = 0.5 mm/s, ΔP_{Sp} = 350 kPa, C_{SDS} = 20 ppm, (b) U_G= 1 mm/s, ΔP_{Sp} = 210 kPa, C_{SDS} = 5 ppm).

A logic flow diagram for mathematically determining t_F is shown in Figure 5.5.

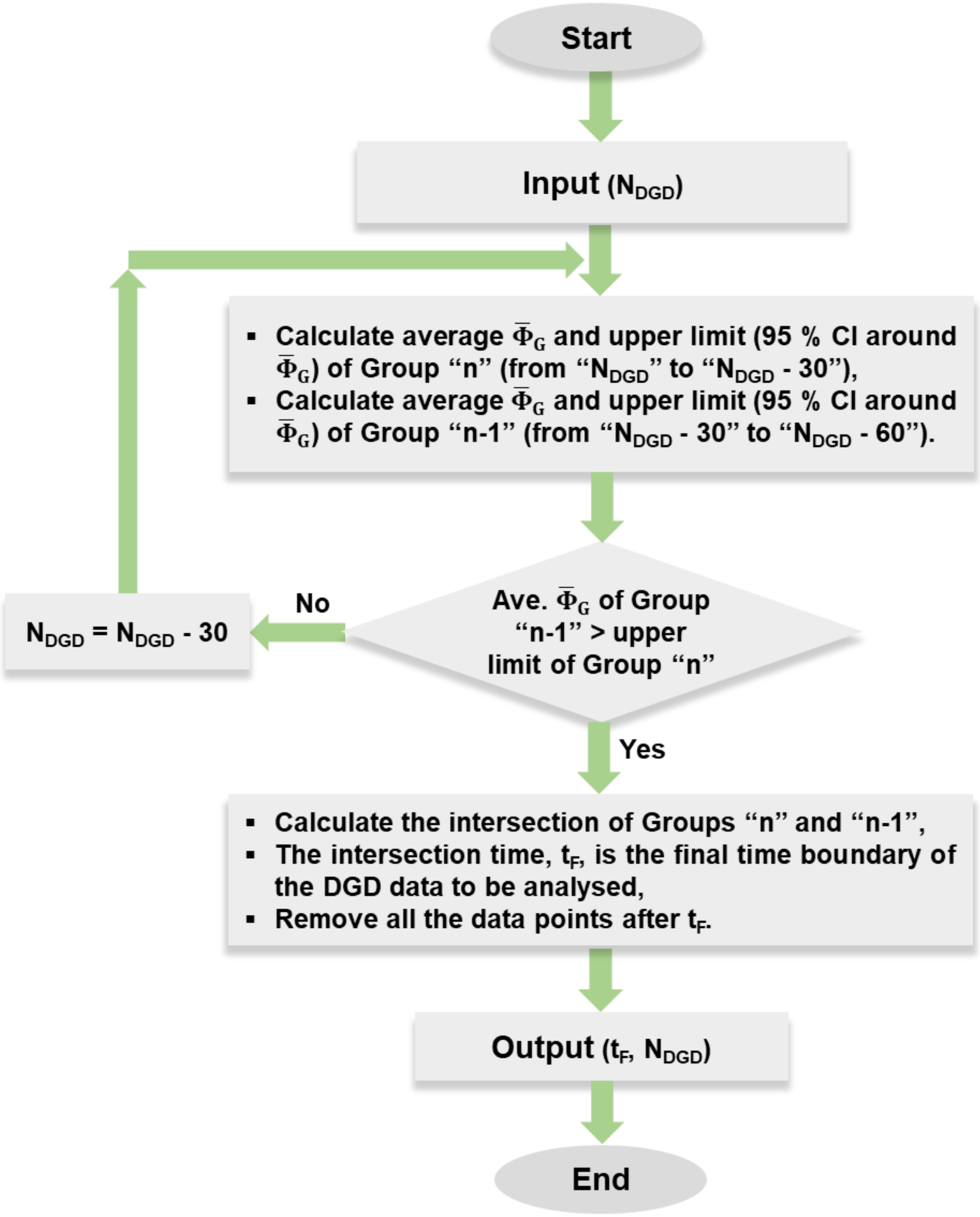

Figure 5.5 Logic flow diagram of identifying the final time boundary of the DGD data to be analyzed.

Besides, there are some cases like Figure 5.4b. The gas holdup continues to decrease with time beyond the manufacture's declared sensor lower limit (ΔP_{LL}). This shows that the real lower limit of this sensor (DP1, 0 – 34.5 kPa) is at a pressure difference value much lower than the manufacture's value. By extensively reviewing the experimental DGD results, it was concluded that the practical lower limit of this sensor is 5 Pa, which is defined as the experimentally estimated lower limit of the differential pressure sensor, shown as ΔP_{LLE} in Figure 5.4b. So, in these cases, t_{LLE} is the final time boundary of the DGD data to be analyzed.

5.2.3 Identifying the Boundaries of the First Disengagement Time Interval

As was shown in Figure 4.12, almost all the DGD results obtained in this investigation show a linear part at the beginning of the DGD process, followed by a concave curve to the end. The curve approaches zero asymptotically at infinite time.

Therefore, the criterion used for determining the final boundary of the first time interval is based on identifying the point at which the linear data-fit line begins to consistently and significantly deviate from the following experimental points.

The procedures for identifying the end boundary of the first disengagement time interval are described below,

1) Start after the instabilities at the onset of the DGD process, make a linear fit to the first disengagement time interval with a limited number of points. Then, progressively adding the points to the linear fit.

    - In order to make the program as automatic as possible, the starting point of the linear fit, $n_{1initial}$, is selected after reviewing most of the DGD results obtained under a wide range of experimental conditions. Thus, this number is 7 (corresponds to 3.5 s) for the runs measured in the whole column, and 5 (corresponds to 2.5 s) for those at sparger region, which automates 95 % of the DGD runs (except for $U_G \leq 1$ mm/s).
    - The number of points initially included in the linear fit, $n_{1linest\_start}$, is 10 based on most of the DGD results in this work,

2) Calculate the gas holdup and its upper limit (gas holdup plus its standard deviation (95 % CI)) of the last point on the linear fit,

3) Compare this point with the following three points. If at least one of the experimentally measured gas holdup of the following three points is less than the upper limit of this point, then add one point to the linear fit and repeat the steps (2) & (3).

When the experimentally measured gas holdups of all the three following points are larger than the upper limit of the last point on the linear fit, theoretically, it means the linear fit line begins to deviate from the following experimental points. However, after reviewing most experimental results, this may happen earlier than the real linear fit deviation due to the experimental error. Thus, it can be considered as pseudo-deviation.

In order to reduce the effect of the experimental error on identifying the final boundary of the first time interval, the linear fit continues adding points when the pseudo-deviation occurs. Once the continuous four points, the experimentally measured gas holdups of their following three points, are all larger than their upper limits of the gas holdups calculated from the linear fit, the final boundary of the first disengagement time interval is identified.

A logic flow diagram showing the steps of identifying the final boundary of the first disengagement time interval is depicted in Figure 5.6. Once the final boundary of the first time interval is identified, as seen in Figure 5.7. The initial boundary (pseudo start point of the DGD region) is identified as the intersection point of the average gas holdup line at the steady-state section and the linear fit line of the first disengagement time interval.

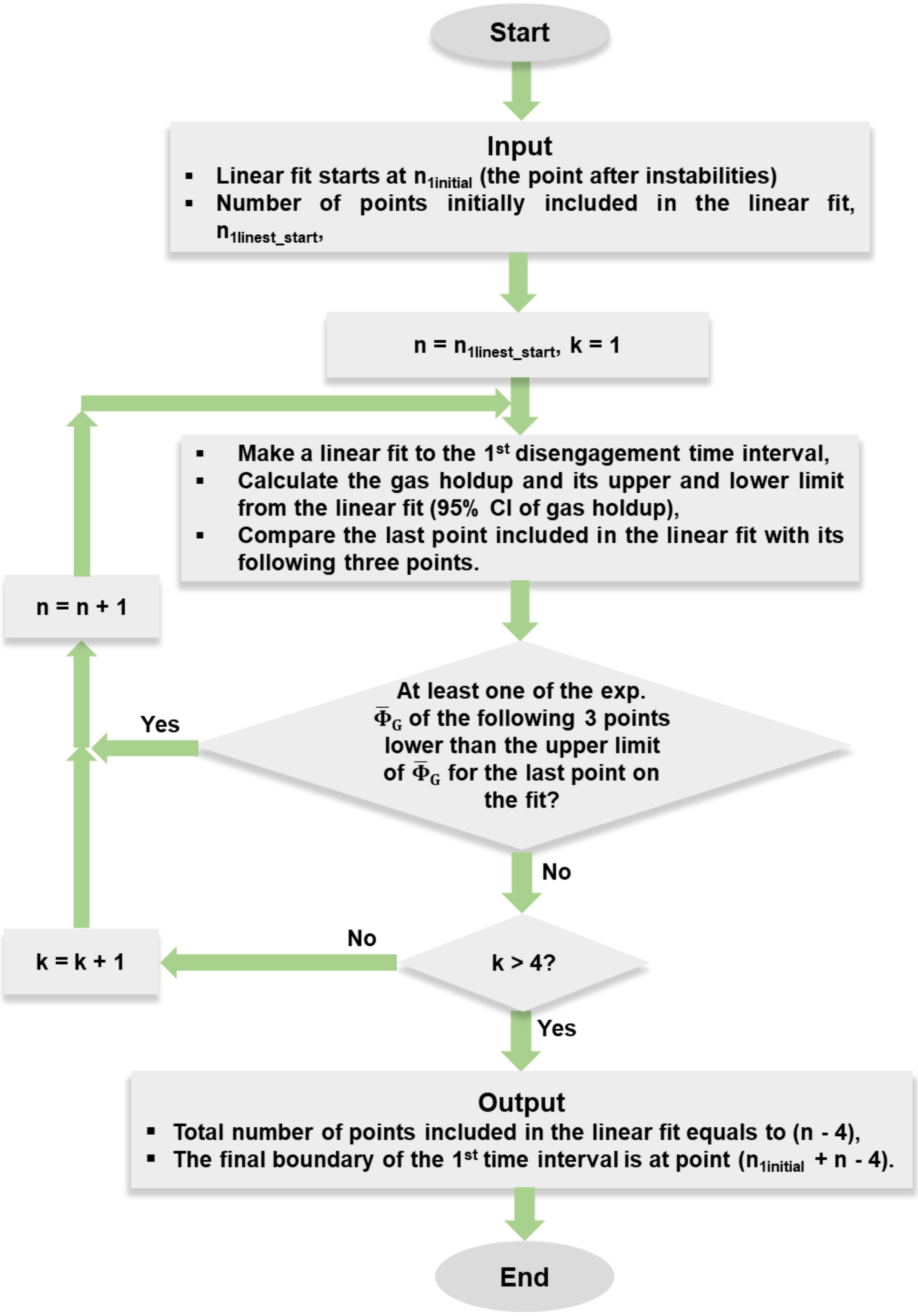

Figure 5.6 Logic flow diagram of identifying the final boundary of the first disengagement time interval.

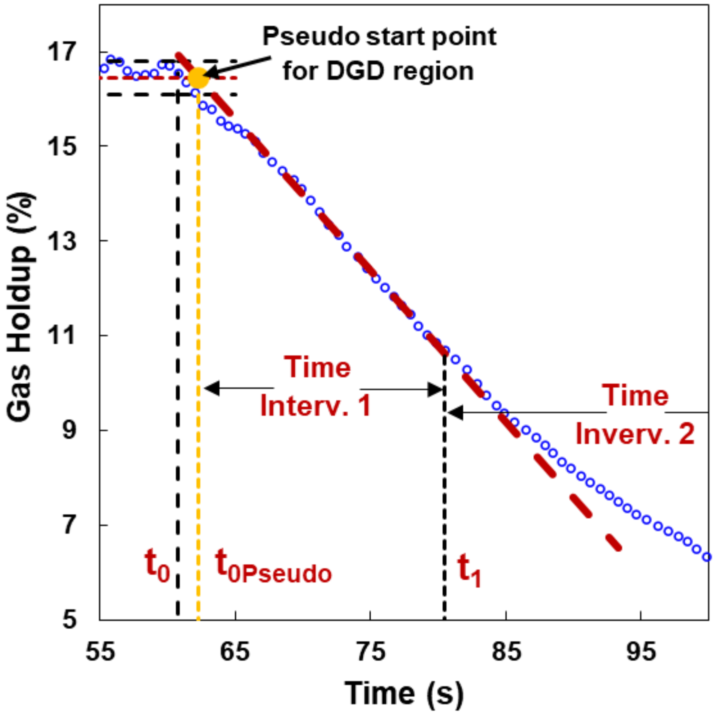

Figure 5.7 Graphical representation of the method used to identify the initial/final boundaries of the first disengagement time interval. (Throughout the column, ΔP_{Sp} = 210 kPa, C_{SDS} = 20 ppm, U_G = 20 mm/s).

5.2.4 Dividing the DGD Data into N Non-Equal Time Intervals

The typical gas disengagement process, which contains infinite bubble size classes, can be generally described by a curve, as was shown in Figure 4.12. It is impractical to determine these infinite sizes of bubbles. A general methodology is instead to estimate a limited number of bubble size classes. This can be done by approximating the disengagement curve with a number of consecutive straight lines, a simplified representation of which is shown in Figure 5.8.

As discussed in Section 5.1, the disengagement rates of varying bubble size classes are different during the DGD event. Large bubbles usually rise faster than small bubbles, and the disengagement time needed for large bubbles is much shorter than that needed for small bubbles. Therefore, after identifying the boundaries of the first disengagement time interval, the rest DGD curve is divided into (N-1) non-equal (logarithmic-equal) time intervals. N varies from 2 to N_{Max}. By following the log-equal time intervals, as seen in Figure 5.8, small bubble disengagement (the end of the curve) is longer than large bubbles (beginning of the curve), which could reasonably express the experimental observation.

At the end of each time interval, the gas holdup values need to be smoothed to avoid wild derivative changes. The smoothing is done by a local quadratic polynomial fit to a specific number of points before and after the raw values in the log-log domain. Due to the non-equal time intervals, the number of points used at the beginning time intervals of the curve is less than that at the end of the curve. In this work, the number of points used for each side of the polynomial fit is equal to three times the time interval number, whenever possible.

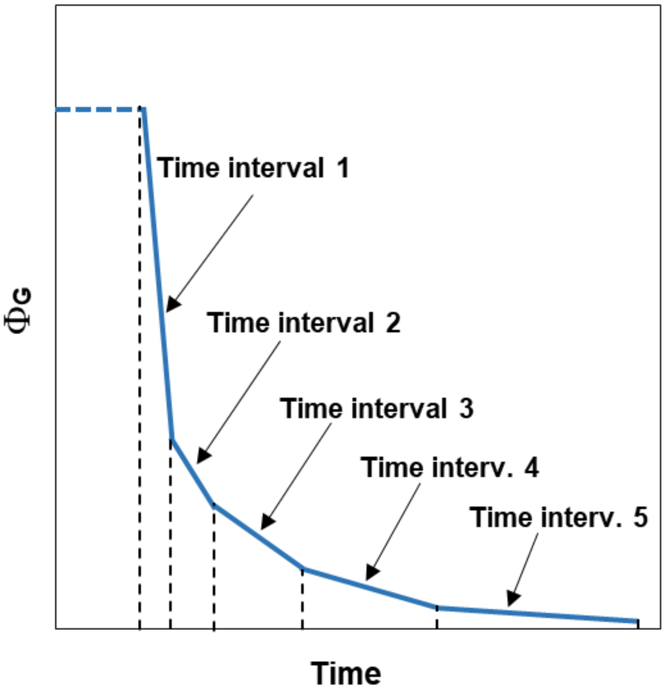

Figure 5.8 Simplified representation of using a number of consecutive straight lines to approximate the DGD curve.

5.2.5 Graphical Representation of the Concepts Involved in the Novel DGD Analysis Method

Before mathematically estimating the bubble sizes and the corresponding gas holdups for each bubble size class, it is necessary to explain the concept of this advanced DGD method. In this investigation, the bubble sizes are estimated using the bubble terminal rise velocities obtained from the measured bubble rise velocities. However, it is easier to explain the concept from a known size of bubbles since their terminal rise velocity is constant.

During the DGD process, for any disengagement time interval, the main size class of bubbles disengages with the smaller bubbles entrained into this interval. For instance, the first disengagement time interval to be disengaged has "N" bubble classes, then the second disengagement time interval has "N-1" bubble classes (without the main bubble size class disengaged in the first disengagement time interval) and so on. The last disengagement time interval has only "1" bubble size class, that of the smallest bubble size class.

In order to clearly explain how the various size classes of bubbles disengage in different time intervals, a total of 5 bubble size classes are used to schematically describe this DGD method. Therefore, in this case, the first disengagement time interval has “5” bubble classes, then the second disengagement time interval has “4” bubble classes, and the last disengagement time interval has only “1” bubble size class.

Figure 5.9a, at a specific time (t = 40 s), depicts the level of each bubble size class that stays in various disengagement time intervals of the column. It is obvious that Class 5, the smallest bubble size class, stays in all disengagement time intervals in the column. Whereas Class 1, the largest bubble size class, stays only in the first disengagement time intervals. As a result, the total gas holdup in the first disengagement time interval is the sum of the gas holdups constituted by 5 bubble size classes, as seen in Figure 5.9b.

For a known size of bubbles, although the terminal rise velocity is constant (see the dotted line in Figure 5.9c), the slip velocities of these bubbles in different disengagement time intervals are affected by the total gas holdups in different intervals. Therefore, as seen in Figure 5.9c, the slip velocities of bubble size class 5 in different time intervals were obtained by taking into consideration of the gas holdups of each interval.

The mathematical calculations, including the gas holdups of each disengagement time interval, the bubble sizes, and corresponding gas holdups of each bubble size class in each interval, will be discussed in Sections 5.2.6 & 5.2.7.

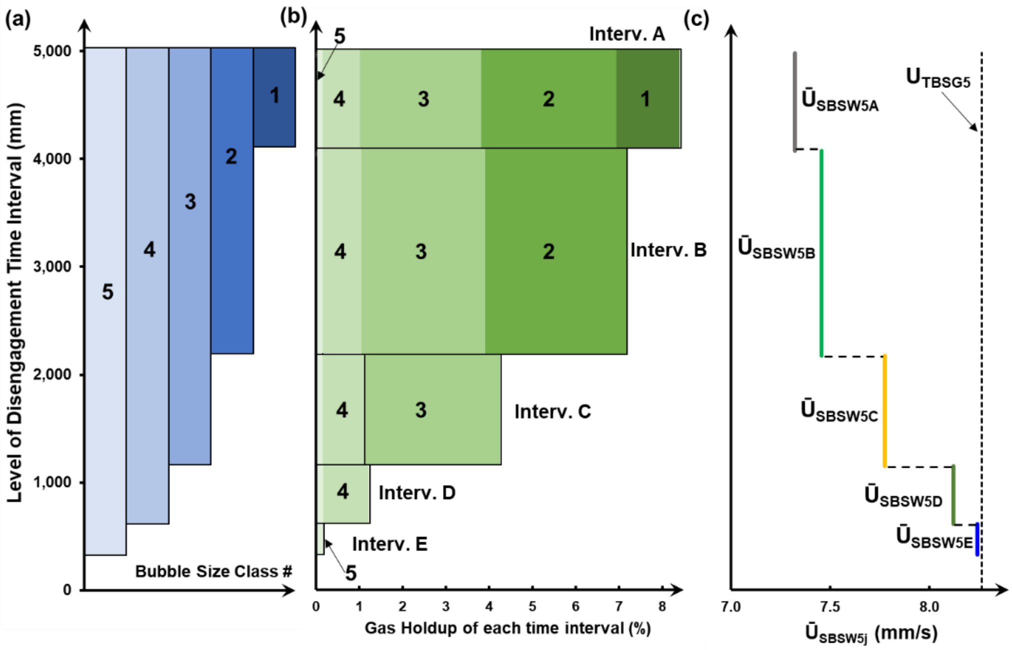

Figure 5.9 Graphical description of DGD data analysis at a specific disengagement time t = 40 s, (a) the level of each bubble size class in different disengagement time intervals in the column; (b) the gas holdups of each disengagement time interval and the gas holdup of each class in each interval; (c) slip velocities of bubble size class 5 in each interval. (Throughout the column, C_{SDS} = 20 ppm, ΔP_{Sp} = 210 kPa, Q_L = 7 L/min, U_G = 5 mm/s).

Since the liquid is moving down to compensate for the volume of the gas disengaged during the DGD process, the effect of liquid downward velocity on bubble rise velocity should be considered. Figure 5.10 illustrates how the bubble rise velocities were obtained from the bubble slip velocities. As seen in Figure 5.10, the rise velocity of bubble size class 5 in each disengagement time interval is equal to its slip velocity minus the liquid velocity in that interval. The mathematical calculation of the liquid velocity in each interval is discussed in Section 5.2.6.1.

Besides, the average rise velocity of size class 5 throughout the column (see in Figure 5.10c) can be obtained by the rise velocities of each time interval as well as the interval volume, which can be calculated by:

$$U_{RBSW5,Avg} = \frac{\sum_{j=A}^{E} U_{RBSW5j} \cdot h_{Dispj}}{\sum_{j=A}^{E} h_{Dispj}} \tag{5.1}$$

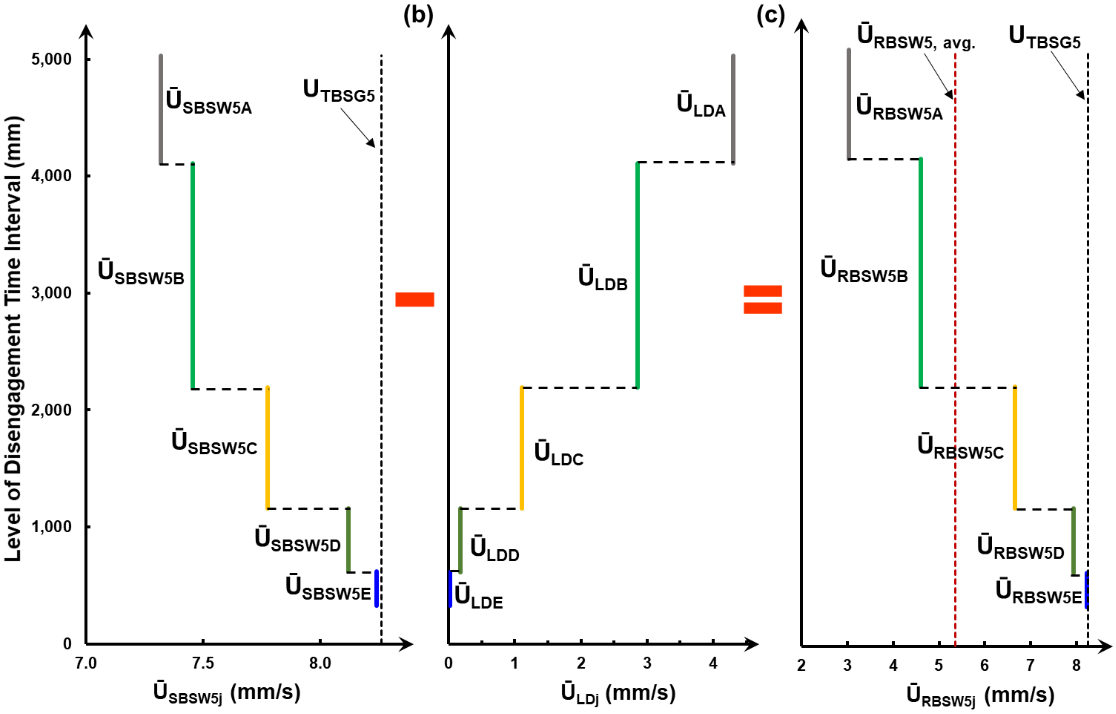

Figure 5.10 Graphical description of DGD data analysis at a specific disengagement time t = 40 s, (a) slip velocities of bubble size class 5 in each time interval; (b) liquid downward velocities in each time interval; (c) the adjusted rise velocities of bubble size class 5 in each time interval. (Throughout the column, C_{SDS} = 20 ppm, ΔP_{Sp} = 210 kPa, Q_L = 7 L/min, U_G = 5 mm/s).

5.2.6 Estimating the Bubble Size for Each Bubble Class

In this section, the method used to estimate the size of bubbles contained within each bubble size class will be discussed. The methodology used is described in the logic flow diagram presented in Figure 5.11.

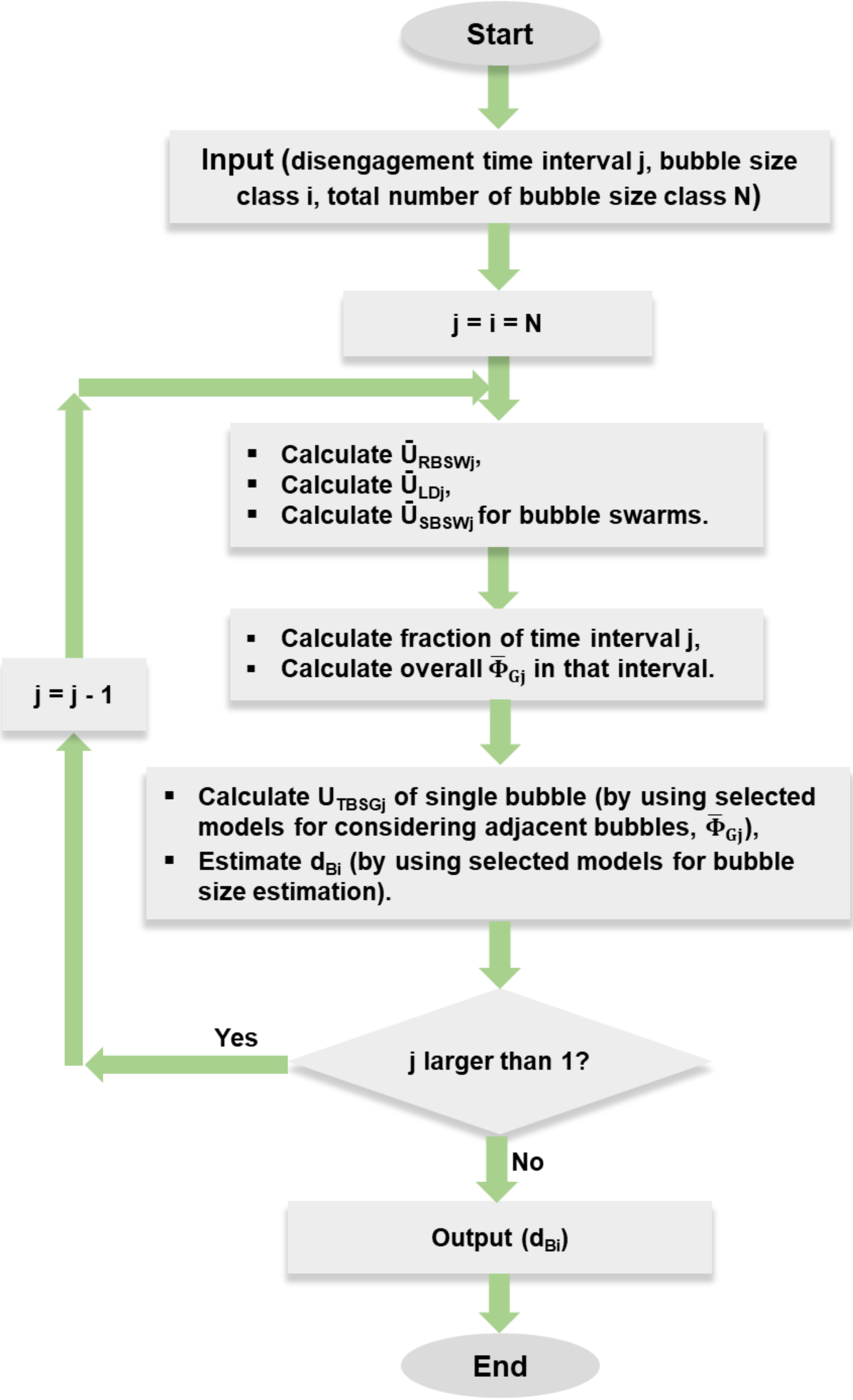

Figure 5.11 Logic flow diagram of the methodology used to estimate the bubble size for each bubble size class.

5.2.6.1 Estimating the Rise and Slip Velocities of Bubble Swarms

During the disengagement, the main size class of bubbles (represented by i) within a disengagement time interval (represented by j) is recorded to be disengaged completely from the two measuring ports of the differential pressure sensor within a period of time. Therefore, the mean rise velocity of this bubble size class, as well as this disengagement time interval, can be expressed by:

$$\overline{\mathrm{U}}_{\mathrm{RBSWj}} = \frac{\mathrm{H}_{\mathrm{Dis}}}{\mathrm{t}_{\mathrm{j}}} \tag{5.2}$$

In the bubble column, as the gas moves up to disengage, the liquid will flow down to compensate for the volume of gas disengaged. Thus, at any cross-section, the volumetric flow of the downward liquid should be equal to that of the upward gas:

$$\dot{\mathrm{V}}_{\mathrm{Gj}} = \overline{\mathrm{U}}_{\mathrm{RBSWj}} \cdot \overline{\Phi}_{\mathrm{Gj}} \cdot \mathrm{A_c} = \overline{\mathrm{U}}_{\mathrm{LDj}} \cdot \left(1 - \overline{\Phi}_{\mathrm{Gj}}\right) \cdot \mathrm{A_c} = \dot{\mathrm{V}}_{\mathrm{Lj}} \tag{5.3}$$

So, the downward liquid velocity of time interval j is:

$$\overline{\mathrm{U}}_{\mathrm{LD_j}} = \frac{\dot{\mathrm{V}}_{\mathrm{Gj}}}{\mathrm{A_c} \cdot \left(1 - \overline{\Phi}_{\mathrm{Gj}}\right)} \tag{5.4}$$

This requires the calculation of the volumetric gas disengagement rate during disengagement time interval “j”. For each time interval, this is computed from the data as:

$$\frac{\dot{\mathrm{V}}_{\mathrm{Gj}}}{\mathrm{A_c}} = -\frac{\partial \overline{\Phi}_{\mathrm{GC}}}{\partial \mathrm{t}} \cdot \mathrm{H}_{\mathrm{Dis}} = \frac{\mathrm{H}_{\mathrm{Dis}}}{\partial \mathrm{t}} \cdot -\partial \overline{\Phi}_{\mathrm{GC}} \approx -\frac{(\overline{\Phi}_{\mathrm{GC}})_{\mathrm{j}} - (\overline{\Phi}_{\mathrm{GC}})_{\mathrm{j-1}}}{\mathrm{t_j} - \mathrm{t_{j-1}}} \cdot \mathrm{H}_{\mathrm{Dis}} \tag{5.5}$$

The slip velocity of bubble swarms needs then to be calculated to eliminate the effect of downward liquid velocity,

$$\overline{\mathrm{U}}_{\mathrm{SBSWj}} = \overline{\mathrm{U}}_{\mathrm{RBSWj}} + \overline{\mathrm{U}}_{\mathrm{LDj}} \tag{5.6}$$

5.2.6.2 Estimating Gas Holdups for Each Disengagement Time Interval

Very fine bubbles have very small rise velocities; hence they stay in the column for a very long time. Thus, there might be residual gas holdups in the column as the DGD stops. This residual gas holdup needs to be deducted from the total gas holdup used for the data analysis. In this way, only the gas holdup generated by the completely disengaged bubbles will be considered in the calculations.

The gas holdup of a disengagement time interval is obtained by the mean bubble size class (the largest bubble size class in that time interval) and the other bubble classes with smaller bubble sizes. Therefore, the gas holdup of a disengagement time interval can be described as:

$$\overline{\Phi}_{\mathrm{Gj}} = \overline{\Phi}_{\mathrm{Gjj}} + \overline{\Phi}_{\mathrm{G(j+1)j}} + \cdots = \sum_{\mathrm{i=j}}^{\mathrm{N}} \left(\overline{\Phi}_{\mathrm{Gij}}\right) \tag{5.7}$$

The gas holdup of each time interval, $\overline{\Phi}_{\mathrm{Gj}}$, is the sum of the individual gas holdups, $\overline{\Phi}_{\mathrm{Gij}}$, of each bubble class present in that interval. The gas holdup of each bubble class in each time interval will be estimated in Section 5.2.7.

At t_0, the gas holdup at any cross-section of the column is uniformly distributed. As the bubbles disengage from the first time interval, it will also have bubbles leave the first time interval to the other time interval.

For simple simulation, it is assumed that the gas holdup distribution of the first disengagement time interval is the same as that during the steady-state operation of the column. Other than the first time interval, the gas holdup of each time interval will be mainly estimated by computing the fraction of each disengagement time interval corresponding to the whole DGD region.

The fraction of each time interval is calculated at the time when the previous time interval has just finished disengaging (*i.e.,* $\mathrm{t} = \mathrm{t_{j-1}}$, the time interval $(\mathrm{j} - 1)$ just finished disengaging). The fraction of time interval j corresponding to the entire DGD region can be described by:

$$\mathrm{X_j} = 1 - \frac{\overline{\mathrm{U}}_{\mathrm{RBSWj}}}{\mathrm{H_{Dis}}} \cdot \mathrm{t_{j-1}} \tag{5.8}$$

The fractions of the other time intervals which have not yet been disengaged are described as:

$$X_{j+1,t_{j-1}} = \frac{(\overline{U}_{RBSWj} - \overline{U}_{RBSWj+1})}{H_{Dis}} \cdot t_{j-1} \tag{5.9}$$

$$X_{j+2,t_{j-1}} = \frac{(\overline{U}_{RBSWj+1} - \overline{U}_{RBSWj+2})}{H_{Dis}} \cdot t_{j-1} \tag{5.10}$$

...

$$X_{j+n,t_{j-1}} = \frac{(\overline{U}_{RBSWj+(n-1)} - \overline{U}_{RBSWj+n})}{H_{Dis}} \cdot t_{j-1} \tag{5.11}$$

At any given time, the gas holdup measured for the entire DGD region is

$$\overline{\Phi}_{GC,t} = \sum_{j}^{N} (\overline{\Phi}_{Gj} \cdot X_{j,t}) \tag{5.12}$$

Therefore, at the times of each time interval boundary, it is possible to compute the gas holdup of each interval at any given time, starting with the last disengagement time interval, since there is only one bubble size class in the last interval. Thus, the gas holdup of the last time interval can be known from:

$$\overline{\Phi}_{GN} = \frac{\overline{\Phi}_{GC,t_{N-1}}}{X_{N,t_{N-1}}} \tag{5.13}$$

The calculation then proceeds to $\overline{\Phi}_{G(N-1)}$, $\overline{\Phi}_{G(N-2)}$, $\overline{\Phi}_{G(N-3)}$ etc. until $\overline{\Phi}_{G2}$, using the values of $\overline{\Phi}_{Gj}$ estimated previously:

$$\overline{\Phi}_{GC,t_{j-1}} = \overline{\Phi}_{Gj} \cdot X_{j,t_{j-1}} + \sum_{k=j+1}^{N} (\overline{\Phi}_{Gk} \cdot X_{k,t_{k-1}}) \tag{5.14}$$

$$\overline{\Phi}_{Gj} = \frac{\overline{\Phi}_{GC,t_{j-1}} - \sum_{k=j+1}^{N} (\overline{\Phi}_{Gk} \cdot X_{k,t_{k-1}})}{X_{j,t_{j-1}}} \tag{5.15}$$

By using this ‘reverse cascade’ calculation, once the gas holdup for a time interval “j” has been computed, the gas holdup of “j-1” can be found. Therefore, the gas holdup for each disengagement time interval can be estimated.

5.2.6.3 Estimating Bubble Diameters for Each Bubble Size Class

The slip velocities discussed in Section 5.2.6.1 are the bubble swarm velocities. As discussed in Section 3.5, the effect of bubble swarms on bubble slip velocities can be eliminated by using the drag model accounting for the crowding effect.

Therefore, the terminal velocity of a single bubble for size class “i” can be obtained by using a correction factor provided by any of the models selected,

$$\mathrm{U_{TBSGi}} = \lambda_j \cdot \overline{\mathrm{U}}_{\mathrm{SBSWi}} \tag{5.16}$$

The correction factor is a function of the gas holdup, which can be written as

$$\lambda_j = f(\overline{\Phi}_{Gj}) \tag{5.17}$$

After the terminal velocities of single bubbles are obtained, the bubble diameter can be estimated using the various correlations of the drag coefficient on bubble terminal velocity.

A subroutine is built in the Excel VBA to estimate the bubble size from the bubble terminal velocity. The procedures are shown by a logic flow diagram in Figure 5.12.

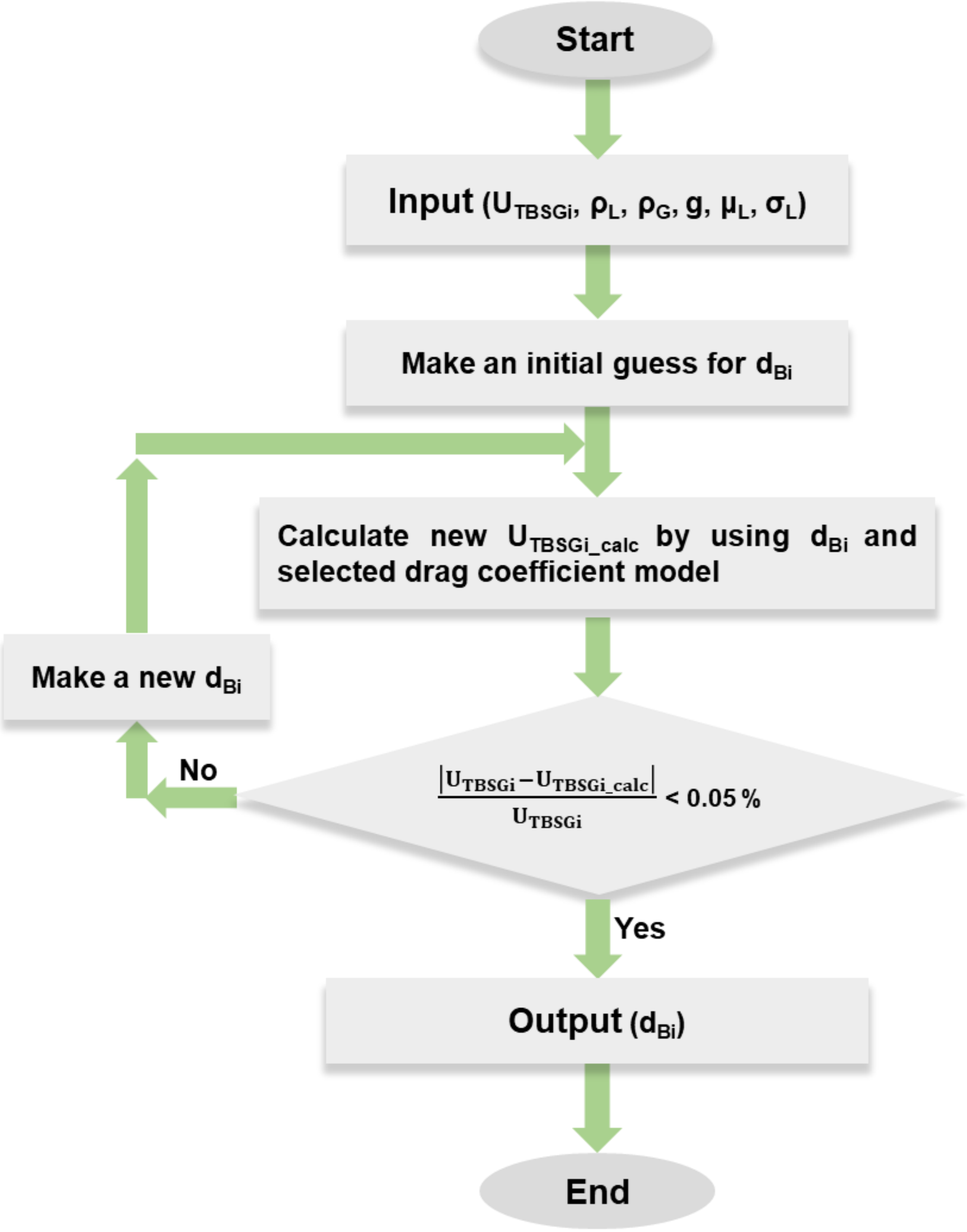

Figure 5.12 Logic flow diagram of estimating bubble size using the selected drag models of the single bubble

5.2.7 Estimating Gas Holdups for Each Bubble Size Class

The process for estimating gas holdups for each bubble size class is not as straightforward as that for estimating bubble diameters because different bubble size classes with different proportions are present throughout the disengagement time intervals as they rise and disengage.

The basic criteria are derived from the population balance of each class of bubbles across the layered time intervals [Luo et al., 1996]. During the gas disengagement, all the classes of bubbles that are smaller than the largest, i.e., from (j+1) to N, rise more slowly than size class "j". Therefore, all those classes will be losing some bubbles from interval "j" to interval "j+1". On the other hand, time interval j will receive bubbles from time interval "j-1". The gas holdup of each bubble class in each disengagement time interval stays constant. However, the total amount of bubbles (total volume) of a time interval increases because the lower boundary velocity (the main bubble rise velocity of interval "j+1") is slower than the upper boundary (the main bubble rise velocity of interval "j"). Thus, when the interval "j" just finished disengaging, interval "j+1" reaches its largest fraction corresponding to the entire DGD region.

The increase of the total amount of class of bubbles "i" in disengagement time interval "j" (left side of the equation) is given by the difference (right side of the equality) between the bubbles received from the layer above and those lost to the layer below.

$$\left(\overline{\mathrm{U}}_{\mathrm{RBSW(j-1)}} - \overline{\mathrm{U}}_{\mathrm{RBSWj}}\right)\cdot\overline{\Phi}_{\mathrm{Gij}} = \left(\overline{\mathrm{U}}_{\mathrm{RBSW(j-1)}} - \overline{\mathrm{U}}_{\mathrm{RBSWi(j-1)}}\right)\cdot\overline{\Phi}_{\mathrm{Gi(j-1)}} - \left(\overline{\mathrm{U}}_{\mathrm{RBSWj}} - \overline{\mathrm{U}}_{\mathrm{RBSWij}}\right)\cdot\overline{\Phi}_{\mathrm{Gij}} \tag{5.18}$$

By rearranging the above equation,

$$\left(\overline{\mathrm{U}}_{\mathrm{RBSW(j-1)}} - \overline{\mathrm{U}}_{\mathrm{RBSWi(j-1)}}\right)\cdot\overline{\Phi}_{\mathrm{Gi(j-1)}} = \left(\overline{\mathrm{U}}_{\mathrm{RBSW(j-1)}} - \overline{\mathrm{U}}_{\mathrm{RBSWj}}\right)\cdot\overline{\Phi}_{\mathrm{Gij}} + \left(\overline{\mathrm{U}}_{\mathrm{RBSWj}} - \overline{\mathrm{U}}_{\mathrm{RBSWij}}\right)\cdot\overline{\Phi}_{\mathrm{Gij}} \tag{5.19}$$

The gas holdup of a bubble class can be computed from that of the time interval below it,

$$\overline{\Phi}_{\mathrm{Gi(j-1)}} = \overline{\Phi}_{\mathrm{Gij}}\cdot\frac{\left(\overline{\mathrm{U}}_{\mathrm{RBSW(j-1)}} - \overline{\mathrm{U}}_{\mathrm{RBSWij}}\right)}{\left(\overline{\mathrm{U}}_{\mathrm{RBSW(j-1)}} - \overline{\mathrm{U}}_{\mathrm{RBSWi(j-1)}}\right)} \tag{5.20}$$

The rise velocities are then computed for each class in each time interval by

$$\overline{\mathrm{U}}_{\mathrm{RBSWij}} = \overline{\mathrm{U}}_{\mathrm{TBSGi}}\cdot\lambda_{\mathrm{j}} - \overline{\mathrm{U}}_{\mathrm{LDj}} \tag{5.21}$$

The gas holdup of a disengagement time interval “j” can be described as:

$$\overline{\Phi}_{\mathrm{Gj}} = \overline{\Phi}_{\mathrm{Gjj}} + \overline{\Phi}_{\mathrm{G(j+1)j}} + \cdots = \sum\nolimits_{\mathrm{i=j}}^{\mathrm{N}}\left(\overline{\Phi}_{\mathrm{Gij}}\right) \tag{5.22}$$

The gas holdup for the last class, “N”, corresponds to the time interval that has only one bubble size class (smallest bubbles). The gas holdup is thus described as

$$\overline{\Phi}_{\mathrm{GNN}} = \overline{\Phi}_{\mathrm{GN}} \tag{5.23}$$

Therefore, starting with the time interval “N”, the last interval, it is then possible to compute the partial gas holdups of a bubble size class in all preceding time intervals. The other bubble size classes, including the first bubble size, $\overline{\Phi}_{G11}$, can be calculated by

$$\overline{\Phi}_{Gjj} = \overline{\Phi}_{Gj} - \sum_{i=j+1}^{N}\left(\overline{\Phi}_{Gij}\right) \tag{5.24}$$

By this method, it is possible to compute all the gas holdups of each class in each time interval up to the second disengagement time interval. The balance of the gas holdups of different bubble size classes in the first time interval, $\overline{\Phi}_{Gi1}$; however, it is different because there is no disengagement time interval above it.

Hence, the compositions of the first interval, $\overline{\Phi}_{Gi1}$, are obtained from the volume balance of each bubble class in this interval and the entire DGD region,

$$\overline{U}_{RBSWi1} \cdot \overline{\Phi}_{Gi1} \cdot t_1 \cdot A_C = \left(\overline{\Phi}_{GCi} - \sum_{j=2}^{i}\left(\overline{\Phi}_{GCij}\right)\right) \cdot A_C \cdot H_{Dis} \tag{5.25}$$

Since the gas holdup distributions of each bubble size class in the first time interval are assumed to be the same as those at the steady-state section,

$$\overline{\Phi}_{GCi} = \overline{\Phi}_{Gi1} \tag{5.26}$$

Therefore, Equation (5.25) can be rewritten as

$$\overline{U}_{RBSWi1} \cdot \overline{\Phi}_{Gi1} \cdot \frac{t_1}{H_{Dis}} = \overline{\Phi}_{GCi} - \sum_{j=2}^{i}\left(\overline{\Phi}_{GCij}\right) \tag{5.27}$$

$$\overline{\Phi}_{Gi1} \cdot \frac{\overline{U}_{RBSWi1}}{\overline{U}_{RBSW1}} = \overline{\Phi}_{Gi1} - \sum_{j=2}^{i}\left(\overline{\Phi}_{GCij}\right) \tag{5.28}$$

Replacing and rearranging the balance, $\overline{\Phi}_{Gi1}$ (i = N to 2) can be obtained by

$$\overline{\Phi}_{Gi1} = \frac{\sum_{j=2}^{\boldsymbol{i}}\left(\overline{\Phi}_{GCij}\right)}{1 - \frac{\overline{U}_{RBSWi1}}{\overline{U}_{RBSW1}}} = \frac{\overline{U}_{RBSW1} \cdot \left[\sum_{j=2}^{\boldsymbol{i}}\left(\overline{\Phi}_{GCij}\right)\right]}{\overline{U}_{RBSW1} - \overline{U}_{RBSWi1}} \tag{5.29}$$

As mentioned above, the gas holdup distributions of each class keep the same as those under steady-state operation. Therefore, the gas holdup in the first time interval can be used to represent the gas holdups in the entire DGD region. The overall gas holdup in the entire DGD region for each class in each time interval can be described by

$$\overline{\Phi}_{\mathrm{GCij}} = \overline{\Phi}_{\mathrm{Gij}} \cdot \mathrm{X}_{\mathrm{j},\mathrm{t}_1} \tag{5.30}$$

The fraction of each time interval corresponding to the entire DGD region at the point of t1 is obtained by

$$\mathrm{X}_{\mathrm{j},\mathrm{t}_1} = \frac{\overline{\mathrm{U}}_{\mathrm{RBSW(j-1)}} - \overline{\mathrm{U}}_{\mathrm{RBSWj}}}{\mathrm{H}_{\mathrm{Dis}}} \cdot \mathrm{t}_1 = \frac{\overline{\mathrm{U}}_{\mathrm{RBSW(j-1)}} - \overline{\mathrm{U}}_{\mathrm{RBSWj}}}{\overline{\mathrm{U}}_{\mathrm{RBSW1}}} \tag{5.31}$$

Based on the Equations (5.30) and (5.31) above, the initial gas holdup (gas holdup in the first time interval) for bubble size classes i = N to 2 are computed using

$$\overline{\Phi}_{\mathrm{Gi1}} = \frac{\sum_{\mathrm{j=2}}^{\mathbf{i}}\left[\overline{\Phi}_{\mathrm{Gij}} \cdot \left(\overline{\mathrm{U}}_{\mathrm{RBSW(j-1)}} - \overline{\mathrm{U}}_{\mathrm{RBSWj}}\right)\right]}{\overline{\mathrm{U}}_{\mathrm{RBSW1}} - \overline{\mathrm{U}}_{\mathrm{RBSWi1}}} \tag{5.32}$$

Thus, the gas holdup for the first bubble size class (which has the largest bubble size) is calculated by

$$\overline{\Phi}_{\mathrm{G11}} = \overline{\Phi}_{\mathrm{G1}} - \sum_{\mathrm{i=2}}^{\mathrm{N}}\left(\overline{\Phi}_{\mathrm{Gi1}}\right) \tag{5.33}$$

Therefore, the total gas holdup of each bubble size in all time intervals can be obtained by

$$\overline{\Phi}_{\mathrm{Gi}} = \overline{\Phi}_{\mathrm{Gi1}} + \overline{\Phi}_{\mathrm{Gi2}} + \cdots = \sum_{\mathrm{j=1}}^{\mathrm{i}}\left(\overline{\Phi}_{\mathrm{Gij}}\right) \tag{5.34}$$

The procedures of estimating gas holdups of each bubble size class in each disengagement time interval are shown in Figure 5.13. Therefore, the estimated BSDs can be obtained from the bubble size and its corresponding gas holdup of each bubble size class.

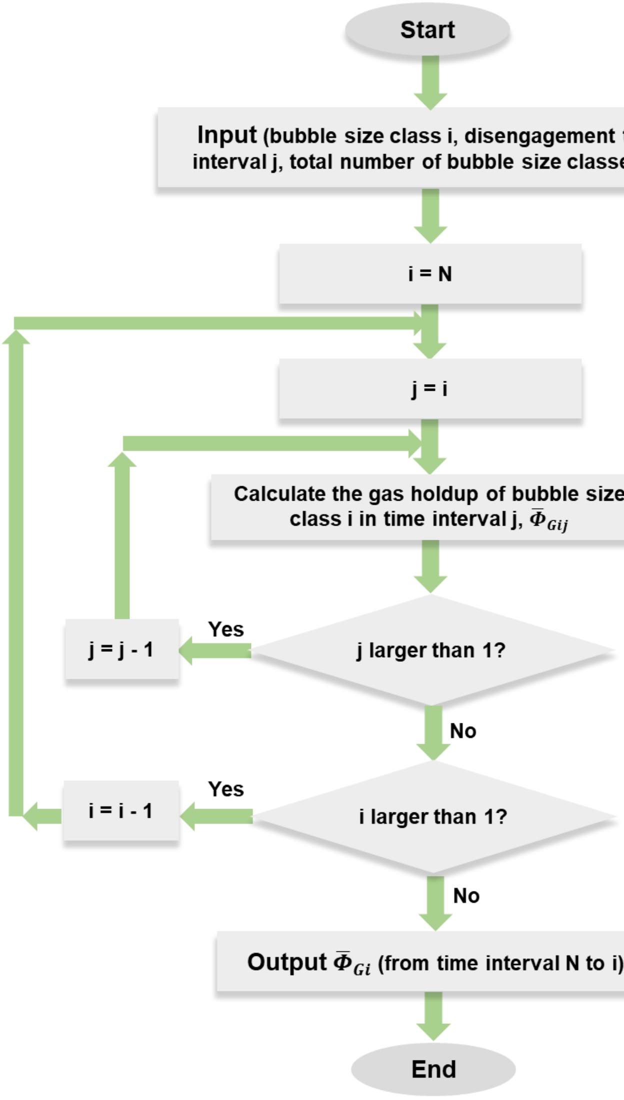

Figure 5.13 Logic flow diagram of computing gas holdups for each bubble size class in each time interval.

5.2.8 Parameters Computed from the Estimated Bubble Size Distributions

In this investigation, several parameters can be computed from the estimated BSDs obtained using the newly developed advanced DGD method, such as interfacial areas, bubble number density, and various mean bubble diameters (d_{10}, d_{20}, d_{30}, d_{32}, d_{43}).

Interfacial areas of contact, which is an important parameter for assessing the gas-liquid dispersions, can be computed by the bubble size and corresponding gas holdup of each bubble size class, described by

$$a = \sum_{i=1}^{N} \left(\frac{6\bar{\Phi}_{Gi}}{d_{Bi}} \right) \tag{5.35}$$

Since this investigation mainly focuses on small bubbles, most of the bubbles generated can be assumed as spheres. Thus, the number of bubbles per unit volume can be calculated from the balance of total bubble volumes,

$$\bar{\Phi}_{Gi} \cdot A_C \cdot H_{Dis} = N_{B_i} \cdot \frac{\pi {d_{Bi}}^3}{6} \cdot A_C \cdot H_{Dis} \tag{5.36}$$

$$N_B = \sum_{i=1}^{N} \frac{6\bar{\Phi}_{Gi}}{\pi {d_{Bi}}^3} \tag{5.37}$$

In addition, the various mean bubble diameters can be obtained from the bubble diameter and the gas holdup of each bubble size class. The physical meaning of these mean bubble diameters will be discussed in Section 6.4.1.

$$d_{10} = \frac{\sum_{i=1}^{N} N_{Bi} \cdot d_{Bi}}{N_B} = \frac{\sum_{i=1}^{N} (\frac{\bar{\Phi}_{Gi}}{{d_{Bi}}^2})}{\sum_{i=1}^{N} (\frac{\bar{\Phi}_{Gi}}{{d_{Bi}}^3})} \tag{5.38}$$

$$d_{20} = \frac{\sum_{i=1}^{N} N_{Bi} \cdot {d_{Bi}}^2}{N_B} = \left(\frac{\sum_{i=1}^{N} (\frac{\bar{\Phi}_{Gi}}{d_{Bi}})}{\sum_{i=1}^{N} (\frac{\bar{\Phi}_{Gi}}{{d_{Bi}}^3})}\right)^{1/2} \tag{5.39}$$

$$d_{30} = \frac{\sum_{i=1}^{N} N_{Bi} \cdot {d_{Bi}}^3}{N_B} = \left(\frac{\bar{\Phi}_G}{\sum_{i=1}^{N} (\frac{\bar{\Phi}_{Gi}}{{d_{Bi}}^3})}\right)^{1/3} \tag{5.40}$$

$$d_{32} = \frac{\sum_{i=1}^{N} N_{Bi} \cdot {d_{Bi}}^3}{\sum_{i=1}^{N} N_{Bi} \cdot {d_{Bi}}^2} = \frac{\overline{\Phi}_G}{\sum_{i=1}^{N} (\frac{\overline{\Phi}_{Gi}}{d_{Bi}})} \tag{5.41}$$

$$d_{43} = \frac{\sum_{i=1}^{N} N_{Bi} \cdot {d_{Bi}}^4}{\sum_{i=1}^{N} N_{Bi} \cdot {d_{Bi}}^3} = \frac{\sum_{i=1}^{N} (\overline{\Phi}_{Gi} \cdot d_{Bi})}{\overline{\Phi}_G} \tag{5.42}$$

5.2.9 Identifying the Optimal Number of Bubble Size Classes

In a continuous BSD, the smallest bubble class starts from a zero volume fraction and ends with a zero volume fraction at the large bubble side. However, the BSD estimated by following the procedures outlined in Sections 5.2.1 to 5.2.8 is truncated. In order to more accurately describe the BSD and improve the ability to fit it with standard distributions, such as Log-normal or Rosin-Rammler distributions, the following two extra points were included in each estimated BSD in order to approach a more realistic description of the BSD:

- The bubble size class smaller than the smallest measured one was assigned a zero volume fraction,
- Similarly, the bubble size class larger than the biggest measured one was assigned a zero volume fraction,

Because of the significant improvement achieved by incorporating such a modification, and its ability to closely resemble real BSDs, the procedure was incorporated in the EXCEL software used in the present investigation.

The conditions encountered in the whole column are used as an example to identify the optimal number of bubble size classes. Figure 5.14a clearly shows that a better BSD resolution can be achieved by increasing the value of N. Since Sauter mean bubble diameter (d_{32}) and bubble number density (N_B) are commonly used as important characteristics in operations such as mass transfer operations and flotation columns, respectively, their trends on increasing N are investigated in Figure 5.14 b&c. As shown in Figure 5.14b, the value of d_{32} was found to increase with increasing N but tends to plateau at relatively high N values. This trend can be attributed to the decreased volume fraction of the smaller bubbles resulting from increasing N. The total bubble number density, which is more sensitive to the smaller bubbles, was decreased due to the reduced volume fraction of smaller bubbles. As seen in Figure 5.14c, the N_B values, opposite to the trend of d_{32}, decreased as N increased. However, it tends to plateau as well when the N value is relatively high.

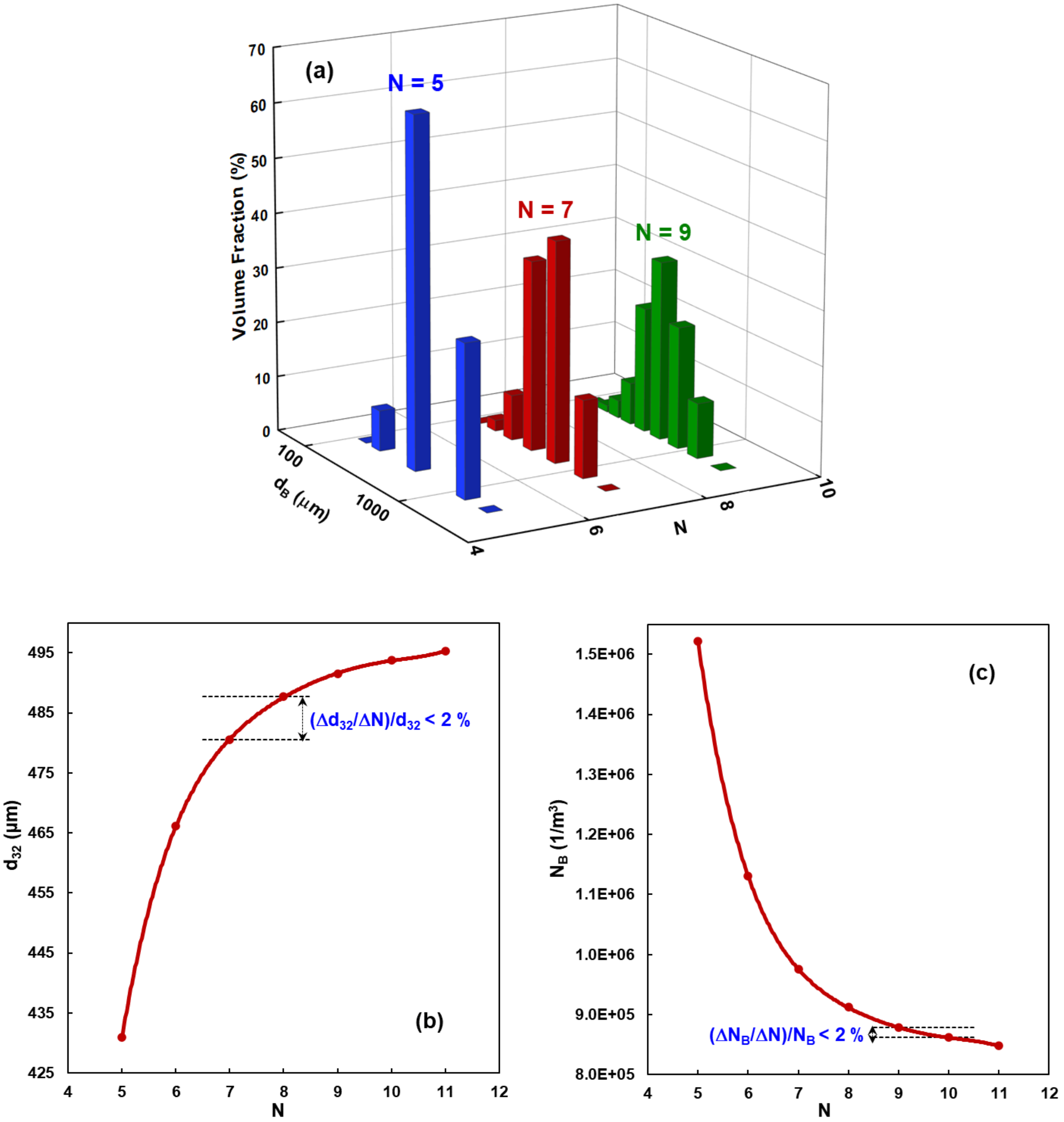

Figure 5.14 Effect of increasing the number of classes used in data analysis on (a) the BSD resolution, (b) the estimated d_{32} value, (c) the estimated N_B value (Throughout the column, C_{SDS} = 10 ppm, ΔP_{Sp} = 210 kPa, Q_L = 7 L/min, U_G = 2 mm/s, Models used: Tomiyama et al. [1998]-fully contaminated and Griffith & Wallis [1961])

In order to accurately analyze the BSD data estimated at various N values using this novel technique, it is necessary to use advanced statistical analysis methods (such as "OriginPro - Data Analysis and Graphing Software" used by SOPAT, or Excel SPC) in order to accurately identify the various characteristics associated with the estimated BSD. However, this is beyond the scope of the present investigation. Therefore, a simple, iterative approach was developed and used to identify the optimal number of classes based on the most relevant parameter that is relevant to the case being studied.

In the case of mass transfer operations (where the d_{32} values are important), the sensitivity of the Sauter mean diameter, d_{32}, to variation in the number of classes $[(\Delta d_{32}/\Delta N)/\ d_{32}]$ was used to identify the optimum number, with an arbitrary threshold limit of 2% being used in the present investigation. On the other hand, the bubble number density N_B plays an important role in flotation operations. Consequently, a slope value of $[(\Delta N_B/\Delta N)/\ N_B = 2\%]$ was used as the threshold limit for assessing the BSD used for flotation purposes. As shown from the results presented in Figure 5.14, optimal N values of 7 and 9 were achieved using Sauter mean diameter and bubble number density criterion, respectively. Similar trends were observed with all other runs. However, the optimal N value was found to vary between 5 and 11 classes depending on the hydrodynamic and interfacial conditions prevailing in the measurement region. For example, a simple, iterative approach was developed and used to identify the optimal number of classes based on the most relevant parameter that is relevant to the case being studied. In the case of mass transfer operations (where the d_{32} values are important), the sensitivity of the Sauter mean diameter, d_{32}, to variation in the number of classes $[(\Delta d_{32}/\Delta N)/\ d_{32}]$ was used to identify the optimum number, with an arbitrary threshold limit of 2% being used in the present investigation. On the other hand, the bubble number density N_B plays an important role in flotation operations. Consequently, a slope value of $[(\Delta N_B/\Delta N)/\ N_B = 2\%]$ was used as the threshold limit for assessing the BSD used for flotation purposes. The results presented in Figure 5.14 showed that optimal N values of 7 and 9 were achieved using Sauter mean diameter and bubble number density criterion, respectively. Similar trends were observed with all other runs. However, the optimal N value was found to vary between 5 and 11 classes depending on the hydrodynamic and interfacial conditions prevailing in the measurement region.

CHAPTER 6 RESULT AND DISCUSSION

In recent years, the use of fine and ultrafine bubbles gained much attention for intensifying mass transfer and flotation operations. Unfortunately, there are presently no non-disputable techniques that can confidently be used for estimating BSDs encountered in these areas. Strictly speaking, to achieve a high degree of confidence in BSD estimation, it is necessary to compare the BSD results estimated by any of the techniques with those obtained using another independent measuring technique such as the Sopat-VI Sc probe used by Ohde et al. [2021]. However, the estimated cost of the measuring system and associated software exceeds $C 200,000, and this technique still relies on some simplifying image analysis assumptions.

In this investigation, a simple and cost-effective method for analyzing DGD data was developed based on the well-known DGD technique. Although this method is restricted by its ability to provide accurate absolute BSD values, it is a good indicator that can be confidently used to quantify the relative impact of various design and operating conditions on the characteristics of the gas-liquid dispersion encountered in G/L contactors. This chapter will, therefore, focus on analyzing the results/trends estimated using the advanced DGD method developed in this investigation and compare them with previously-reported trends and results, as well as fundamental phenomena involved in the parameters investigated.

An attempt to fit the estimated BSDs obtained in the present investigation using Log-Normal, and Rosin-Rammler, distributions were undertaken using the sub-functions available in Excel (“LOGNORM.DIST function” and “WEIBULL.DIST function”), and the BSDs were characterized using parameters such as mean and standard deviation around the mean.

In the present investigation, the drag forces acting on individual bubbles were calculated using the well-known fully-contaminated model developed by Tomiyama et al. [1998], unless otherwise specified. As shown in Section 3.3, this model yields bubble rise velocities that are very close to those predicted by many other investigators [Schiller & Naumann, 1935; Ishii and Zuber, 1979] and can be used for a wide range of bubble sizes. It has also been extensively used by investigators to estimate bubble rise velocities [Kawahara et al., 2009; Lane et al., 2016; Liu et al., 2016; Parisien et al., 2017]. In a similar fashion, the expression developed by Griffith & Wallis [1961] to account for the bubble swarming effect was used throughout this investigation, unless otherwise specified. This model was selected because it is almost identical to that proposed by Simonnet et al. [2007], who considered local gas holdups for the swarming effect, but does not suffer from instability when $\Phi_G > 15$ %.

6.1 Reproducibility of the Measured Gas Holdup and Estimated Sauter Mean Diameter

As mentioned in Chapter 4, 90 runs were conducted to determine the reproducibility of the measurements obtained over a wide range of experimental conditions (5 replicates conducted under 18 different conditions). The reproducibility of the steady-state, and Dynamic Gas Disengagement, tests were characterized using the measured average steady-state gas holdups for the former, and the estimated Sauter mean diameter, d_{32}.

The steady-state gas holdups were measured at two regions of the column, at the sparger region and throughout the column, respectively.

The reproducibility values were calculated using a 95 % confidence interval of the mean steady-state gas holdup over the 5 replicates. The steady-state gas holdup reproducibility values of both zones were found to not vary much over a broad range of experimental conditions. However, this value was found to be significantly different between the sparger region (where it has a mean value of about 5 %) and over the column (where it has a mean value of less than 2%). This observation suggests that more instabilities could occur in the sparger region, which is in line with the finding reported by Mouza et al. [2005].

The gas holdup is one of the main characteristics of the performance of gas-liquid dispersion in bubble columns, and it is used to characterize flow regimes in the column. The details of this part are addressed and discussed by Idhbeaa et al. [2022, In Preparation]. Therefore, it will not be elaborated further in this thesis. This work focuses on developing a DGD-based technique for estimating BSDs in a bubble column, mainly for fine gas-liquid dispersions. The reproducibility of d_{32}, a parameter computed from the estimated BSDs, is therefore discussed in two regions of the column.

As seen in Figure 6.1, the 95 % confidence interval of the mean d_{32} under each condition was found to be around or more than doubled in the sparger region compared to that in the whole column. This observation matches the gas holdup reproducibility in this work and the finding reported by Mouza et al. [2005]. The reproducibility of d_{32} was found to be very high in slowly-coalescent systems operated at low U_G values (± 0.9 % with 95 % confidence limits).

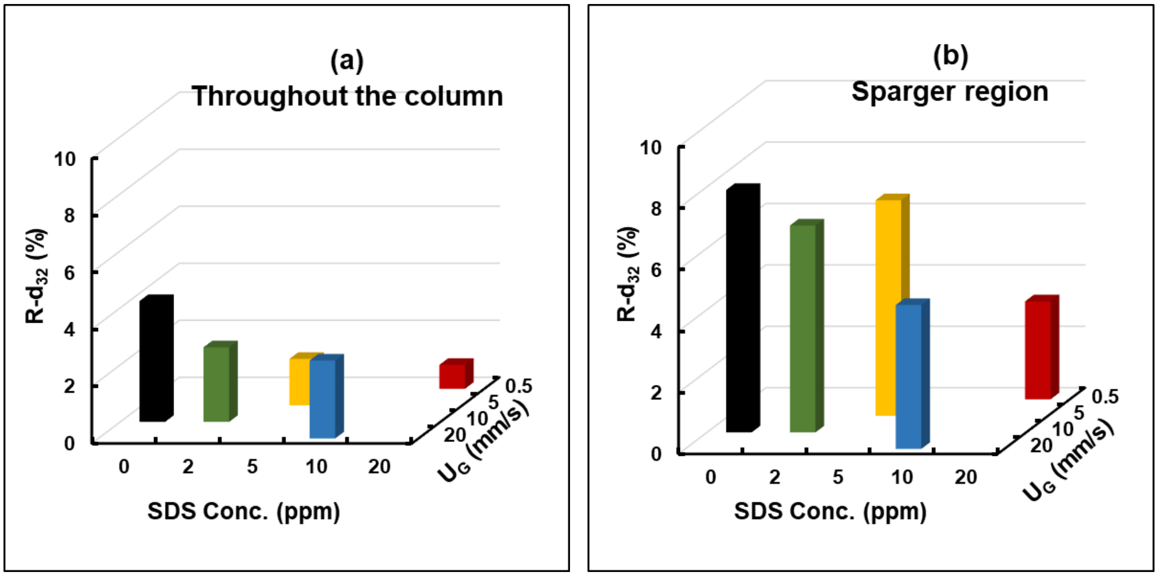

Figure 6.1 Reproducibility results on d_{32}, (a) Throughout the column, (b) Sparger region.

Moreover, the 95 % confidence interval of the mean d_{32} in both regions was found to increase as the system transferred from a slowly coalescent system to a rapidly coalescent system. This can be attributed to the broader BSDs achieved in rapidly coalescent systems, which results in more instabilities under such conditions. The varying BSDs achieved under different coalescence retarding systems will be discussed in Section 6.2.

6.2 Bubble Size Distributions

Bubble size distribution (BSD) is one of the main characteristics estimated from the newly developed DGD method. In this section, the effect of G/L ratios and the impact of coalescence retardation on BSDs are discussed. Moreover, the BSD trends achieved by the DGD method in this work are compared to other investigations and fundamental understandings.

6.2.1 Effect of Gas-to-Liquid Ratio on BSD

The distributive BSDs obtained with different G/L ratios were compared in Figure 6.2.

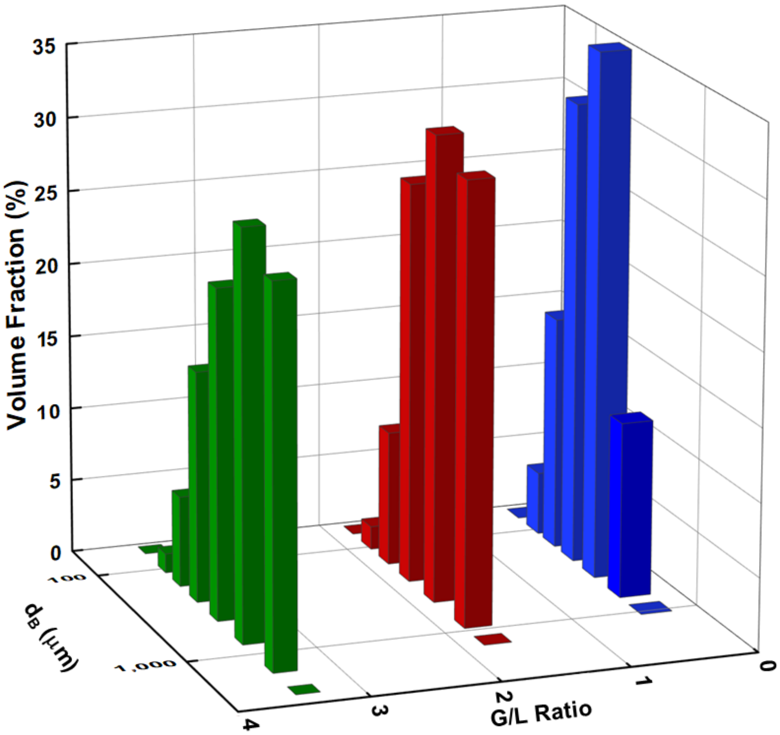

Figure 6.2 Effect of U_G on distributive BSDs (Throughout the column, C_{SDS} = 50 ppm, A_{Th} = 22 mm^2 , Q_L = 7 L/min).

As seen in the graph, the BSD became broader and broader with the increase of G/L ratios, which indicated that coarser bubbles were generated at high G/L ratios. This is in line with BSD results reported by Muroyama et al. [2013]. Based on the findings of Idhbeaa [2022, In Preparation], this behaviour can be due to the transition from true-homogeneous and pseudo-homogeneous flow regime as a result of increasing gas holdups as G/L ratios (increasing U_G with constant U_L) increased. In a slowly-coalescent system (50 ppm SDS), the increased gas holdup would reduce the gap between bubbles and thus enhance bubble-bubble interactions and facilitate the formation of clusters of bubbles. Therefore, the trend observed in Figure 6.2 supported the flow regimes observed in the whole column.

6.2.2 The Impact of Coalescence Retardation on BSD

The presence of contaminants in the water, and their tendency to adsorb at the G/L interface, is known to increase its interfacial elasticity, a factor that significantly retards bubble breakage and coalescence processes [Chesters, 1991]. The estimated BSDs, obtained in both the sparger region and the column, as well as various surfactant concentrations, were used to show the impact of coalescence retardation with comparisons of previous findings.

6.2.2.1 Effect of Bubble Coalescence throughout the Column

As mentioned in Chapter 4, the DGD experiments were conducted at two regions, one is throughout the column, and the other is at the sparger region. The estimated BSDs obtained from these two regions can be used to show the effect of bubble coalescence tendencies throughout the column. An example is depicted in Figure 6.3, which compares the BSDs obtained from these two regions under the same experimental condition in a relatively rapidly coalescent system.

The difference between BSDs obtained from these two regions may be attributed to two reasons:

- Gas expansion due to the hydrostatic pressure decrease with column height (shown as the dotted line in Figure 6.3).

- Bubble coalescence along the axial of the column.

As seen in Figure 6.3, clearly indicates that the effect of bubble coalescence is more significant than that of gas expansion. Therefore, the difference of estimated BSDs observed at different regions of the column is in line with the fundamental understanding that the bubbles tend to coalescence as they flow axially through the column, particularly in rapidly coalescent systems.

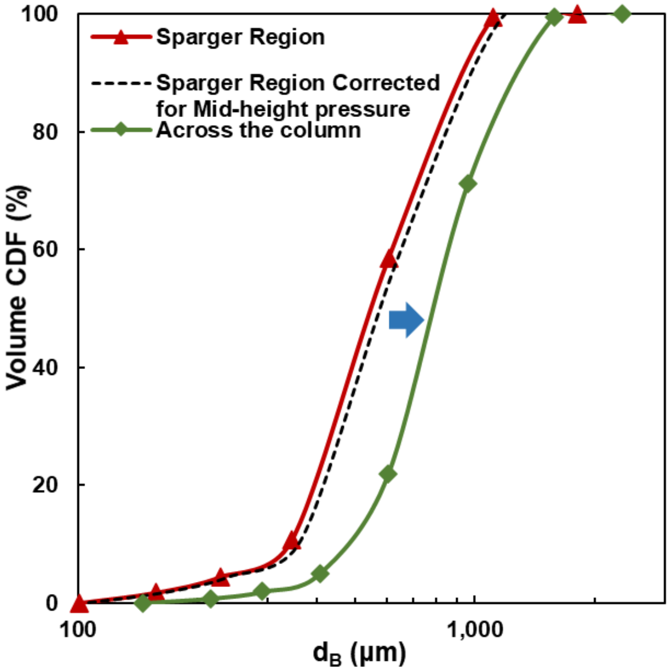

Figure 6.3 Effect of bubble coalescence throughout the column (C_{SDS} = 5 ppm, ΔP_{Sp} = 210 kPa, Q_L = 7 L/min, U_G = 5 mm/s).

6.2.2.2 Effect of Surfactant Concentration on BSDs

As discussed in 6.2.2.1, bubbles tend to coalescence along with the column height. However, the rate at which the bubble coalescence is strongly impacted by the presence of contaminants reduces bubble coalescence rates (because of their impact on the interfacial elasticity, "the Marangoni Effect"). This is particularly important under the low energy dissipation rates encountered at relatively small U_G values used in the present investigation. It was, therefore, necessary to investigate the impact of varying SDS concentrations on the resulting estimated BSDs.

Figure 6.4a depicts the effect of SDS concentration on the cumulative BSD observed in the whole column. The bubbles obtained using tap water could, for all practical purposes, be considered as being monodisperse, thus was not included in the graph. However, increasing polydispersity was observed to develop in the presence of SDS, with finer BSD being observed to prevail at higher SDS concentrations (which, in turn, is associated with increasing coalescence retardation). As can be seen from Figure 6.4b, the addition of 50 ppm SDS to tapwater resulted in:

- a 5-fold increase in Φ_G,
- an 8-fold reduction in d_{32},

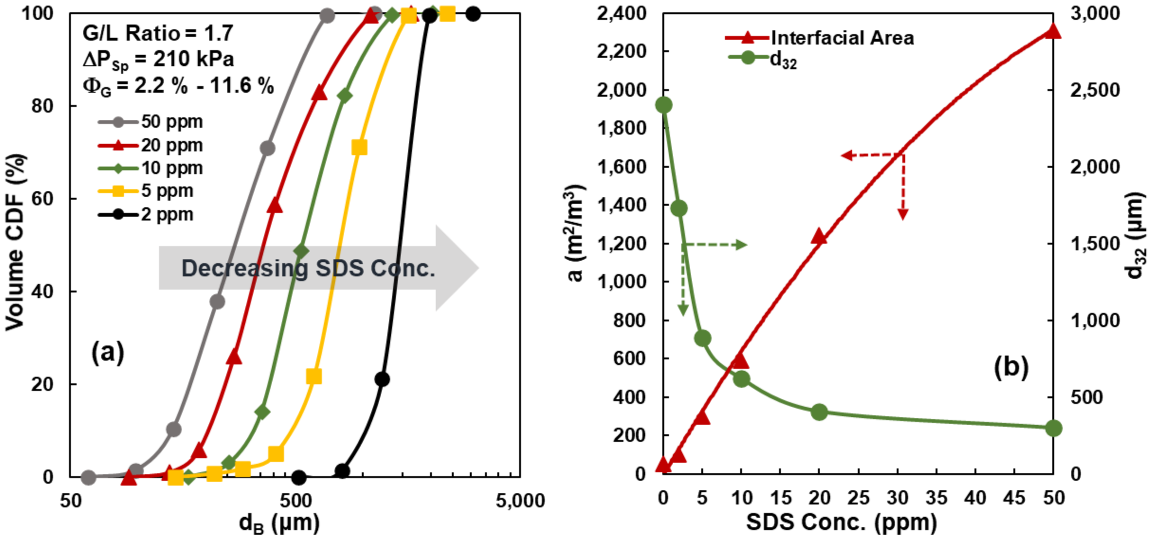

Figure 6.4 Effect of contaminant levels on (a) BSD maintained throughout the column, (b) Interfacial area of contact, and d_{32} value, in the sparger region.

More significantly, the combined effect of the increased gas holdup, and the prevalence of finer bubbles in the column, resulted in an almost linear relationship between the interfacial area of contact and SDS concentration, generating up to a 40-fold increase in the interfacial area of contact. Such observation could explain the beneficial impact that contaminants can have on the volumetric mass transfer coefficient observed in bioreactors, despite their adverse impact on k_L values [Luna-Brito et al., 2018].

The aforementioned phenomena could be attributed to the growing tendency to form finer bubbles when increasingly contaminated systems are pre-dispersed using venturi spargers [Chesters, 1991; Pallapothu & Al Taweel, 2012]. Although the very fine bubbles introduced at the bottom of the column are thermodynamically unstable and tend to coalesce as they rise through the column, the bubble coalescence rate in microbubble-aerated columns operating in the homogeneous/pseudo-homogeneous regime is slowed down by:

- the low rate of energy dissipation in the column (which affects bubble collision rate), and
- the contaminant concentration (which affects bubble coalescence efficiency).

6.3 Interfacial Areas of Contact

Interfacial areas of contact were computed from the estimated BSDs in our advanced DGD method. In this section, the effect of superficial gas velocity and pressure drops across the sparger on interfacial areas is discussed. Besides, the estimated interfacial areas obtained from the sparger region and those throughout the column were compared.

6.3.1 Effect of Superficial Gas Velocity and Pressure Drop Across the Sparger on Interfacial Area Generated

As mentioned in Chapter 4, in addition to superficial gas velocity, the pressure drop across the sparger (ΔP_{Sp}) is also a parameter that can be adjusted to control bubble sizes generated in the sparger. Therefore, the effect of both U_G and ΔP_{Sp} on interfacial areas was investigated, as seen in Figure 6.5.

Increasing the pressure drop across the sparger could contribute to higher Interfacial areas of contact. This observation could be attributed to the tendency to form finer bubbles at higher ΔP_{Sp}. This, in turn, results in the formation of higher interfacial areas of contact in the column. A similar trend was found when comparing gas holdup results with different pressure drops across the sparger, the details of which are discussed in Idhbeaa et al. [2022, In Preparation]. thesis. Moreover, Bae et al. [2021] also reported that the increase of pressures could contribute to generating finer bubbles.

Besides, it is obvious in Figure 6.5 that interfacial areas increase with the increase of U_G but tend to plateau or even slightly decrease at relatively high U_G values. As reported by Idhbeaa et al. [2022, In Preparation], at U_G = 5 mm/s, whereas a true homogeneous flow was obtained at 350 kPa, a transit occurred from true-homogenous flow to pseudo-homogeneous at 210 kPa, which explains the slight decrease of the interfacial area from 5 mm/s to 10 mm/s under this condition. Therefore, the trends observed in Figure 6.5 explain the flow regime transition from true homogeneous flow to pseudo-homogeneous flow. In pseudo-homogenous flow, the bubbles tend to form clusters and reduce the gap between bubbles, which facilitates bubble coalescence tendencies and, therefore, reduces the interfacial area of contact.

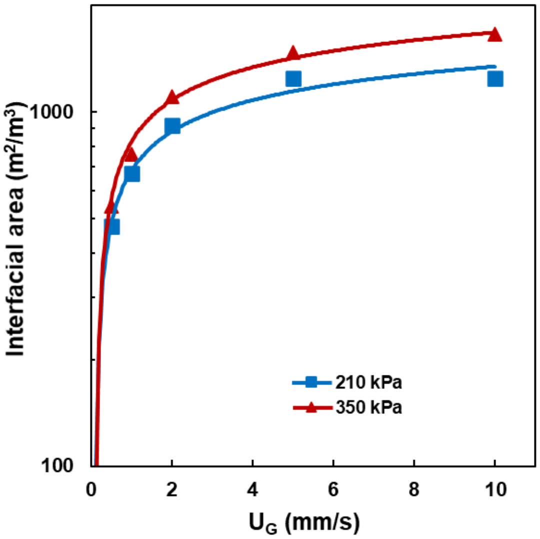

Figure 6.5 Effect of superficial gas velocity on the interfacial area of contact. (Throughout the column, C_{SDS} = 20 ppm, Q_L = 7 L/min).

6.3.2 Comparison of Interfacial Areas at Different Parts of the Column

The flow behaviour between the region near the sparger and throughout the column can be very different due to the different mixing patterns. In order to differentiate the effect of flow behaviour between two regions and the effect of coalescence throughout the column, as seen in Figures 6.6 and 6.7, the measured gas holdups and estimated interfacial areas in two regions of the column were compared under a more slowly-coalescent system (50 ppm SDS Conc.) and a relatively slightly-coalescent system (10 ppm SDS Conc.), respectively.

The gas holdup results obtained in the sparger region were found to be higher than those achieved throughout the column under both SDS Conc. The difference became more significant as U_G increased and increased coalescence retardation tendencies (i.e., higher SDS Conc.). A similar trend was found in the results of interfacial areas, as seen in Figures 6.6b and 6.7b, for both higher and lower SDS Conc. systems. However, the differences between the two regions were much larger than those in gas holdup results. Moreover, this difference became more significant under more slowly-coalescent systems (50 ppm SDS Conc.). The observation found in this work could most probably explain the finding reported by Anastasiou et al. [2013] and Mouza et al. [2018] that a mixing region was formed in the sparger region, whereas flow conditions in the column are closer to plug flow. In a well-mixed region under relatively more slowly-coalescent systems, the mixing could facilitate bubble-bubble interaction and enhance the bubble breakage rather than the bubble coalescence, which as a result, generate finer bubbles and increase the interfacial areas.

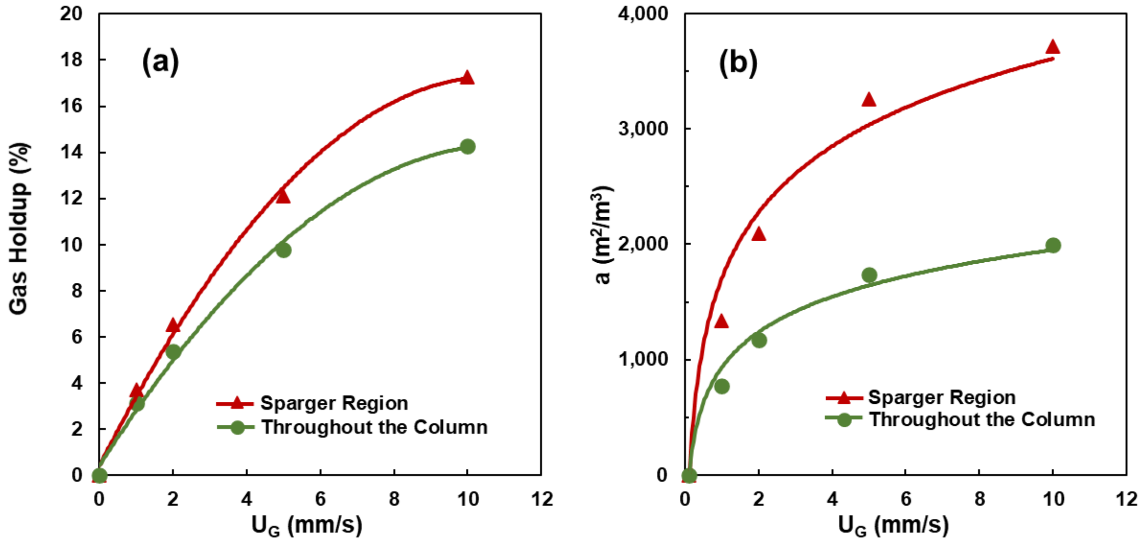

Figure 6.6 Effect of superficial gas velocity at different regions of the column on (a) gas holdups; (b) interfacial areas (C_{SDS} = 50 ppm, Q_L = 7 L/min).

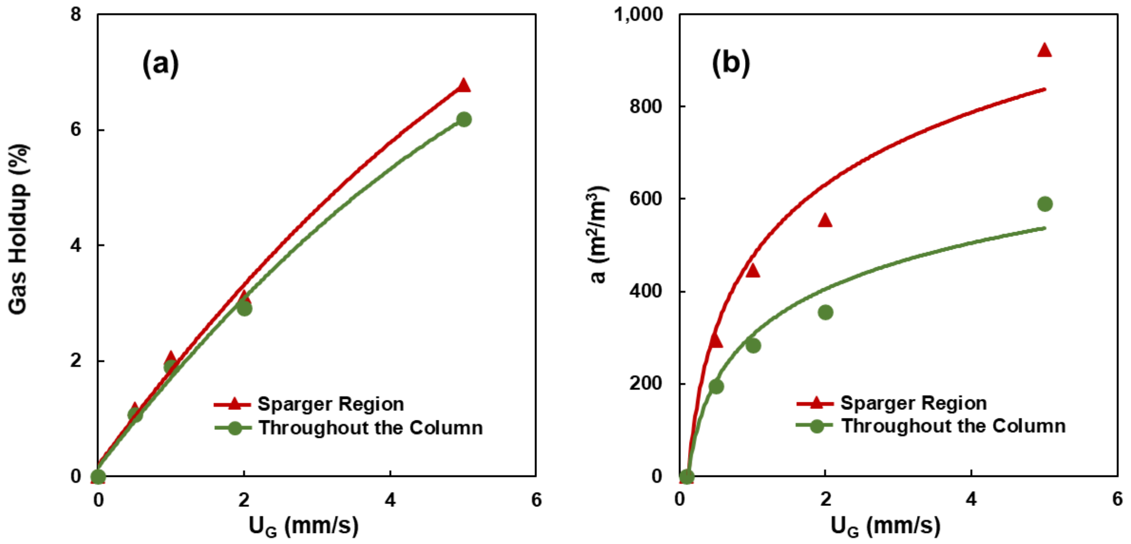

Figure 6.7 Effect of superficial gas velocity at different regions of the column on (a) gas holdups; (b) interfacial areas (C_{SDS} = 10 ppm, Q_L = 7 L/min).

6.4 An Overall Characterization of Gas/Liquid Dispersions

In addition to interfacial areas of contact, various mean bubble diameters (d_{10}, d_{20}, d_{30}, d_{32}, d_{43}) and bubble number density (N_B) were computed from the estimated BSDs using the newly-developed DGD method in this investigation. This section discusses the effect of various operating parameters (e.g., U_G, ΔP_{Sp}, and SDS Conc.) on mean bubble diameters and bubble number density. Besides, since the newly-developed DGD method allows the users to select the desired model based on their needs, the effect of different models for single bubble and bubble swarms is investigated on estimated d_{32} values.

6.4.1 Effect of Superficial Gas Velocities and Surfactant Concentration on Various Mean Bubble Diameters

Various mean bubble diameters are commonly used for assessing gas-liquid dispersions in many applications. There are five mean bubble diameters that were computed from the estimated BSDs in this work. Mean bubble diameters, d_{10}, d_{20}, and d_{30}, are length mean diameter, surface mean diameter, and volume mean diameter, respectively. The Sauter mean diameter, d_{32}, can also be referred to as volume surface mean diameter. It is most important when interfacial areas of contact are of interest. The De Brouckere mean diameter, d_{43}, is the volume-weighted mean diameter. [Foust, 1980; Alderliesten, 2005].

Figure 6.8a depicts the effect of U_G on various mean bubble diameters computed from the estimated BSD results. The overall trend is similar for all mean bubble diameters, in which the mean bubble diameters tend to increase with the increase of U_G. However, the variances between different mean bubble diameters in Figure 6.8a clearly reflect their physical meanings. For instance, at the same U_G value, the volume mean diameter, d_{30}, was larger than the surface mean diameter (d_{20}) and length mean diameter (d_{10}). More significant variances were found in d_{32} and d_{43} values under the same superficial gas velocity. The Sauter mean bubble diameter d_{32} increased when the volume surface ratio increased with the increase of U_G values. This can be attributed to large bubbles generated in the column under high superficial gas velocities and, as a result, reduce the interfacial areas. Therefore, the observation found in Figure 6.8a fits the discussion made in Section 6.3.1. The d_{43} value at relatively high U_G values was found to be significantly larger than the d_{32} value because the volume-weighted mean diameter, d_{43}, is more sensitive to the larger bubbles in the BSDs.

All mean bubble diameters were then used to investigate the effect of surfactant concentration, as shown in Figure 6.8b. The tests were conducted throughout the column under the same U_G with different SDS concentrations. It is obvious to see that smaller mean bubble diameters were generated and maintained under slowly-coalescent systems, which confirms the finding discussed in Section 6.2.2.2 that adding contaminants in the water could help retarding the bubble coalescence throughout the column.

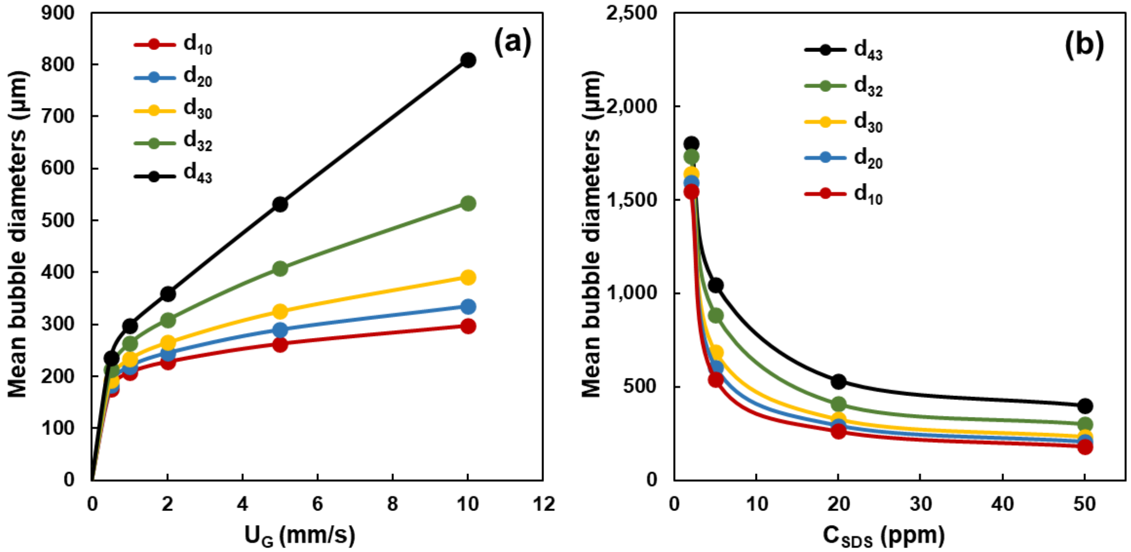

Figure 6.8 Effect of U_G and SDS Conc. on various mean bubble diameters, Throughout the column, ΔP_{Sp} = 210 kPa, Q_L = 7 L/min, (a) C_{SDS} = 20 ppm; (b) U_G = 5 mm/s.

6.4.2 Effect of Drag Models on Sauter Mean Bubble Diameter

The advanced DGD method developed in this investigation allows the users to select the desired model amongst a list of models (drag models on single bubbles and models accounting for the crowding effect) based on their needs. Although the BSDs reported in this thesis are estimated from the fully-contaminated model developed by Tomiyama et al. [1998] for single bubble and Griffith & Wallis's model [1961] account for the bubble swarming effect, two more models were used for single bubbles and for bubble swarms respectively to verify the advanced DGD method on estimating BSDs and their computed parameters.

In Figure 6.9, estimated d_{32} values obtained from different surfactant concentrations were compared among three models developed for single bubbles. Karamanev's model [1996] and Tomiyama's fully-contaminated model [1998] were developed for contaminated systems, whereas the model proposed by Schiller and Naumann [1935] was for rigid spheres. As seen in Figure 6.9a, the maximum d_{32} was found to be around 539 μm with the U_G ranges examined in this work. Under this surfactant concentration (20 ppm of SDS), all three models gave almost the same estimated d_{32} values. However, as seen from Figure 6.9b, the tests were done with a much lower surfactant concentration (2 ppm of SDS), in which the estimated d_{32} values could reach as high as about 2,444 μm. Tomiyama's fully-contaminated [1998] and Schiller and Naumann [1935] under this condition still showed the same estimated d_{32} values. However, Karamanev's model [1996] resulted in a noticeable increase in estimated d_{32} values, and the difference became more significant with the increase of U_G values.

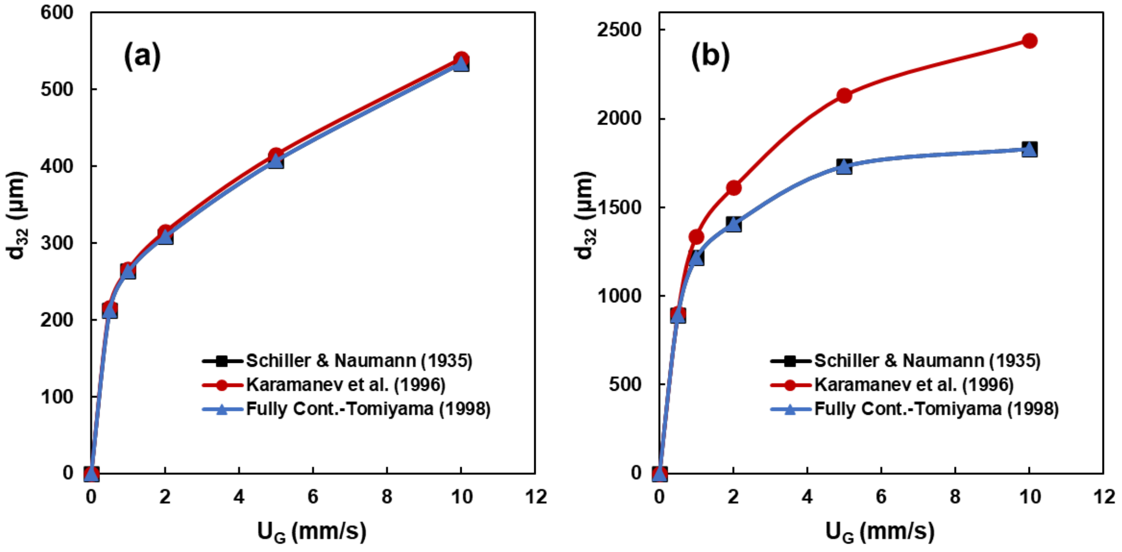

Figure 6.9 Effect of drag models of single bubbles on estimated d_{32} (Throughout the column, ΔP_{Sp} = 210 kPa, Q_L = 7 L/min), (a) C_{SDS} = 20 ppm; (b) C_{SDS} = 2 ppm.

To illustrate the capability of the newly-developed technique, a comparison of various models accounting for adjacent bubbles was made under two conditions with different gas holdup ranges. The maximum gas holdup in Figure 6.10a is around 11 % and is about 24 % in Figure 6.10b. As seen in Figure 6.10, the model proposed by Griffith & Wallis [1961] gave almost identical results with the polynomial fit derived from Simonnet's model [2007] (details were discussed in Section 3.5) under both conditions. However, Lockett and Kirkpatrick's model [1975], which was accepted by several investigators [Lane et al., 2016; Parisien et al., 2017], resulted in a 2.6 % increase in the estimated d_{32} values at $\Phi_G \approx 11$ % and a 3.7 % increase in the estimated d_{32} values at $\Phi_G \approx 24$ %. This observation is in line with the curves in Figure 3.6 that a slightly more effect of bubble swarms on drags was considered by Lockett and Kirkpatrick [1975], especially at relatively high gas holdups.

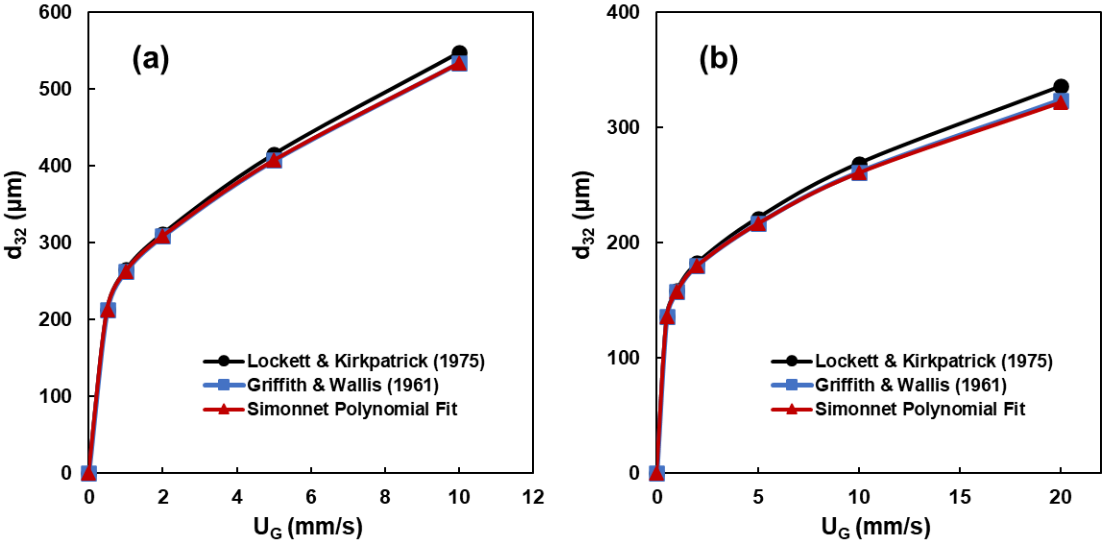

Figure 6.10 Effect of drag models accounting for adjacent bubbles on estimated d_{32}, (a) Throughout the column, $\Delta P_{Sp} = 210$ kPa, $Q_L = 7$ L/min, $C_{SDS} = 20$ ppm, $\Phi_G \leq 11.1$ %; (b) Sparger region, $A_{Th} = 22$ mm^2, $Q_L = 7$ L/min, $C_{SDS} = 50$ ppm, $\Phi_G \leq 24.1$ %.

6.4.3 Effect of Superficial Gas Velocity and Pressure Drops on Bubble Number Density

Bubble number density is one of the computed parameters from the estimated BSDs, which plays an important role in flotation columns. The computed N_B values under various U_G at different pressure drops across the sparger were compared in Figure 6.11. For the experimental conditions delineated in this figure, the N_B value was found to increase with increasing U_G, reaching a maximum of around 2 mm/s, beyond which it decreased with increasing U_G. This is very much in line with the discussion presented in Section 6.2.1 and is most probably caused by the large bubbles generated and maintained throughout the column at relatively high superficial gas velocities. Similarly, the N_B values generated at higher ΔP_{Sp} values (350 kPa) are significantly larger than those generated at relatively low ΔP_{Sp} (210 kPa). This is very much in line with the observations made in Section 6.3.1 based on interfacial area estimates.

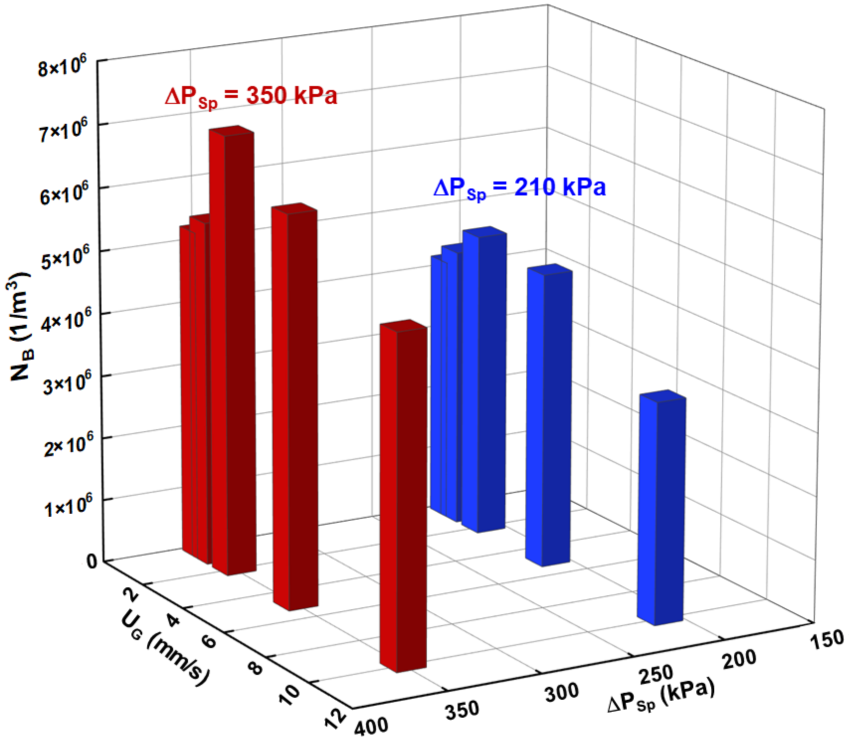

Figure 6.11 Effect of U_G on bubble number density (Throughout the column, C_{SDS} = 20 ppm, Q_L = 7 L/min).

6.5 Comparison With Previous Work

The gas holdup results measured in the column and the interfacial areas of contact estimated from the advanced DGD method were compared to those reported in previous works. Both of them were compared with investigations conducted using conventional perforated spargers in contaminated systems.

6.5.1 Gas Holdup

The gas holdup results generated by the ADPV sparger in this work were compared with those generated by conventional perforated spargers in previous works. As seen in Figure 6.12, all gas holdup results were obtained in contaminated systems. The use of conventional perforated spargers to aerate pilot-scale bubble columns in the presence of 500 ppm Ethanol yields gas holdups that are linearly proportional to U_G, regardless of the type of sparger used (e.g., spider or perforated-plate) [Besagni & Inzoli, 2017; Gemello et al., 2018]. On the other hand, significantly higher gas holdups could be achieved when the more effective porous spargers were used in the presence of 600 ppm SDS [Anatasious et al., 2010].

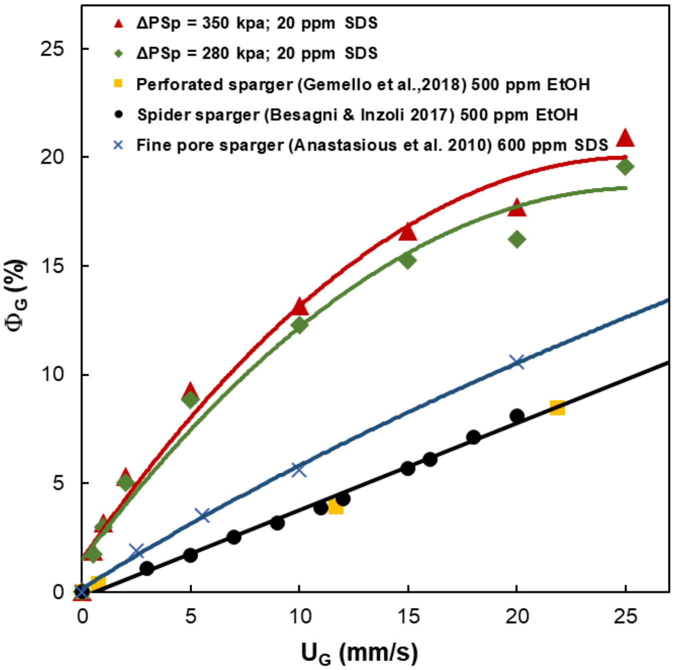

Figure 6.12 Comparison of gas holdups obtained throughout the column in this work and previous works.

On the other hand, a multifold increase in gas holdup was achieved using the ADPV sparger (even at a fraction of the SDS concentration), particularly at low superficial gas velocities and higher pressure drops across the sparger. This beneficial effect can generally be attributed to:

- The ability of the ADPV spargers to generate fine bubbles in the presence of contaminants [Al Taweel et al., 2003]. These fine bubbles tend to coalesce slower as they rise through the tall columns, particularly at low agitation intensities and in the presence of effective coalesce retardants (i.e. contaminants),
- The fine bubbles maintained within the column exhibit reduced slip velocities between the phases, a factor that is accentuated by the interfacial-immobilization in the presence of contaminants. The combined effect of these two factors results in increasing gas holdup.
- The effect of increasing U_G on gas holdup results can be reduced once the hydrodynamic conditions in the column become unstable and the homogeneous flow regime ceases to exist.

6.5.2 Interfacial Area of Contact

Although the advanced DGD method developed in this investigation can only give estimated interfacial areas of contact, the comparison of gas holdup results between this work and previous investigations could help demonstrate the estimated interfacial area trend when it is compared with other works.

As discussed in 6.5.1, the ADPV sparger is capable of generating finer bubbles rather than that of conventional perforated spargers. As a result, the estimated interfacial areas of contact generated by the ADPV sparger and maintained in contaminated systems are expected to show a similar trend. The results estimated using the newly developed advanced DGD method were therefore used to assess the aforementioned expectations. A preliminary comparison between the data generated in the present investigation and those reported by previous investigators, using a spider sparger in the presence of 500 ppm Ethanol and 4,000 ppm NaCl, was made, as seen in Figure 6.13. The results obtained in this work show an order-of-magnitude enhancement in the interfacial area of contact compared to those reported by Basagni & Inzoli [2017], although they used very high contaminant concentrations. This observation is in line with the gas holdup comparison.

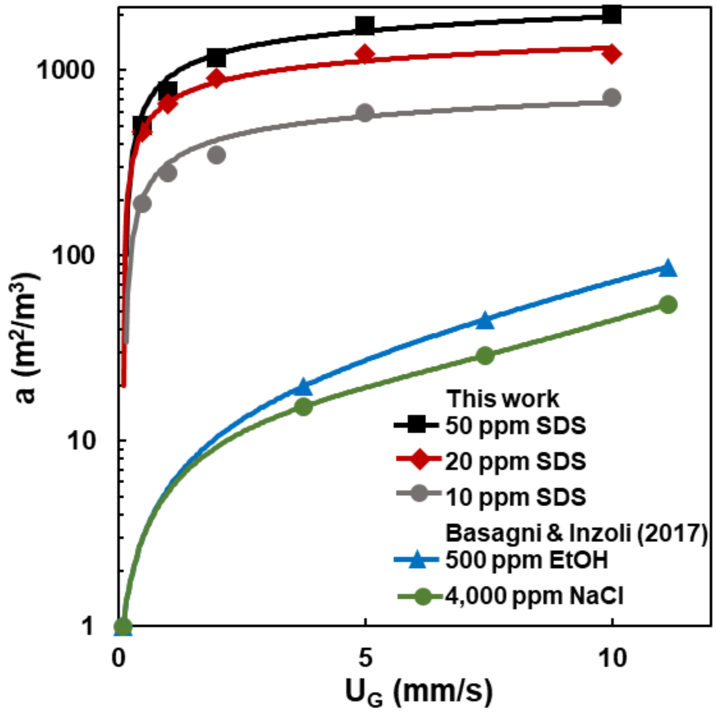

Figure 6.13 Comparison of interfacial areas of contact generated and maintained throughout the column in this work and the work reported by Basagni & Inzoli [2017].

6.6 Fitting the Estimated Bubble Size Distributions to Theoretical Ones

The experimental work conducted by Gordiychuk et al. [2016], Li et al. [2017], and Zhao et al. [2019] indicates that the BSD generated by Venturi-type spargers tends to depict a unimodal log-normal distribution in both contaminated and uncontaminated systems. This distribution, as well as the closely related Rosin-Rammler (Weibull), are the one most commonly reported for describing the volume and number density generated by porous spargers [Parthasarathy and Ahmed, 1996; Mouza et al., 2005; Kazakis et al., 2008; Ohde et al., 2021], and those encountered in bubble columns operating at atmospheric and elevated pressures

[Zhang et al., 2008; Li et al. 2013; Parisien et al., 2017; Basha and Morsi, 2018; Prakash et al., 2020].

The interfacial area available for interphase mass transfer is an important design/operating parameter that is influenced by the combined effect of gas holdup and Sauter mean bubble diameter. These, in turn, are influenced by a wide range of design and operating parameters as well as the physicochemical properties of the gas/liquid system. It is therefore important to identify the possibility that the results obtained in the present investigation can be similarly fitted.

In order to accurately analyze the BSD data estimated using this novel technique, it is necessary to use advanced statistical analysis methods (such as “OriginPro - Data Analysis and Graphing Software” used by SOPAT, or Excel SPC) in order to accurately identify the various characteristics associated with the estimated BSD, in which the Kolmogorov-Smirnov and Anderson-Darling tests can be used to assess the goodness of fit. However, such an effort is beyond the scope of the present investigation, and a simpler approach was used.

An attempt was undertaken in this work to fit the experimentally determined BSD to various standard distributions (as Log-normal or Rosin-Rammler distributions). This was accomplished using the following simple fit functions provided in Microsoft 365 EXCEL:

- “LOGNORM.DIST function” to analyze data that has been logarithmically transformed. This program generates the lognormal distribution of x, where ln(x) is normally distributed, and characterizes it using two parameters, namely the “mean value” and the “standard deviation” around the mean. These two parameters were therefore used as indicators of the “mean tendency” and “spread around the mean” of the BSD obtained in the present investigation.
- “WEIBULL.DIST function” to make the reliability analysis. This program generates the Weibull (Rosin-Rammler) distribution of x and characterizes it using two parameters, namely the “shape parameter” and the “scale

parameter”. Therefore, these two parameters were used to calculate the “mean tendency” and “spread around the mean” of the BSD obtained in this work.

The aforementioned simple technique is satisfactory for the purposes of this investigation. However, because a linear fitting technique was used to fit the experimental results discussed in this thesis, the ensuing results may not be accurate.

An example of fitting the estimated BSD to typical distributions using the simple approach in this work is depicted in Figures 6.14 and 6.15 for cumulative and distributive distributions, respectively. The BSD in terms of volume fraction, interfacial area, and bubble number density are presented in the figures. Both Log-Normal and Rosin-Rammler distributions were found to fit the three types of BSDs reasonably well. This is very much in line with the findings of previous investigators and confirms the suggestion that, although the newly-developed technique may not yield exact values of the BSD, it can be confidently used for comparative evaluation of the effect of various designs and operating parameters.

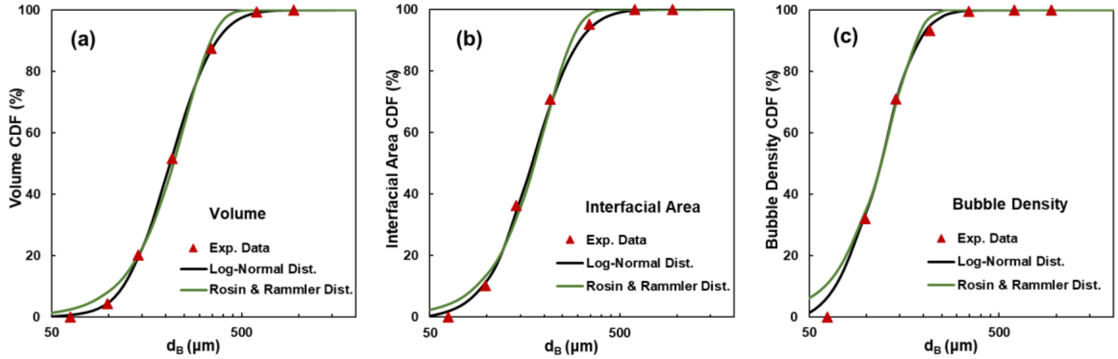

Figure 6.14 Attempts to fit the cumulative density functions (a) volume, (b) interfacial area of contact, (c) bubble number density by theoretical distributions (Log-Normal and Rosin-Rammler distributions (Throughout the column, C_{SDS} = 50 ppm, A_{Th} = 22 mm^2, Q_L = 7 L/min, U_G = 1 mm/s).

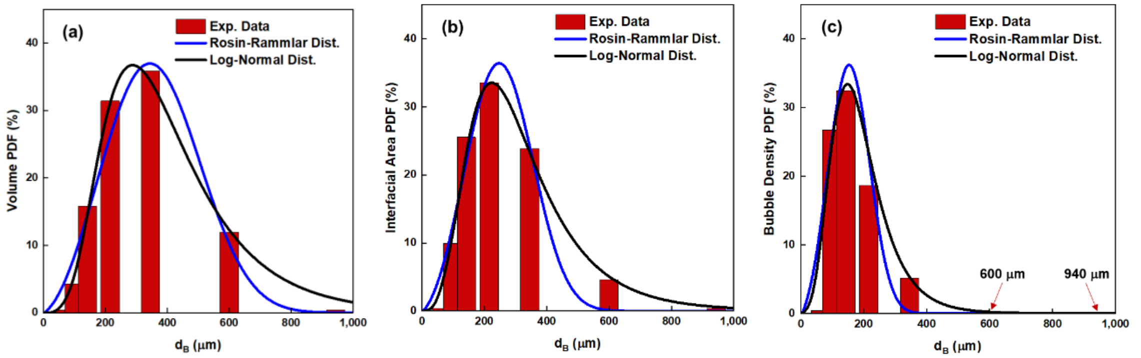

Figure 6.15 Attempts to fit the distributive density functions (a) volume, (b) interfacial area of contact, (c) bubble number density by theoretical distributions (Log-Normal and Rosin-Rammler distributions (Throughout the column, C_{SDS} = 50 ppm, A_{Th} = 22 mm^2, Q_L = 7 L/min, U_G = 1 mm/s).

In this case, the Log-Normal distribution seems to fit the experimental BSDs better than the Rosin-Rammler distribution. However, a comprehensive analysis of the thoroughly quantitative BSD fit analysis (including the goodness of fit) and the comparison between two typical distributions over a broad range of experimental conditions are needed in future work to generalize such findings confidently.

The function "LOGNORM.DIST(x, μ, σ, FALSE)", which is built into Microsoft 365 EXCEL, linearly fits a Log-Normal distribution to the natural-log values of the experimentally-obtained probability density functions describing the bubble size distribution. The resulting fit is described using two adjustable parameters, μ and σ, and covers a range varying between x = 0 and x= ∞. It is given by,

$$f(\mathrm{x}) = \frac{1}{x\sigma\sqrt{2\pi}} e^{-\frac{1}{2}(\frac{\ln x-\mu}{\sigma})^2} \tag{6.1}$$

Some of the key statistical properties associated with that distribution are given in Table 6.1.

Table 6.1 Key statistical properties of Log-Normal distribution.

Mean	$e^{\mu+\sigma^2/2}$
Median	e^{μ}

Mode	$e^{\mu-\sigma^2}$
Variance	$(e^{\sigma^2}-1)e^{2\mu+\sigma^2}$
Skewness	$(e^{\sigma^2}+2)\sqrt{e^{\sigma^2}-1}$
Kurtosis	$e^{4\sigma^2}+2e^{3\sigma^2}+3e^{2\sigma^2}-6$

In the following analysis, attention is focused on only two of the statistical parameters listed above, namely the mean and variance, and the findings are used to gain a better understanding of the important role that bubble coalescence plays in controlling the generation and maintenance of gas/liquid dispersions. In Figure 6.16, attention is focused on two quantitative parameters that characterize the gas-liquid dispersion obtained in the sparger region (the relatively small region close to the sparger), where bubble coalescence is relatively slow due to the presence of 50 ppm of SDS. Therefore, one can comfortably assume that the information obtained through such an analysis closely represents the gas/liquid dispersion delivered by the ADPV sparger.

As shown in Figure 6.16a, the smallest bubbles were observed at the lowest U_G values, and their size linearly increases with progressively increasing U_G values. Several investigators, who studied the performance of the venturi sparger, reported similar trends, a phenomenon that is attributed to the larger gas-to-liquid ratios passing through the sparger. However, the results that are shown in Figure 6.16a depict a very small concave propensity which is most probably caused by the tendency of the bubbles to coalesce at the higher gas holdups associated with larger U_G values. This is clearly evident from the results shown in Figure 6.16b, where the relative changes in the magnitude of the PDF variance are more significant than those attributed to enlarged mean values. Therefore, one can conclude that the BSDs obtained under the conditions associated with Figure 6 16 are essentially self-similar, with a progressively increasing mean value and broader BSDs. The very slow bubble coalescence tendencies somewhat accentuate the latter.

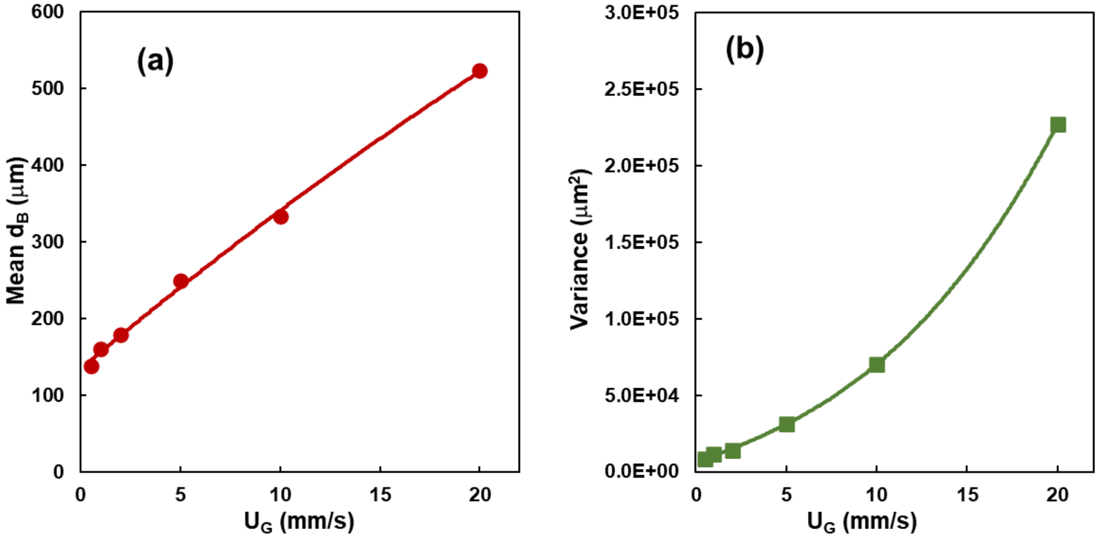

Figure 6.16 Effect of superficial gas velocity on Log-Normal characterization parameters in terms of volume fraction, (a) Mean bubble size, (b) BSD Variance (Sparger region, C_{SDS} = 50 ppm, A_{Th} = 22 mm^2, Q_L = 7 L/min)

Similar conclusions can be drawn when one analyses the estimated average BSD prevalent throughout the column (Figure 6.17).

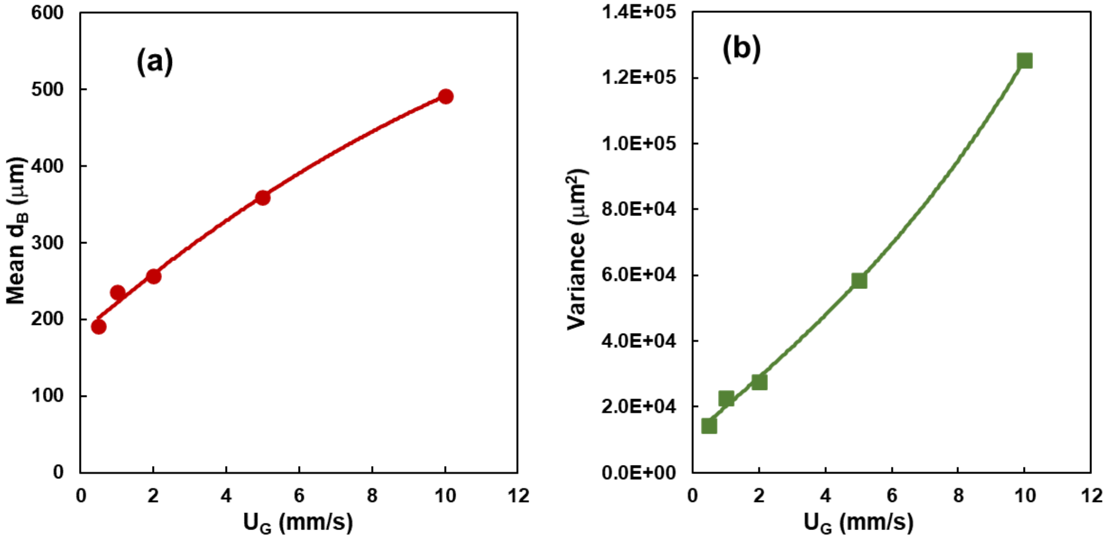

Figure 6.17 Effect of superficial gas velocity on Log-Normal characterization parameters in terms of volume fraction, (a) Mean bubble size, (b) BSD Variance (Throughout the column, C_{SDS} = 20 ppm, ΔP_{Sp} = 350 kPa, Q_L = 7 L/min).

However, more significant bubble coalescence is expected to be prevalent in this case due to the larger gas phase residence times and the greater propensity for bubbles to coalesce in the presence of only 20 ppm of SDS. This is reflected in the more significant deviation from linear behaviour shown in Figure 6.17a and in the relative changes in variance shown in Figure 6.17b being even more prominent than the similar tendencies shown in Figure 6.16b.

The observations made above further confirm the conclusion that the improved DGD technique developed in this investigation can be confidently used to quantify the relative impact of various design and operating conditions on the characteristics of the gas-liquid dispersion encountered in G/L contactors.

CHAPTER 7 CONCLUSIONS & RECOMMENDATIONS

In this investigation, a simple and cost-effective approach for estimating the bubble size distribution obtained in microbubble-aerated columns was developed. It is based on the well-known Dynamic Gas Disengagement technique commonly used to estimate the bubble sizes encountered in bubble columns. It, however, extends its capability from predicting only two to three classes (large and small or large, middle, small) into a fully-fledged bubble size distribution. This data analysis program was incorporated within an automated control/data collection and analysis program, thereby reducing the efforts needed from the operator.

In its modelling, the algorithms used for estimating the BSD are based on the extensive body of fundamental knowledge generated by CFD studies. The user is therefore given the option to select amongst a wide range of models for the terminal rise velocity of single bubbles and those used to quantify the impact of adjacent bubbles on the swarm velocity. It can therefore be used to:

- Estimate the bubble size distributions under the different hydrodynamic conditions encountered in varying regions of the bubble column. These results can be used to calculate the interfacial area of contact between the phases and calculate a wide range of characteristic mean bubble diameters (d_{10}, d_{20}, d_{30}, d_{32}, d_{43}) and bubble number densities, and can be fitted by theoretical distributions (such as log-normal and Rosin-Rammler distributions),
- The advanced bubble size estimation method is generally confined to relatively small bubble sizes where a relatively flat gas holdup profile is expected to prevail. The specific BSD range can be limited by the models used. For example, this advanced DGD method can only be used up to 2440 μm when the Tomiyama fully-contaminated model is used in conjunction with the bubble swarm model proposed by Griffith & Wallis.
- The number of classes that can be used to describe the BSD was identified using a simple optimization technique. Under the hydrodynamic conditions

used in the present investigation and the aforementioned models, the optimal number varied between 5 and 11 classes. Smaller class numbers were observed under rapidly coalescent conditions.

Although an extensive comparison with results obtained using another independent bubble size measuring technique is needed to further enhance confidence in the newly developed DGD method, the results/trends obtained in the present investigation are very much in line with previous experience and/or trends predicted on the basis of fundamental understanding. For example:

- The reproducibility by which d_{32} can be predicted is very high, particularly in slowly-coalescent systems operated at low U_G values (± 0.9 % confidence limits),
- The estimated BSD throughout the column was found to move to the coarser bubble side compared to that generated in the sparger region in a rapidly coalescent system. This matches the fundamental understanding that bubble tends to coalescence throughout the column, particularly in rapidly coalescent systems.
- The BSD estimated by the newly developed DGD method became finer (smaller d_{32}) and broader (more bubble classes) with higher SDS concentrations. This is in line with the increased Φ_G values obtained under such conditions,
- The estimated interfacial areas encountered in the sparger region were significantly larger than those throughout the column under slowly coalescent systems, particularly at high U_G values. This is most probably caused by the formation of a mixing region in the sparger region, which is in line with the findings of previous investigators.
- The estimated d_{32} values from different models for the terminal rise velocity of single bubbles, as well as those accounting for the crowding effect, were quite close under the examined range of this investigation.

- The estimated BSD encountered in the sparger region and along the column closely fit a log-normal distribution, particularly in slowly coalescent systems. This is in line with the findings of most investigators
- The estimated BSD confirms the flow regimes analysis from the gas holdup results obtained in the whole column.

Finally, the estimated BSD and its computed parameters obtained in this investigation can explain the impact of varying the sparger operating conditions (pressure drop across the sparger, superficial gas velocities, G/L ratio, surfactant concentration). The impact of operating under different flow regimes (true-homogeneous vs pseudo-homogeneous) was found to be reflected in the estimated interfacial areas encountered under those conditions.

REFERENCES

Acuña, C. A., & Finch, J. A. (2010). Tracking velocity of multiple bubbles in a swarm. *International Journal of Mineral Processing, 94*(3–4), 147–158. doi: 10.1016/j.minpro.2010.02.001

Adetunji, O.C.& Rawatlal, R. (2017). Estimation of Bubble Column Hydrodynamics: Image-Based Measurement Method. *Flow Measurement and Instrumentation. 53*, 4–17. doi: 10.1016/j.flowmeasinst.2016.08.002

Adetunji, O.C.& Rawatlal, R. (2018). Prediction of bubble size and axial position distribution through hybridization of population balance modelling and dynamic gas disengagement. *Flow Measurement and Instrumentation. 59*, 181–193. doi: 10.1016/j.flowmeasinst.2017.12.016

Alderliesten, M. (2005). Mean particle diameters. From statistical definition to physical understanding. Journal of Biopharmaceutical Statistics, 15(2), 295–325. doi: 10.1081/BIP-200048774Al Taweel, A.M., Luo, J., Wang, J. (2003). Dynamic Spargers: A Novel Approach to Intensifying Gas/Liquid Contacting Operations. *Proc. of the 5th Intern. Conf. Process Intensification*, 91–106.

Al-Masry, W. A., Dukkan, A. R. (1997). The role of gas disengagement and surface active agents on hydrodynamic and mass transfer characteristics of airlift reactors. Chemical Engineering Journal, 65(3), 263–271. doi: 10.1016/S1385-8947(97)00033-8

Al Taweel, A.M., Landau, J. (1977). Turbulence modulation in two-phase jets. *International Journal of Multiphase Flow, 3*(4), 341-351. doi: 10.1016/0301-9322(77)90014-3.

Al Taweel, A.M., Ramadan, A.M., Moharam, M.R., El Mofty, S.M., Ityokumbul, M. T. (1996). Effect of Honeycomb Inserts on Axial Mixing in Bubble Columns. *Institution of Chemical Engineers*, *74*, 456–462.

Al Taweel, A. M., Luo, J. J., Wang, J. (2003). Dynamic spargers: a novel approach to intensifying gas/liquid contacting operations. In Proceedings of the 5th International Process Intensification Conference, A. Stankiewicz, Ed., 91–106, BHR, Cranfield, UK.

Alves, S. S., Orvalho, S. P., & Vasconcelos, J. M. T. (2005). Effect of bubble contamination on rise velocity and mass transfer. *Chemical Engineering Science, 60*(1), 1–9. doi: 10.1016/j.ces.2004.07.053

Anastasiou, A. D., Kazakis, N. A., Mouza, A. A., & Paras, S. V. (2010). Effect of organic surfactant additives on gas holdup in the pseudo-homogeneous regime in bubble columns equipped with fine pore sparger. *Chemical Engineering Science, 65*(22), 5872–5880. doi: 10.1016/j.ces.2010.08.011

Anastasiou, A. D., Passos, A. D., & Mouza, A. A. (2013). Bubble columns with fine pore sparger and non-Newtonian liquid phase: Prediction of gas holdup. *Chemical Engineering Science, 98*, 331–338. doi: 10.1016/j.ces.2013.05.006

Aoki, J., Hayashi, K., Hosokawa, S., & Tomiyama, A. (2015). Effects of Surfactants on Mass Transfer from Single Carbon Dioxide Bubbles in Vertical Pipes. *Chemical Engineering and Technology, 38*(11), 1955–1964. doi: 10.1002/ceat.201500063

Babaei, R., Bonakdarpour, B., & Ein-Mozaffari, F. (2015). Analysis of gas phase characteristics and mixing performance in an activated sludge bioreactor using electrical resistance tomography. *Chemical Engineering Journal, 279*, 874–884. doi: 10.1016/j.cej.2015.05.072

Bae, K., Kim, J. Y., Go, K. S., Nho, N. S., Kim, D. J., Bae, J. W., & Lee, D. H. (2021). Effect of distributor type on microbubble dispersion in a pressurized bubble column. *Chemical Engineering Research and Design, 174*, 188–198. doi: 10.1016/j.cherd.2021.08.009

Bando, Y., Yoshimatsu, T., Wang, Y., Yasuda, K., Sugie, T. and Asai, T. (2008). Influence of micro-bubble on ozone-decomposition of excess sludge, *Japanese Journal of Multiphase Flow*, *3*, 51–57. doi: 10.3811/pmfr.3.51

Basha, O. M., & Morsi, B. I. (2018). Novel Approach and Correlation for Bubble Size Distribution in a Slurry Bubble Column Reactor Operating in the Churn-Turbulent Flow Regime. *Industrial and Engineering Chemistry Research*, *57*(16), 5705–5716. doi: 10.1021/acs.iecr.8b00543

Baz-Rodríguez, S.; Aguilar-Corona, A., Soria, A. (2012). Rising Velocity for Single Bubbles in Pure Liquids. *Revista Mexicana de Ingeniería Química, 11*, 269-278. Retrieved from http://www.redalyc.org/articulo.oa?id=62026895006

Behkish, A., Lemoine, R., Sehabiague, L., Oukaci, R., & Morsi, B. I. (2007). Gas holdup and bubble size behavior in a large-scale slurry bubble column reactor operating with an organic liquid under elevated pressures and temperatures. *Chemical Engineering Journal, 128*, 69–84. doi: 10.1016/j.cej.2006.10.016

Behzadi, A., Issa, R. I., & Rusche, H. (2004). Modelling of dispersed bubble and droplet flow at high phase fractions. *Chemical Engineering Science, 59*(4), 759–770. doi: 10.1016/j.ces.2003.11.018

Besagni, G., & Inzoli, F. (2017). The effect of liquid phase properties on bubble column fluid dynamics: Gas holdup, flow regime transition, bubble size distributions and shapes, interfacial areas and foaming phenomena. *Chemical Engineering Science*, *170*, 270–296. doi: 10.1016/j.ces.2017.03.043

Binks, B. P. (2002). Particles as surfactants-similarities and differences. *Current Opinion in Colloid & Interface Science, 7*, 21-41. doi: 10.1016/S1359-0294(02)00008-0

Boyer, C., Duquenne, A.-M.M., Wild, G., 2002. Measuring techniques in gas–liquid and gas–liquid–solid reactors. *Chemical Engineering Science, 57*(16), 3185–3215. doi: 10.1016/S0009-2509(02)00193-8.

Bridge, A., Lapidus, L., Elgin, J., 1964. The Mechanics of Vertical Gas–Liquid Fluidized System. Part I: Countercurrent Flow. *A.I.Ch.E. Journal. 10*(6), 819–826.

Brucato, A., Grisafi, F., & Montante, G. (1998). Particle drag coefficients in turbulent fluids. *Chemical Engineering Science, 53*(18), 3295–3314. doi: 10.1016/S0009-2509(98)00114-6

Buffo, A., Vanni, M., Renze, P., & Marchisio, D. L. (2016). Empirical drag closure for polydisperse gas–liquid systems in bubbly flow regime: Bubble swarm and micro-scale turbulence. *Chemical Engineering Research and Design, 113*, 284–303. doi: 10.1016/j.cherd.2016.08.004

Camarasa, E., Vial, C., Poncin, S., Wild, G., Midoux, N., & Bouillard, J. (1999). Influence of coalescence behaviour of the liquid and of gas sparging on hydrodynamics and bubble characteristics in a bubble column. *Chemical Engineering and Processing: Process Intensification, 38*(4–6), 329–344. doi: 10.1016/S0255-2701(99)00024-0

Chen, Z., Ata, S., & Jameson, G. J. (2015). Breakup and re-formation of bubble clusters in a flotation cell. *Minerals Engineering, 71*, 16–20. doi: 10.1016/j.mineng.2014.11.002

Chesters, A. K. (1991). Modelling of coalescence processes in fluid-liquid dispersions. A review of current understanding. *Chemical Engineering Research and Design*.

Daly, J.G., Patel, S.A. & Bukur, D.B. (1992). Measurement of Gas Holdups and Sauter Mean Bubble Diameters in Bubble Column Reactors by Dynamic Gas Disengagement Method. *Chemical Engineering Science*, *47*, 3647–3654.

Deng, Z.H., Wang, T.F., Zhang, N., Wang, Z.W. (2011). Mass-transfer behaviors in alcohol solutions in an internal-loop airlift reactor of 5-m height. *Industrial & Engineering Chemistry Research, 50*, 11537–11543. doi: 10.1021/ie2001988

Djuve, J., Pugh, R. J., & Sjoblom, J. (2001). Foaming and dynamic surface tension of aqueous polymer/surfactants solutions 1: Ethyl(hydroxyethyl) cellulose and sodium dodecyl sulphate. *Colloids and Surfaces A: Physicochemical and Engineering Aspects, 186*(3), 189–202. doi: 10.1016/S0927-7757(00)00787-1

Duineveld, P. C. (1995). The Rise Velocity and Shape of Bubbles in Pure Water at High Reynolds Number. *Journal of Fluid Mechanics, 292*, 325-332. doi: 10.1017/S0022112095001546

Fei, Q., Guarnieri, M. T., Tao, L., Laurens, L. M. L., Dowe, N., & Pienkos, P. T. (2014). Bioconversion of natural gas to liquid fuel: Opportunities and challenges. *Biotechnology Advances*, *32*(3), 596–614. doi: 10.1016/j.biotechadv.2014.03.011

Foust, A. S. (1980). Principles of unit operations-Appendix B. New York: Wiley.

Fransolet, E., Crine, M., Marchot, P., & Toye, D. (2005). Analysis of gas holdup in bubble columns with non-Newtonian fluid using electrical resistance tomography and dynamic gas disengagement technique. *Chemical Engineering Science, 60*(22), 6118–6123. doi: 10.1016/j.ces.2005.03.046

Garnier, C., Lance, M., & Marié, J. L. (2002). Measurement of local flow characteristics in buoyancy-driven bubbly flow at high void fraction. Experimental *Thermal and Fluid Science, 26*(6–7), 811–815. doi: 10.1016/S0894-1777(02)00198-X

Gemello, L., Plais, C., Augier, F., Cloupet, A., & Marchisio, D. L. (2018). Hydrodynamics and bubble size in bubble columns: Effects of contaminants and spargers. *Chemical Engineering Science*, *184*, 93–102. doi: 10.1016/j.ces.2018.03.043

Gordiychuk, A., Svanera, M., Benini, S., & Poesio, P. (2016). Size distribution and Sauter mean diameter of micro bubbles for a Venturi type bubble generator. *Experimental Thermal and Fluid Science*, *70*, 51–60. doi: 10.1016/j.expthermflusci.2015.08.014

Griffith, P., Wallis, G. (1961). Two Phase Slug Flow. *ASME Transactions. Journal of Heat Transfer,* 83, 307–320.

Guo, K., Wang, T., Yang, G., & Wang, J. (2016). Distinctly different bubble behaviors in a bubble column with pure liquids and alcohol solutions. *Journal of Chemical Technology and Biotechnology, 92*(2), 432–441. doi: 10.1002/jctb.5022

Haapala, A., Honkanen, M., Liimatainen, H., Stoor, T., & Niinimäki, J. (2010). Hydrodynamic drag and rise velocity of microbubbles in papermaking process waters. *Chemical Engineering Journal, 162*(3), 956–964. doi: 10.1016/j.cej.2010.07.001

Hashemi, N., Ein-Mozaffari, F., Upreti, S. R., & Hwang, D. K. (2016). Experimental investigation of the bubble behavior in an aerated coaxial mixing vessel through electrical resistance tomography (ERT). *Chemical Engineering Journal, 289*, 402–412. doi: 10.1016/j.cej.2015.12.077

Hayashi, K., & Tomiyama, A. (2012). Effects of surfactant on terminal velocity of a Taylor bubble in a vertical pipe. *International Journal of Multiphase Flow, 39*, 78–87. doi: 10.1016/j.ijmultiphaseflow.2011.11.001

Hayashi, K., & Tomiyama, A. (2018). Effects of surfactant on lift coefficients of bubbles in linear shear flows. International Journal of Multiphase Flow, 99, 86–93. doi: 10.1016/j.ijmultiphaseflow.2017.10.003

Henry, C. L., Parkinson, L., Ralston, J. R., & Craig, V. S. J. (2008). A mobile gas-water interface in electrolyte solutions. *Journal of Physical Chemistry C, 112*(39), 15094–15097. doi: 10.1021/jp8067969

Hessenkemper, H., Ziegenhein, T., Lucas, D., & Tomiyama, A. (2021). Influence of surfactant contaminations on the lift force of ellipsoidal bubbles in water. International Journal of Multiphase Flow, 145(March), 103833. doi: 10.1016/j.ijmultiphaseflow.2021.103833

Hyndman, C. L., Larachi, F., & Guy, C. (1997). Understanding gas-phase hydrodynamics in bubble columns: A convective model based on kinetic theory. *Chemical Engineering Science, 52*(1), 63–77. doi: 10.1016/S0009-2509(96)00387-9

Idhbeaa, A. O. and Al Taweel, A. M, Leng, R., Ghanem, A. Donaldson, A., and Haelssig J. (2022). Effect of Coalescence Retardation on the Gas Holdup and Flow Regimes Encountered in Microbubble-Aerated Columns. To be submitted for publication to "*Chemical Engineering Research and Design*".

Idhbeaa, A. O. and Al Taweel, A. M, Leng, R., Ghanem, A. Donaldson, A., and Haelssig J. (2022). Effect of Sparger Geometric Configurations on the Gas dispersing performance of Adjustable dual-phase transonic venturi sparger. To be submitted for publication to "*Chemical Engineering Research and Design*".

Ishii, M. & Zuber, N. (1979). Drag Coefficient and Relative Velocity in Bubbly, Droplet or Particulate Flows. *AIChE J. 25*, 843-855.

Jamialahmadi, M., Branch, C. and Muller- Steinhagen, H., 1994. Terminal bubble rise velocity in liquids. *Chemical Engineering Research and Design, 72*, 119-122.

Jang N., Yasin, M., Kang, H., Lee, Y., Park, G. W., Park, S., In Seop, C. (2018). Bubble coalescence suppression driven carbon monoxide (CO)-water mass transfer increase by electrolyte addition in a hollow fiber membrane bioreactor (HFMBR) for microbial CO conversion to ethanol. *Bioresource Technology, 263*, 375–384. doi: 10.1016/j.biortech.2018.05.012

Jarek, E., Warszynski, P., & Krzan, M. (2016). Influence of different electrolytes on bubble motion in ionic surfactants solutions. *Colloids and Surfaces A: Physicochemical and Engineering Aspects, 505*, 171–178. doi: 10.1016/j.colsurfa.2016.03.071

Jhawar, A. K., & Prakash, A. (2014). Bubble column with internals: Effects on hydrodynamics and local heat transfer. *Chemical Engineering Research and Design, 92*(1), 25–33. doi: 10.1016/j.cherd.2013.06.016

Jin, H., Wang, M., & Williams, R. A. (2007). Analysis of bubble behaviors in bubble columns using electrical resistance tomography. *Chemical Engineering Journal, 130*(2–3), 179–185. doi: 10.1016/j.cej.2006.08.032

Jin, H., Lian, Y., Yang, S., He, G., & Guo, Z. (2013). The parameters measurement of air-water two phase flow using the electrical resistance tomography (ERT) technique in a bubble column. *Flow Measurement and Instrumentation, 31*, 55–60. doi: 10.1016/j.flowmeasinst.2012.11.002

Jordan, U., Saxena, A. K., & Schumpe, A. (2008). Dynamic Gas Disengagement in a High-Pressure Bubble Column. *The Canadian Journal of Chemical Engineering, 81*(3–4), 491–498. doi: 10.1002/cjce.5450810322

Karamanev, D. G. (1996). Equations for calculation of the terminal velocity and drag coefficient of solid spheres and gas bubbles. *Chemical Engineering Communications*. doi: 10.1080/00986449608936496

Kawahara, A., Sadatomi, M., Matsuyama, F., Matsuura, H., Tominaga, M., & Noguchi, M. (2009). Prediction of micro-bubble dissolution characteristics in water and seawater. *Experimental Thermal and Fluid Science, 33*(5), 883–894. doi: 10.1016/j.expthermflusci.2009.03.004

Kazakis, N.A.; Mouza, A.A.; Paras, S.V. (208). Experimental study of bubble formation at metal porous spargers: Effect of liquid properties and sparger characteristics on the initial bubble size distribution. *Chem. Eng. J. 137*, 265–281. doi: 10.1016/j.cej.2007.04.040

Kazemzadeh, A., Elias, C., Tamer, M., & Ein-Mozaffari, F. (2018). Hydrodynamic performance of a single-use aerated stirred bioreactor in animal cell culture: applications of tomography, dynamic gas disengagement (DGD), and CFD. *Bioprocess and Biosystems Engineering, 41*(5), 679–695. doi: 10.1007/s00449-018-1902-7

Kelsall, G. H., Tang, S., Smith, A. L., & Yurdakul, S. (1996). Measurement of rise and electrophoretic velocities of gas bubbles. *Journal of the Chemical Society - Faraday Transactions, 92*(20), 3879–3885. doi: 10.1039/ft9969203879

Khalili, F., Jafari Nasr, M. R., Kazemzadeh, A., & Ein-Mozaffari, F. (2018). Analysis of gas holdup and bubble behavior in a biopolymer solution inside a bioreactor using tomography and dynamic gas disengagement techniques. Journal of *Chemical Technology and Biotechnology, 93*(2), 340–349. doi: 10.1002/jctb.5356

Kong, G., Mirsandi, H., Buist, K. A., Peters, E. A. J. F., Baltussen, M. W., & Kuipers, J. A. M. (2019). Hydrodynamic interaction of bubbles rising side-by-side in viscous liquids. *Experiments in Fluids, 60*(10), 1–15. doi: 10.1007/s00348-019-2798-y

Krishna, R., De Swart, J. W. A., Ellenberger, J., Martina, G. B., & Maretto, C. (1997). Gas Holdup in Slurry Bubble Columns: Effect of Column Diameter and Slurry Concentrations. *AIChE Journal, 43*(2), 311–316. doi: 10.1002/aic.690430204

Krishna, R., Van Baten, J. M., Urseanu, M. I., & Ellenberger, J. (2001). Design and scale up of a bubble column slurry reactor for Fischer-Tropsch synthesis. *Chemical Engineering Science, 56*(2), 537–545. doi: 10.1016/S0009-2509(00)00258-X

Krzan, M., & Malysa, K. (2012). Influence of electrolyte presence on bubble motion in solutions of sodium n-alkylsulfates (C8, C10, C12). *Physicochemical Problems of Mineral Processing, 48*(1), 49–62.

Kugou, N., Ishida, K., & Yoshida, A. (2003). Experimental study on motion of air bubbles in seawater (terminal velocity and drug coefficient of air bubble rising in seawater). *WIT Transactions on the Built Environment, 68*(3), 145–158.

Lane, C. D., Parisien, V., Macchi, A., & Donaldson, A. A. (2016). Investigation of bubble swarm drag at elevated pressure in a contaminated system. *Chemical Engineering Science, 152*, 381–391. doi: 10.1016/j.ces.2016.06.017

Lee, D. J., Luo, X., & Fan, L. S. (1999). Gas disengagement technique in a slurry bubble column operated in the coalesced bubble regime. *Chemical Engineering Science, 54*(13–14), 2227–2236. doi: 10.1016/S0009-2509(98)00389-3

Leifer, I., Patro, R. K., & Bowyer, P. (2000). A study on the temperature variation of rise velocity for large clean bubbles. *Journal of Atmospheric and Oceanic Technology, 17*(10), 1392–1402. doi: 10.1175/1520-0426(2000)017<1392:ASOTTV>2.0.CO;2

Lemoine, R., Behkish, A., & Morsi, B. I. (2004). Hydrodynamic and mass-transfer characteristics in organic liquid mixtures in a large-scale bubble column reactor for the toluene oxidation process. *Industrial and Engineering Chemistry Research, 43*(19), 6195–6212. doi: 10.1021/ie0400797

Li, W., Zhong, W., Jin, B., Xiao, R., Lu, Y., He, T. (2013). Study of the Particle Size Effect on Bubble Rise Velocities in a Three-Phase Bubble Column. *World Academy of Science, Engineering and Technology International Journal of Chemical and Molecular Engineering. 7*(12), 971-975.

Li, J., Song, Y., Yin, J., & Wang, D. (2017). Investigation on the effect of geometrical parameters on the performance of a venturi type bubble generator. *Nuclear Engineering and Design, 325*, 90–96. doi: 10.1016/j.nucengdes.2017.10.006

Lim, D. H., Park, J. H., Kang, Y., & Jun, K. W. (2013). Structure of bubble holdups in a viscous slurry bubble column with low surface tension media. *Fuel Processing Technology, 108*, 2–7. doi: 10.1016/j.fuproc.2012.06.024

Liu, B., Manica, R., Liu, Q., Klaseboer, E., Xu, Z., & Xie, G. (2019). Coalescence of bubbles with mobile interfaces in water. *Physical Review Letters, 122*(19), 194501. doi: 10.1103/PhysRevLett.122.194501

Liu, L., Yan, H., Zhao, G., & Zhuang, J. (2016). Experimental studies on the terminal velocity of air bubbles in water and glycerol aqueous solution. *Experimental Thermal and Fluid Science, 78*, 254–265. doi: 10.1016/j.expthermflusci.2016.06.011

Lockett, M.J., Kirkpatrick, R.D. (1975). Ideal bubbly flow and actual flow in bubble columns. *Trans. Inst. Chem. Eng.*, 53.

Loisy, A. & Naso, A. (2017). Interaction between a large buoyant bubble and turbulence. *Physical Review Fluids, 2*, 014606. doi: 10.1103/PhysRevFluids.2.014606

Luna-Brito, M. J., Sacramento-Rivero, J. C., & Baz-Rodríguez, S. A. (2018). Effects of Medium Composition and Gas Superficial Velocity on Mass Transfer during Microalgae Culturing in a Bubble Column Photobioreactor. *Industrial and Engineering Chemistry Research*, *57*(50), 17058–17063. doi: 10.1021/acs.iecr.8b03940

Luo, H., Hjarbo, K., Svendsen, H. (1996). Bubble size and gas holdup structure in bubble column by dynamic gas disengagement. *Chinese Journal of Chemical Engineering. 4*(2), 150-161.

Luo J. (2002). *Bubble dispersion and coalescence in turbulent pipe flow* (Doctoral Dissertation). Dalhousie University, Canada.

Marrucci, G. (1965). Rising velocity of swarm of spherical bubbles. *Industrial and Engineering Chemistry Fundamentals, 4*(2), 224–225. doi: 10.1021/i160014a022

Martnez Mercado, J., Chehata Gmez, D., Van Gils, D., Sun, C., & Lohse, D. (2010). On bubble clustering and energy spectra in pseudo-turbulence. *Journal of Fluid Mechanics, 650*, 287–306. doi: 10.1017/S0022112009993570

McClure, D. D., Wang, C., Kavanagh, J. M., Fletcher, D. F., & Barton, G. W. (2016). Experimental investigation into the impact of sparger design on bubble columns at high superficial velocities. Chemical Engineering Research and Design, 106, 205–213. doi: 10.1016/j.cherd.2015.12.027

McClure, D. D., Kavanagh, J. M., Fletcher, D. F., & Barton, G. W. (2017). Experimental investigation into the drag volume fraction correction term for gas-liquid bubbly flows. *Chemical Engineering Science, 170*, 91–97. doi: 10.1016/j.ces.2016.12.066

McKenna, S. P., & McGillis, W. R. (2004). The role of free-surface turbulence and surfactants in air-water gas transfer. *International Journal of Heat and Mass Transfer, 47*(3), 539–553. doi: 10.1016/j.ijheatmasstransfer.2003.06.001

Mehrabadi, A.A.R. (2009). *Effects of Frother Type on Single Bubble Rise Velocity*. McGill University, Montreal, Canada.

Mikkilineni, S., Koelle, M., & Xu, H. (1997). Measurement of dynamic gas disengagement profile by using an analog output level gauge. *Experiments in Fluids, 22*(3), 249–250. doi: 10.1007/s003480050043

Moilanen, P., Laakkonen, M., & Aittamaa, J. (2006). Modeling aerated fermenters with computational fluid dynamics. *Industrial and Engineering Chemistry Research, 45*(25), 8656–8663. doi: 10.1021/ie060097j

Moraveji, M. K., Pasand, M. M., Davarnejad, R., Chisti, Y. (2012). Effects of surfactants on hydrodynamics and mass transfer in a split-cylinder airlift reactor. The Canadian Journal of Chemical Engineering, 90(1), 93–99. doi: 10.1002/cjce.20516

Mouza, A. A., Dalakoglou, G. K., & Paras, S. V. (2005). Effect of liquid properties on the performance of bubble column reactors with fine pore spargers. *Chemical Engineering Science, 60*(5), 1465–1475. doi: 10.1016/j.ces.2004.10.013

Möller, F., Kipping, R., Lavetty, C., Hampel, U., & Schubert, M. (2019). Two-Bubble Class Approach Based on Measured Bubble Size Distribution for Bubble Columns with and without Internals. *Industrial and Engineering Chemistry Research*, *58*(8), 2759–2769. doi: 10.1021/acs.iecr.8b05784

Muroyama, K., Imai, K., Oka, Y., & Hayashi, J. (2013). Mass transfer properties in a bubble column associated with micro-bubble dispersions. *Chemical Engineering Science, 100*, 464–473. doi: 10.1016/j.ces.2013.03.043

Nedeltchev, S., Hampel, U., & Schubert, M. (2016). Investigation of the radial effect on the transition velocities in a bubble column based on the modified Shannon entropy. *Chemical Engineering Research and Design*, *115*, 303–309. doi: 10.1016/j.cherd.2016.08.011

Nedeltchev, S. (2020). Precise identification of the end of the gas maldistribution in bubble columns equipped with perforated plate gas distributors. *Chemical Engineering Journal, 386*(April 2019), 121535. doi: 10.1016/j.cej.2019.04.115

Ng, S., Warszyński, P., Zembala, M., Małysa, K. (1999). Composition of Bitumen-Air Aggregates Floating to Froth Layer During Processing of Two Different Oil Sands. *Physicochem. Probl. Miner. Process, 33*(1):143–166.

Nguyen, A. V. (1998). Prediction of Bubble Terminal Velocities in Contaminated Water. *AIChE Journal, 44*(1), 226–230. doi: 10.1002/aic.690440124

Nüllig, M., & Peters, F. (2018). Experiments on the transition of fast to slow bubbles in water. *Chemical Engineering Science, 175*, 91–97. doi: 10.1016/j.ces.2017.09.047

Ohde, D., Thomas, B., Matthes, S., Tanaka, S., Bubenheim, P., Terasaka, K., … Liese, A. (2021). Microbubble enhanced mass transfer efficiency of CO2capture utilizing aqueous triethanolamine for enzymatic resorcinol carboxylation. *RSC Advances, 11*(7), 4087–4096. doi: 10.1039/d0ra08690h

Okawa, T., Tanaka, T., Kataoka, I., & Mori, M. (2003). Temperature effect on single bubble rise characteristics in stagnant distilled water. *International Journal of Heat and Mass Transfer, 46*(5), 903–913. doi: 10.1016/S0017-9310(02)00345-9

Okazaki, S. (1964). The Velocity of Ascending Air Bubbles in Aqueous Solutions of a Surface Active Substance and the Life of the Bubble on the Same Solution. *Bulletin of the Chemical Society of Japan, 37*(2), 144–150. doi: 10.1246/bcsj.37.144

Pallapothu, S. K., & Al Taweel, A. M. (2012). Effect of contaminants on the gas holdup and mixing in internal airlift reactors equipped with microbubble generator. *International Journal of Chemical Engineering*, *2012*. doi: 10.1155/2012/569463

Pallapothu, S.K. (2006). Oxygen Transfer in Airlift Reactors Equipped with a High-Performance Sparger. M.A.Sc. Thesis, Department of Process Engineering and Applied Science, Dalhousie University.

Parthasarathy, R., Ahmed, N. (1996). Size distribution of bubbles generated by fine-pore spargers, J*. Chem. Eng. Jpn. 29* (6), 1030–1034.

Passos, A. D., Voulgaropoulos, V. P., Paras, S. V., & Mouza, A. A. (2015). The effect of surfactant addition on the performance of a bubble column containing a non-Newtonian liquid. *Chemical Engineering Research and Design, 95,* 93–104. doi: 10.1016/j.cherd.2015.01.008

Parisien, V., Farrell, A., Pjontek, D., McKnight, C. A., Wiens, J., & Macchi, A. (2017). Bubble swarm characteristics in a bubble column under high gas holdup conditions. *Chemical Engineering Science, 157*, 88–98. doi: 10.1016/j.ces.2016.04.051

Parkinson, L., Sedev, R., Fornasiero, D., & Ralston, J. (2008). The terminal rise velocity of 10-100 μm diameter bubbles in water. *Journal of Colloid and Interface Science, 322*(1), 168–172. doi: 10.1016/j.jcis.2008.02.072

Parmar, R. & Majumder, S. K. (2015). Terminal rise velocity, size distribution and stability of microbubble suspension. *Asia-Pacific Journal of Chemical Engineering Asia-Pac,10,* 450–465. doi: 10.1002/apj.1891

Patel, S.A., Daly, J.G., & Bukur, D.B. (1989). Holdup and Interficial Area Measurements Using Dynamic Gas Disengagement. *AIChE Journal. 35*(6), 931-942.

Pereira, R., Ashton, I., Sabbaghzadeh, B., Shutler, J. D., & Upstill-Goddard, R. C. (2018). Reduced air-sea CO_2 exchange in the Atlantic Ocean due to biological surfactants. *Nature Geoscience, 11*(7), 492–496. doi: 10.1038/s41561-018-0136-2

Prakash, R., Kumar Majumder, S., & Singh, A. (2020). Bubble size distribution and specific bubble interfacial area in two–phase microstructured dense bubbling bed. *Chemical Engineering Research and Design, 156*, 108–130. doi: 10.1016/j.cherd.2020.01.032

Ramírez-Muñoz, J., Galicia-Nequiz, O. G., Baz-Rodríguez, S., Colín-Luna, J. A., Martínez-Delgadillo, S. A., & Puebla, H. (2012). The effects of surfactants on the drag of a bubble. *Procedia Engineering, 42*, 1840–1848. doi: 10.1016/j.proeng.2012.07.579

Richardson, J., Zaki, W. (1954). Sedimentation and fluidisation: part I. *Transactions of the Institution of Chemical Engineers*, 32, 35–53.

Rivas-Interián, R. M., Guillén-Francisco, J. A., Sacramento-Rivero, J. C., Zitlalpopoca-Soriano, Á. G., & Baz-Rodríguez, S. A. (2019). Concentration effects of main components of synthetic culture media on oxygen transfer in bubble column bioreactors. *Biochemical Engineering Journal, 143*, 131–140. doi: 10.1016/j.bej.2018.12.008

Rodrigo Velez-Cordero J., Johanna Lantenet, Juan Hernandez-Cordero, and Roberto Zenit (2014), Compact bubble clusters in Newtonian and non-Newtonian liquids. *Phys. Fluids, 26*, 053101. doi: 10.1063/1.4874630

Roghair, I., Lau, Y. M., Deen, N. G., Slagter, H. M., Baltussen, M. W., Van Sint Annaland, M., & Kuipers, J. A. M. (2011). On the drag force of bubbles in bubble swarms at intermediate and high Reynolds numbers. *Chemical Engineering Science, 66*(14), 3204–3211. doi: 10.1016/j.ces.2011.02.030

Roghair, I., Van Sint Annaland, M. and Kuipers, H.J.A.M. (2013). Drag force and clustering in bubble swarms. *AIChE J, 59*: 1791-1800. doi: 10.1002/aic.13949

Takagi, S., & Matsumoto, Y. (2011). Surfactant effects on bubble motion and bubbly flows. *Annual Review of Fluid Mechanics, 43*, 615–636. doi: 10.1146/annurev-fluid-122109-160756

Rollbusch, P., Bothe, M., Becker, M., Ludwig, M., Grünewald, M., Schlüter, M., & Franke, R. (2015). Bubble columns operated under industrially relevant conditions - Current understanding of design parameters. *Chemical Engineering Science*, *126*, 660–678. doi: 10.1016/j.ces.2014.11.061

Rosso, D., Iranpour, R., & Stenstrom, M. K. (2005). Fifteen Years of Offgas Transfer Efficiency Measurements on Fine-Pore Aerators: Key Role of Sludge Age and Normalized Air Flux. *Water Environment Research*, *77*(3), 266–273. doi: 10.2175/106143005x41843

Rulyov, N., Nessipbay, T., Dulatbek, T., Larissa, S., & Zhamikhan, K. (2018). Effect of microbubbles as flotation carriers on fine sulphide ore beneficiation. *Mineral Processing and Extractive Metallurgy: Transactions of the Institute of Mining and Metallurgy, 127*(3), 133–139. doi: 10.1080/03719553.2017.1351067

Sanada, T., Sugihara, K., Shirota, M., & Watanabe, M. (2008). Motion and drag of a single bubble in super-purified water. *Fluid Dynamics Research, 40*(7–8), 534–545. doi: 10.1016/j.fluiddyn.2007.12.005

Scargiali, F., D'Orazio, A., Grisafi, F., & Brucato, A. (2007). Modelling and simulation of gas - Liquid hydrodynamics in mechanically stirred tanks. *Chemical Engineering Research and Design, 85*(5A), 637–646. doi: 10.1205/cherd06243

Schiller, L. and Naumann, A. (1935), A drag coefficient correlation. *Zeitschrift des Vereins Deutscher Ingenieure, 77*, 318–320.

Schrimpf, M., Esteban, J., Rösler, T., Vorholt, A. J., & Leitner, W. (2019). Intensified reactors for gas-liquid-liquid multiphase catalysis: From chemistry to engineering. *Chemical Engineering Journal*, *372*, 917–939. doi: 10.1016/j.cej.2019.03.133

Schumpe, A. & Grund, G. (1986). The Gas Disengagement Technique for Studying Gas Holdup Structure in Bubble Columns. *The Canadian Journal of Chemical Engineering, 64*, 891–896.

Shi, P., Rzehak, R., Lucas, D., & Magnaudet, J. (2020). Hydrodynamic forces on a clean spherical bubble translating in a wall-bounded linear shear flow. *Physical Review Fluids, 5*(7). doi: 10.1103/PhysRevFluids.5.073601

Simonnet, M., Gentric, C., Olmos, E., & Midoux, N. (2007). Experimental determination of the drag coefficient in a swarm of bubbles. *Chemical Engineering Science, 62*(3), 858–866. doi: 10.1016/j.ces.2006.10.012

Simonnet, M., Gentric, C., Olmos, E., & Midoux, N. (2008). CFD simulation of the flow field in a bubble column reactor: Importance of the drag force formulation to describe regime transitions. *Chemical Engineering and Processing: Process Intensification, 47*(9–10), 1726–1737. doi: 10.1016/j.cep.2007.08.015

Sriram, K., Mann, R. (1977). Dynamic gas disengagement: a new technique for assessing the behaviour of bubble columns. *Chemical Engineering Science*, *32*, 571–580. doi: 10.1016/0009-2509(77)80222-4

Stokes G.G. (1851). On the Effect of the Internal Friction of Fluids on the Motion of Pendulums. *Cambridge Philos. Trans. 9*, 8 –106.

Takagi, S., & Matsumoto, Y. (2011). Surfactant effects on bubble motion and bubbly flows. *Annual Review of Fluid Mechanics, 43*, 615–636. doi:10.1146/annurev-fluid-122109-160756

Takahashi, M. (2005). ζ Potential of microbubbles in aqueous solutions: Electrical properties of the gas - Water interface. *Journal of Physical Chemistry B, 109*(46), 21858–21864. doi: 10.1021/jp0445270

Tanaka, S., Kastens, S., Fujioka, S., Schlüter, M., & Terasaka, K. (2019). Mass transfer from freely rising microbubbles in aqueous solutions of surfactant or salt. *Chemical Engineering Journal,* 1–10. doi: 10.1016/j.cej.2019.03.122

Tao, F., Ning, S., Zhang, B., Jin, H., & He, G. (2019). Simulation study on gas holdup of large and small bubbles in a high pressure gas-liquid bubble column. *Processes, 7*(9). doi: 10.3390/pr7090594

Terasaka, K., Hirabayashi, A., Nishino, T., Fujioka, S., & Kobayashi, D. (2011). Development of microbubble aerator for waste water treatment using aerobic activated sludge. *Chemical Engineering Science, 66*(14), 3172–3179. doi: 10.1016/j.ces.2011.02.043

Tomiyama, A. Kataoka, I., Zun, I., Sakaguchi, T. (1998). Drag coefficients of single bubbles under normal and micro gravity conditions. *JSME International Journal Series B, 41*(2), 472–479. doi: 10.1299/jsmeb.41.472

Urseanu, M. I. (2000). Scaling up bubble column reactors. *UvA-DARE (Digital Academic Repository). University of Amsterdam.*

Vadlakonda, B., & Mangadoddy, N. (2017). Hydrodynamic study of two phase flow of column flotation using electrical resistance tomography and pressure probe techniques. *Separation and Purification Technology, 184*, 168–187. doi: 10.1016/j.seppur.2017.04.029

Vasconcelos, J. M. T., Orvalho, S. P., & Alves, S. S. (2002). Gas-liquid mass transfer to single bubbles: Effect of surface contamination. *AIChE Journal, 48*(6), 1145–1154. doi: 10.1002/aic.690480603

Vermeer, D. J., & Krishna, R. (1981). Hydrodynamics and Mass Transfer in Bubble Columns Operating in the Churn-Turbulent Regime. *Industrial and Engineering Chemistry Process Design and Development, 20*, 475–482. doi: 10.1021/i200014a014

Wu, M., & Gharib, M. (2002). Experimental studies on the shape and path of small air bubbles rising in clean water. *Physics of Fluids, 14*(7). doi: 10.1063/1.1485767

Xing, C., Wang, T., & Wang, J. (2013). Experimental study and numerical simulation with a coupled CFD-PBM model of the effect of liquid viscosity in a bubble column. *Chemical Engineering Science, 95*, 313–322. doi: 10.1016/j.ces.2013.03.022

Yan, X., Zheng, K., Jia, Y., Miao, Z., Wang, L., Cao, Y., & Liu, J. (2018). Drag Coefficient Prediction of a Single Bubble Rising in Liquids. *Industrial and Engineering Chemistry Research, 57*(15), 5385–5393. doi: 10.1021/acs.iecr.7b04743

Yang, J. H., Yang, J. Il, Kim, H. J., Chun, D. H., Lee, H. T., & Jung, H. (2010). Two regime transitions to pseudo-homogeneous and heterogeneous bubble flow for various liquid viscosities. *Chemical Engineering and Processing: Process Intensification, 49*(10), 1044–1050. doi: 10.1016/j.cep.2010.07.015

Yao, K., Chi, Y., Wang, F., Yan, J., Ni, M., & Cen, K. (2016). The effect of microbubbles on gas-liquid mass transfer coefficient and degradation rate of COD in wastewater treatment. *Water Science and Technology, 73*(8), 1969–1977. doi: 10.2166/wst.2016.018

Yasin, M., Ketema, T., & Bacha, K. (2015). Physico-chemical and bacteriological quality of drinking water of different sources, Jimma zone, Southwest Ethiopia. *BMC Research Notes, 8*(1), 1–13. doi: 10.1186/s13104-015-1376-5

Zawala, J., Kosior, D., & Malysa, K. (2015). Formation and influence of the dynamic adsorption layer on kinetics of the rising bubble collisions with solution/gas and solution/solid interfaces. *Advances in Colloid and Interface Science, 222*, 765–778. doi: 10.1016/j.cis.2014.07.013

Zhang, L. juan, Li, T., Ying, W. yong, & Fang, D. ye. (2008). Rising and descending bubble size distributions in gas-liquid and gas-liquid-solid slurry bubble column reactor. *Chemical Engineering Research and Design, 86*(10), 1143–1154. doi: 10.1016/j.cherd.2008.04.006

Zhou, J. Z., Li, H., Chow, R. S., Liu, Q., Xu, Z., & Masliyah, J. (2020). Role of mineral flotation technology in improving bitumen extraction from mined Athabasca oil sands—II. Flotation hydrodynamics of water-based oil sand extraction. *Canadian Journal of Chemical Engineering, 98*(1), 330–352. doi: 10.1002/cjce.23598

Ziegenhein, T., & Lucas, D. (2017). Observations on bubble shapes in bubble columns under different flow conditions. *Experimental Thermal and Fluid Science, 85*, 248–256. doi: 10.1016/j.expthermflusci.2017.03.00

APPENDIX A Calculations of Sparger Parameters

A physical expression of the ADPV sparger is depicted in Figure A.1. The cross-sectional area of the throat can be adjusted by turning the inner core. When the inner core is screwed one turn, the distance of its movement is 1 mm. With the movement of the inner core, the gap between the outer shell and the inner core is changed. The gap between the outer shell and inner core from the throat entrance (location 2) to throat exit (location 3) can be described as:

$$D_{Gap2\rightarrow3} = Turns * 0.001 * \tan 3° * 2 \qquad \text{(A.1)}$$

The gap between the outer shell and inner core from throat exit to sparger exit (locations 3 to 4) will be discussed in A.1.4.

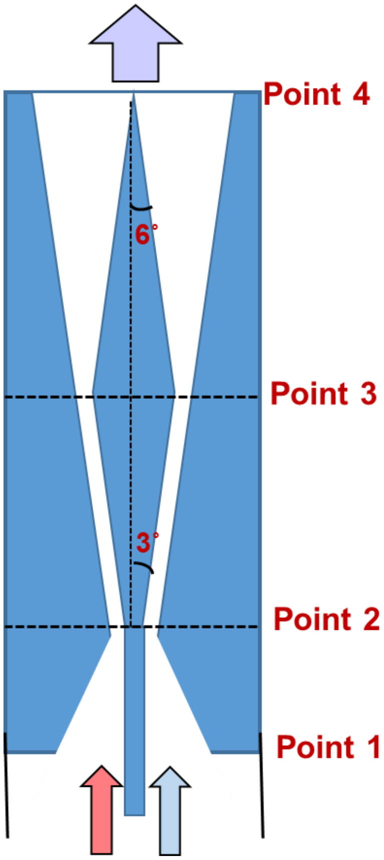

Figure A.1 Physical Expression of Sparger.

There are two equivalent diameters of the throat; one is geometric equivalent diameter, which is based on the geometry of the design and is used for calculating CSAs in the sparger. The other is the hydraulic equivalent diameter, which is used to calculate the parameters related to two-phase flows, such as Reynolds number.

A.1 Geometric Equivalent Diameter

A.1.1 Calculations at Throat Exit

The largest diameter of the inner core is represented by D_{InCo_3}. Thus, the throat geometric equivalent diameter at throat exit (location 3) can be described by:

$$D_{Sp3Geo} = \sqrt{\left(D_{InCo3} + D_{Gap2\to3}\right)^2 - D_{InCo3}{}^2} \tag{A.2}$$

Since the geometric equivalent diameter at the throat exit is known. The cross-sectional areas at this location can be expressed as:

$$A_{Sp3} = \frac{\pi}{4} * D_{Sp3Geo}{}^2$$

A.1.2 Calculations at Throat Entrance

The diameter of the inner core at the throat entrance (location 2) is represented as D_{InCo_2}. the geometric equivalent diameter of the throat at throat entrance can be described by:

$$D_{Sp2Geo} = \sqrt{\left(D_{InCo2} + D_{Gap2\to3}\right)^2 - D_{InCo2}{}^2} \tag{A.3}$$

The cross-sectional areas at the throat entrance can be described by:

$$A_{Sp2} = \frac{\pi}{4} * D_{Sp2Geo}{}^2 \tag{A.4}$$

A.1.3 Calculations at Any Specified Location between Throat Entrance and Throat Exit

The distance from any specified location between throat entrance and throat exit is expressed by $H_{SpecLoc \to 3}$. Any diameter of the inner core between throat entrance and throat exit can be described as:

$$D_{InCoSpecLoc2 \to 3} = D_{InCo3} - 2 * H_{SpecLoc \to Sp3} * \tan 3° \quad \text{(A.5)}$$

So, the geometric equivalent diameter of the throat at this specified location can be described by:

$$D_{SpecLoc2 \to 3Geo} = \sqrt{\left(D_{InCoSpecLoc2 \to 3} + D_{Gap2 \to 3}\right)^2 - {D_{InCoSpecLoc2 \to 3}}^2} \quad \text{(A.6)}$$

Then, the cross-sectional areas at any specified location between throat entrance and throat exit can be described as:

$$A_{SpecLoc2 \to 3} = \frac{\pi}{4} * {D_{SpecLoc2 \to 3Geo}}^2 \quad \text{(A.7)}$$

A.1.4 Calculations at Any Specified Location between Throat Exit and Sparger Exit

The distance from the throat exit to any specified location between the throat exit and the sparger exit is expressed by $H_{3 \to SpecLoc}$. Any diameter of the inner core between the throat exit and the sparger exit can be described as:

$$D_{InCoSpecLoc3 \to 4} = D_{InCo3} - 2 * H_{Sp3 \to SpecLoc} * \tan 6° \quad \text{(A.8)}$$

The gap between the outer shell and inner core from the throat exit to the sparger exit can be described by:

$$D_{Gap3 \to 4} = D_{Gap2 \to 3} + 2 * H_{Sp3 \to SpecLoc} * (\tan 6° + \tan 3°) \quad \text{(A.9)}$$

So, the geometric equivalent diameter of the throat at this specified location can be described by:

$$D_{SpecLoc3\rightarrow 4Geo} = \sqrt{\left(D_{InCoSpecLoc3\rightarrow 4} + D_{Gap3\rightarrow 4}\right)^2 - D_{InCoSpecLoc3\rightarrow 4}{}^2} \quad \text{(A.10)}$$

Then, the cross-sectional areas at any specified location between the throat exit and the sparger exit can be described as:

$$A_{SpecLoc3\rightarrow 4} = \frac{\pi}{4} * D_{SpecLoc3\rightarrow 4Geo}{}^2 \quad \text{(A.11)}$$

A.2 Hydraulic Equivalent Diameter

A.2.1 Calculations at Any Specified Location between Throat Entrance and Throat Exit

Hydraulic equivalent diameter at any specified location from the throat entrance to the throat exit can be expressed as:

$$\begin{aligned} &D_{Hd_{SpecLoc2\rightarrow 3}} \\ &= 4 * \frac{A_{SpecLoc2\rightarrow 3}}{\pi\left(D_{InCoSpecLoc2\rightarrow 3} + D_{Gap2\rightarrow 3} + D_{InCoSpecLoc2\rightarrow 3}\right)} \\ &= 4 * \frac{\frac{\pi}{4} * \left[\left(D_{InCoSpecLoc2\rightarrow 3} + D_{Gap2\rightarrow 3}\right)^2 - D_{InCoSpecLoc2\rightarrow 3}{}^2\right]}{\pi\left(D_{InCoSpecLoc2\rightarrow 3} + D_{Gap2\rightarrow 3} + D_{InCoSpecLoc2\rightarrow 3}\right)} \\ &= D_{Gap2\rightarrow 3} \end{aligned} \quad \text{(A.12)}$$

A.2.2 Calculations at Any Specified Location between Throat Exit and Sparger Exit

Hydraulic equivalent diameter at any specified location from the throat exit to the sparger exit can be expressed as:

$$\begin{aligned} D_{Hd_{SpecLoc3\rightarrow 4}} &= 4 * \frac{A_{SpecLoc3\rightarrow 4}}{\pi\left(D_{InCoSpecLoc3\rightarrow 4} + D_{Gap3\rightarrow 4} + D_{InCoSpecLoc3\rightarrow 4}\right)} \\ &= D_{Gap3\rightarrow 4} \end{aligned} \quad \text{(A.13)}$$

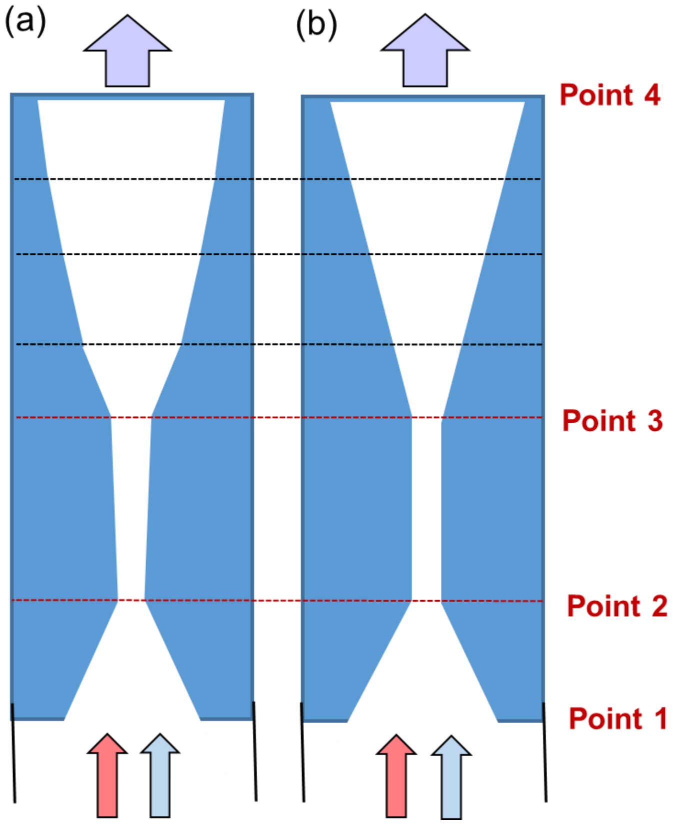

Figure A.2 Equivalent geometry of the sparger modified from Figure A.1 using (a) geometric equivalent diameters, (b) hydraulic equivalent diameters.

A.3 Volume of the Active Part of the ADPV sparger

The equivalent geometry of the throat area (from throat entrance to throat exit, as seen in Figure A.2a) can be considered as a truncated cone. Thus, the volume of the throat can be obtained by:

$$V_{Th} = \frac{1}{3} \cdot H_{Th} \cdot \left(\frac{A_{Sp2}}{4} + \frac{A_{Sp3}}{4} + \pi * {D_{Sp2Geo}}^{2} * {D_{Sp3Geo}}^{2}\right) \qquad \text{(A.14)}$$

As seen in Figure A.2a, the geometry between the throat exit and the sparger exit is not a straight line, so the equivalent geometry of the divergent section using geometric equivalent diameters cannot be considered as a truncated cone, and thus cannot be calculated simply using the equation of a truncated cone. From the physical expression of the sparger shown Figure A.1, the volume of the divergent section should be equal to the volume of the outer shell in this section minus the inner cone, which is described as:

$$V_{Dv} = V_{OuSh_{Dv}} - V_{InCo_{Dv}} \tag{A.15}$$

The length and height from the throat entrance to the sparger exit are 0.09413 m and 0.094 m, respectively. The total length and height of the divergent section, at which the sparger is fully closed, can be expressed as:

$$L_{TL_{Dv}} = 0.09413 - L_{Th} \tag{A.16}$$

$$H_{TL_{Dv}} = 0.094 - H_{Th} \tag{A.17}$$

As we know, the core nozzle will move up 1 mm of height when the sparger is opened for one turn. Thus, the divergence length and height, which are changing with the opening of the sparger, can be obtained as:

$$L_{Dv} = L_{TL_{Dv}} - (Turns * 0.001)/\cos 3° \tag{A.18}$$

$$H_{Dv} = H_{TL_{Dv}} - Turns * 0.001 \tag{A.19}$$

The cross-sectional area of the outer shell at the throat exit (location 3) can be obtained by:

$$A_{OuSh3} = \frac{\pi}{4} * \left(D_{InCo3} + D_{Gap2\to 3}\right)^2 \tag{A.20}$$

The cross-sectional area of the sparger at the sparger exit (location 4) can be described as:

$$A_{Sp4} = \frac{\pi}{4} * {D_{Sp4}}^2 \tag{A.21}$$

The total volume of the outer shell (including the inner core), which changes with the movement of the inner core, can be calculated by:

$$V_{OuSh_{Dv}} = \frac{1}{3} \cdot H_{Dv} \cdot \left(\frac{A_{OuSh3}}{4} + \frac{A_{Sp4}}{4} + \pi * \left(D_{InCo3} + D_{Gap2\rightarrow 3} \right)^2 * D_{Sp4}{}^2 \right) \quad \text{(A.22)}$$

The inner core at the divergent section is a cone. The height of the inner core from the throat exit to the sparger exit is 0.073 m. The cross-sectional area of the inner core at the point of the throat exit (location 3) can be calculated as:

$$A_{InCo3} = \frac{\pi}{4} * D_{InCo3}{}^2 \quad \text{(A.23)}$$

Therefore, the volume of the inner core (cone part) can be expressed as:

$$V_{InCo_{Dv}} = \frac{1}{3} * A_{InCo3} * 0.073 \quad \text{(A.24)}$$

Since the sparger is mainly constituted by the throat section and the divergent section after it, the total volume of the sparger is equal to the sum of these two sections, which can be expressed as:

$$V_{Sp} = V_{Th} + V_{Dv} \quad \text{(A.25)}$$

APPENDIX B Typical Example of the Input Data Sheet for A Typical Run

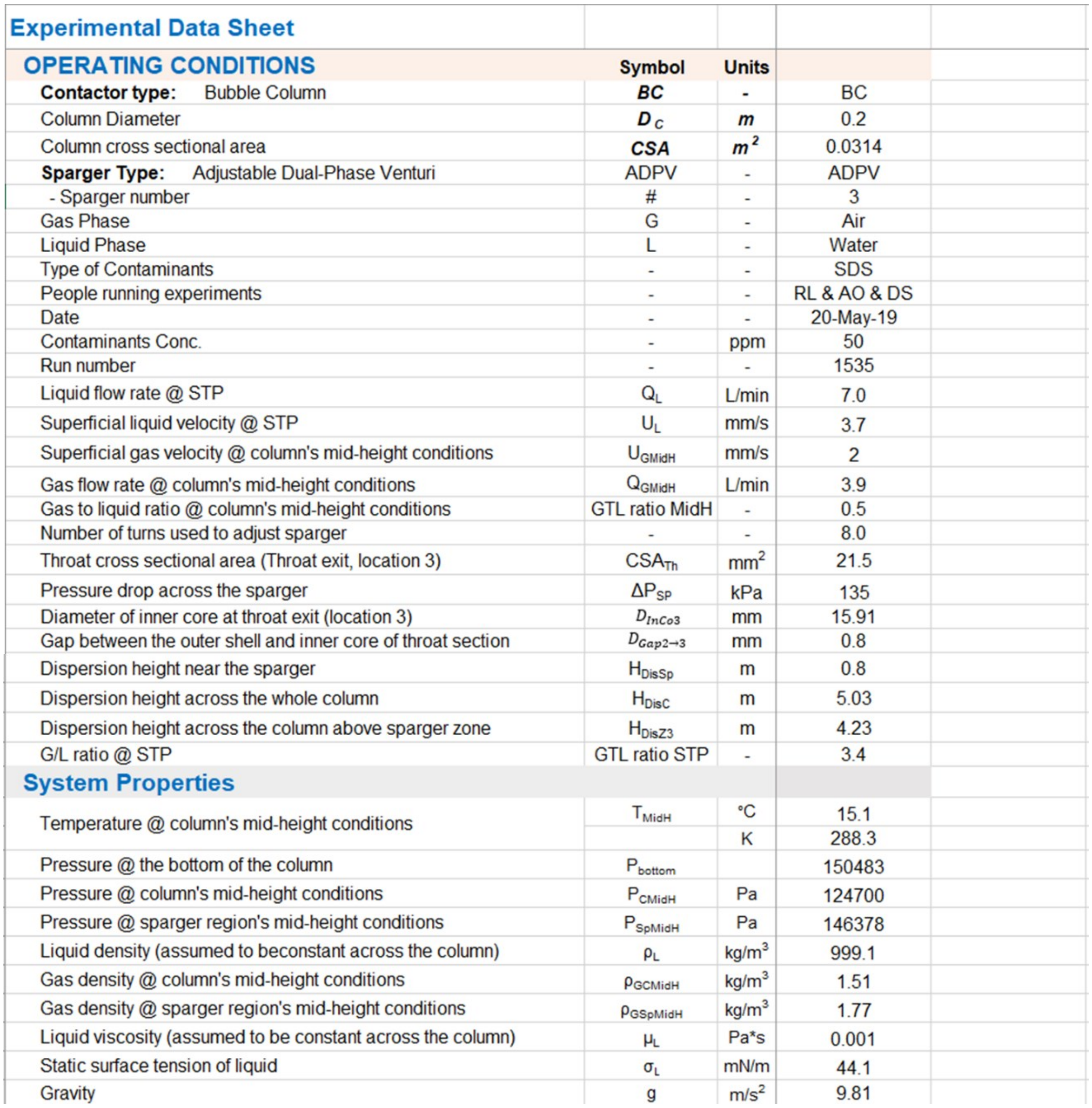

Experimental Data Sheet			
OPERATING CONDITIONS	**Symbol**	**Units**	
Contactor type: Bubble Column	***BC***	**-**	BC
Column Diameter	D_c	*m*	0.2
Column cross sectional area	***CSA***	m^2	0.0314
Sparger Type: Adjustable Dual-Phase Venturi	ADPV	-	ADPV
- Sparger number	#	-	3
Gas Phase	G	-	Air
Liquid Phase	L	-	Water
Type of Contaminants	-	-	SDS
People running experiments	-	-	RL & AO & DS
Date	-	-	20-May-19
Contaminants Conc.	-	ppm	50
Run number	-	-	1535
Liquid flow rate @ STP	Q_L	L/min	7.0
Superficial liquid velocity @ STP	U_L	mm/s	3.7
Superficial gas velocity @ column's mid-height conditions	U_{GMidH}	mm/s	2
Gas flow rate @ column's mid-height conditions	Q_{GMidH}	L/min	3.9
Gas to liquid ratio @ column's mid-height conditions	GTL ratio MidH	-	0.5
Number of turns used to adjust sparger	-	-	8.0
Throat cross sectional area (Throat exit, location 3)	CSA_{Th}	mm^2	21.5
Pressure drop across the sparger	ΔP_{SP}	kPa	135
Diameter of inner core at throat exit (location 3)	D_{InCo3}	mm	15.91
Gap between the outer shell and inner core of throat section	$D_{Gap2\rightarrow3}$	mm	0.8
Dispersion height near the sparger	H_{DisSp}	m	0.8
Dispersion height across the whole column	H_{DisC}	m	5.03
Dispersion height across the column above sparger zone	H_{DisZ3}	m	4.23
G/L ratio @ STP	GTL ratio STP	-	3.4
System Properties			
Temperature @ column's mid-height conditions	T_{MidH}	°C	15.1
		K	288.3
Pressure @ the bottom of the column	P_{bottom}		150483
Pressure @ column's mid-height conditions	P_{CMidH}	Pa	124700
Pressure @ sparger region's mid-height conditions	P_{SpMidH}	Pa	146378
Liquid density (assumed to beconstant across the column)	ρ_L	kg/m^3	999.1
Gas density @ column's mid-height conditions	ρ_{GCMidH}	kg/m^3	1.51
Gas density @ sparger region's mid-height conditions	$\rho_{GSpMidH}$	kg/m^3	1.77
Liquid viscosity (assumed to be constant across the column)	μ_L	Pa*s	0.001
Static surface tension of liquid	σ_L	mN/m	44.1
Gravity	g	m/s^2	9.81

APPENDIX C Typical Example of the Output Data Sheet for A Typical Run

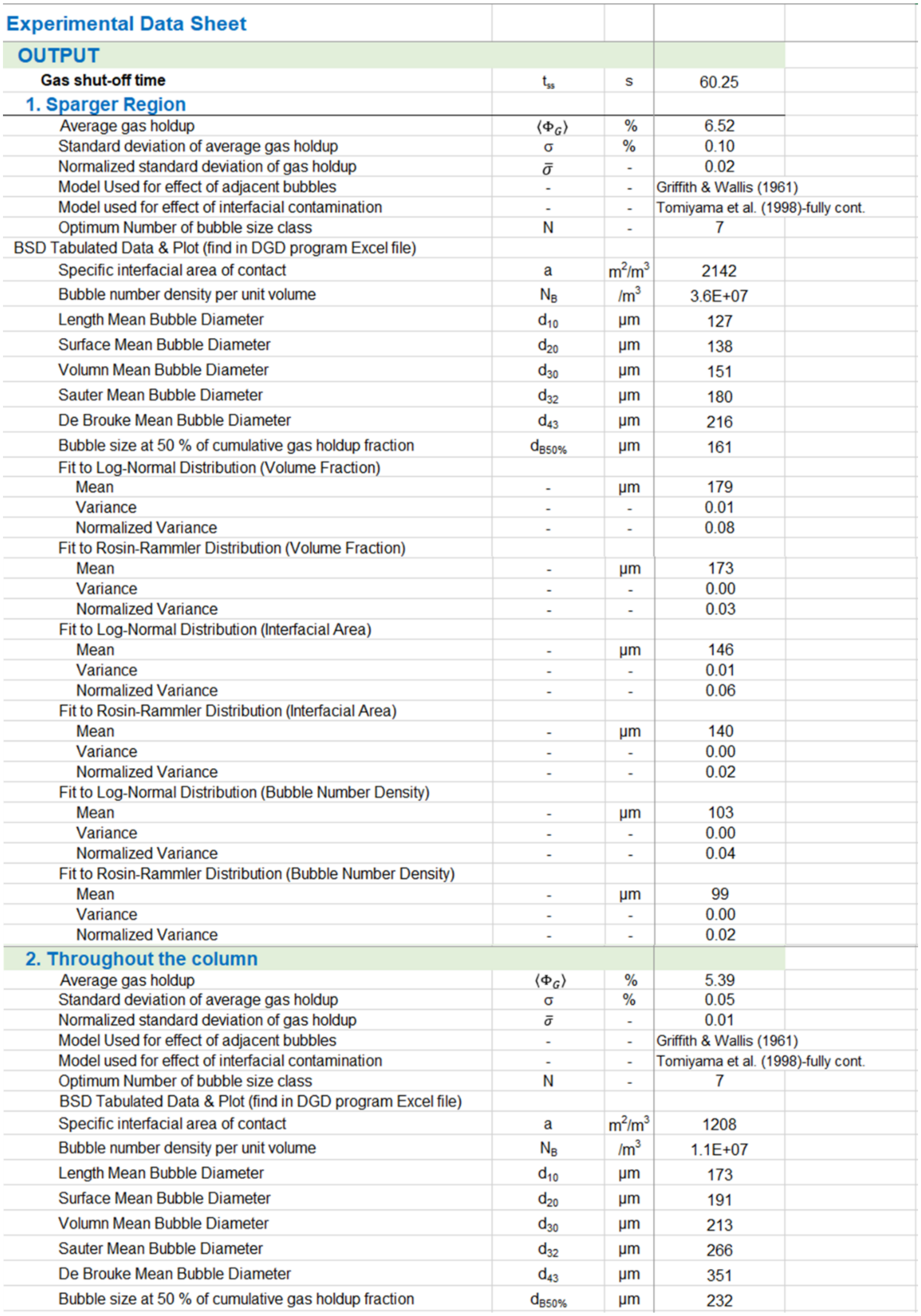

Experimental Data Sheet			
OUTPUT			
Gas shut-off time	t_{ss}	s	60.25
1. Sparger Region			
Average gas holdup	$\langle \Phi_G \rangle$	%	6.52
Standard deviation of average gas holdup	σ	%	0.10
Normalized standard deviation of gas holdup	$\bar{\sigma}$	-	0.02
Model Used for effect of adjacent bubbles	-	-	Griffith & Wallis (1961)
Model used for effect of interfacial contamination	-	-	Tomiyama et al. (1998)-fully cont.
Optimum Number of bubble size class	N	-	7
BSD Tabulated Data & Plot (find in DGD program Excel file)			
Specific interfacial area of contact	a	m^2/m^3	2142
Bubble number density per unit volume	N_B	$/m^3$	3.6E+07
Length Mean Bubble Diameter	d_{10}	μm	127
Surface Mean Bubble Diameter	d_{20}	μm	138
Volumn Mean Bubble Diameter	d_{30}	μm	151
Sauter Mean Bubble Diameter	d_{32}	μm	180
De Brouke Mean Bubble Diameter	d_{43}	μm	216
Bubble size at 50 % of cumulative gas holdup fraction	$d_{B50\%}$	μm	161
Fit to Log-Normal Distribution (Volume Fraction)			
Mean	-	μm	179
Variance	-	-	0.01
Normalized Variance	-	-	0.08
Fit to Rosin-Rammler Distribution (Volume Fraction)			
Mean	-	μm	173
Variance	-	-	0.00
Normalized Variance	-	-	0.03
Fit to Log-Normal Distribution (Interfacial Area)			
Mean	-	μm	146
Variance	-	-	0.01
Normalized Variance	-	-	0.06
Fit to Rosin-Rammler Distribution (Interfacial Area)			
Mean	-	μm	140
Variance	-	-	0.00
Normalized Variance	-	-	0.02
Fit to Log-Normal Distribution (Bubble Number Density)			
Mean	-	μm	103
Variance	-	-	0.00
Normalized Variance	-	-	0.04
Fit to Rosin-Rammler Distribution (Bubble Number Density)			
Mean	-	μm	99
Variance	-	-	0.00
Normalized Variance	-	-	0.02
2. Throughout the column			
Average gas holdup	$\langle \Phi_G \rangle$	%	5.39
Standard deviation of average gas holdup	σ	%	0.05
Normalized standard deviation of gas holdup	$\bar{\sigma}$	-	0.01
Model Used for effect of adjacent bubbles	-	-	Griffith & Wallis (1961)
Model used for effect of interfacial contamination	-	-	Tomiyama et al. (1998)-fully cont.
Optimum Number of bubble size class	N	-	7
BSD Tabulated Data & Plot (find in DGD program Excel file)			
Specific interfacial area of contact	a	m^2/m^3	1208
Bubble number density per unit volume	N_B	$/m^3$	1.1E+07
Length Mean Bubble Diameter	d_{10}	μm	173
Surface Mean Bubble Diameter	d_{20}	μm	191
Volumn Mean Bubble Diameter	d_{30}	μm	213
Sauter Mean Bubble Diameter	d_{32}	μm	266
De Brouke Mean Bubble Diameter	d_{43}	μm	351
Bubble size at 50 % of cumulative gas holdup fraction	$d_{B50\%}$	μm	232

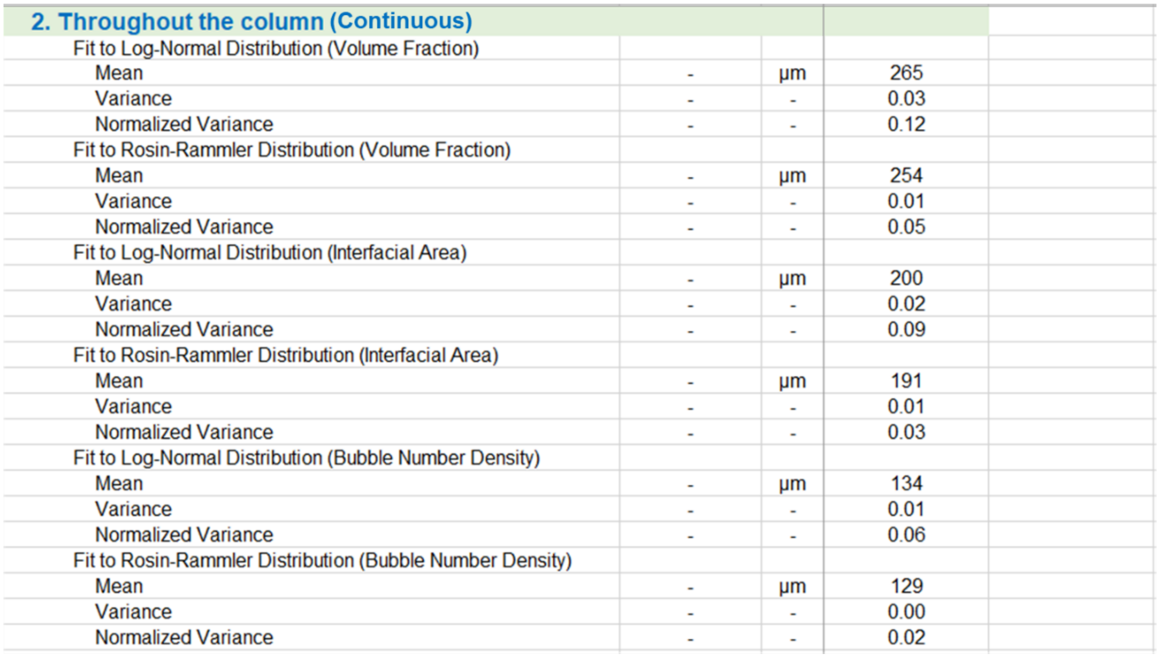

2. Throughout the column (Continuous)

Fit to Log-Normal Distribution (Volume Fraction)			
Mean	-	µm	265
Variance	-	-	0.03
Normalized Variance	-	-	0.12
Fit to Rosin-Rammler Distribution (Volume Fraction)			
Mean	-	µm	254
Variance	-	-	0.01
Normalized Variance	-	-	0.05
Fit to Log-Normal Distribution (Interfacial Area)			
Mean	-	µm	200
Variance	-	-	0.02
Normalized Variance	-	-	0.09
Fit to Rosin-Rammler Distribution (Interfacial Area)			
Mean	-	µm	191
Variance	-	-	0.01
Normalized Variance	-	-	0.03
Fit to Log-Normal Distribution (Bubble Number Density)			
Mean	-	µm	134
Variance	-	-	0.01
Normalized Variance	-	-	0.06
Fit to Rosin-Rammler Distribution (Bubble Number Density)			
Mean	-	µm	129
Variance	-	-	0.00
Normalized Variance	-	-	0.02

APPENDIX D Typical Halifax Water Composition

Table C.1 Typical Halifax water composition.

(www.halifaxwater.ca, Accessed on March 31, 2020)

TYPICAL ANALYSIS OF POCKWOCK LAKE & LAKE MAJOR WATER
2019 - 2020
(in milligrams per litre unless shown otherwise)
Note: All Regulatory Compliance Analysis are Processed by Third Party Laboratories

PARAMETERS	(Halifax) POCKWOCK		(Dartmouth) LAKE MAJOR		GUIDELINES FOR CANADIAN DRINKING WATER QUALITY	
	Raw Water	**Treated Water**	**Raw Water**	**Treated Water**	**Maximum Acceptable Concentration**	**Aesthetic Objective Concentration**
Alkalinity (as CaCO3)	**<5.0**	**18.0**	**<5.0**	**19.0**	**-**	**-**
Aluminum	**0.104**	**[A]0.088**	**0.197**	**[A]0.014**	**-**	**[A]0.20/0.10**
Ammonia (N)	**<0.050**	**<0.050**	**<0.050**	**<0.050**	**-**	**-**
Arsenic	**<0.001**	**<0.001**	**<0.001**	**<0.001**	**0.010**	**-**
Calcium	**1.0**	**4.3**	**1.0**	**14.0**	**-**	**-**
Chloride	**6.4**	**8.7**	**6.0**	**7.6**	**-**	**≤250**
Chlorate	**<0.10**	**<0.10**	**<0.10**	**<0.10**	**1.0**	**-**
Chlorite	**<0.10**	**<0.10**	**<0.10**	**<0.10**	**1.0**	**-**
Colour (True Colour Units)	**17.0**	**<5.0**	**39.0**	**<5.0**	**-**	**≤15.0**
Conductivity (µS/cm)	**32.0**	**72.0**	**32.0**	**110.0**	**-**	**-**
Copper (Total)	**0.0450**	**<0.0005**	**0.0537**	**0.0013**	**2.0**	**≤1.0**
Fluoride	**<0.10**	**0.52**	**<0.10**	**[B]0.49**	**1.5**	**-**
Hardness (as CaCO3)	**3.9**	**13.0**	**4.0**	**32.0**	**-**	**-**
HAA5 (avg.)	**-**	**0.014**	**-**	**0.028**	**0.080**	**-**
Iron (Total)	**0.03**	**<0.05**	**0.09**	**<0.05**	**-**	**≤0.3**

Langelier Index @ 4°C	-	-2.41	-	-1.97	-	-
Langelier Index @ 20°C	-	-2.16	-	-1.72	-	-
Lead (Total) (µg/l)	<0.50	<0.50	<0.50	<0.50	5.0	-
Magnesium	0.390	0.402	0.395	0.410	-	-
Manganese (Total)	0.022	0.015	0.053	<0.002	0.12	≤0.05
Mercury (µg/l)	<0.013	<0.013	<0.013	<0.013	1.0	-
Nitrate (as N)	<0.050	<0.050	<0.050	<0.050	10.0	-
Nitrite (as N)	<0.010	<0.010	<0.010	<0.010	1	-
pH (pH Units)	6.1	7.3	5.9	7.2	-	7.0 - 10.5
Potassium	0.230	0.290	0.250	0.240	-	-
Sodium	4.3	12.0	4.0	9.3	-	≤200
Solids (Total Dissolved)	31.0	57.0	31.5	84.0	-	≤500
Sulphate	3.2	8.8	3.2	28.0	-	≤500
Turbidity (NTU)	0.33	[C]0.06	0.39	[C]0.04	[C]0.15/0.2	-
Total Organic Carbon (TOC)	3.80	3.00	5.50	1.90	-	-
THM's (avg.)	-	0.027	-	0.039	0.100	-
Uranium (µg/l)	<0.10	<0.10	<0.10	<0.10	20.0	-
Zinc (Total)	<0.005	0.098	<0.005	0.088	-	≤5.0
PCB (µg/l)	<0.05	<0.05	<0.05	<0.05	-	-
Gross Alpha / Gross Beta (Bq/L)	<0.10/<0.10	<0.10/<0.10	<0.10/<0.10	<0.10/<0.10	0.5 /1.0	-

[A] Aluminum objective is related to type of plant filtration; the aluminum objective for direct filtration (Pockwock) is <0.20 mg/l and conventional filtration (Lake Major) is <0.10 mg/l.

[B] Fluoride was not being added to the finished water at the Lake Major WSP approximately 65% of the time due to system maintenance.

[C] The Pockwock and Lake Major plants analyze turbidity immediately post-filtration. Each filter must produce water with a turbidity of <0.15 NTU 95% of the time at the Pockwock Water Supply Plant and <0.20 NTU 95% of the time at the Lake Major Water Supply Plant. Both Water Supply Plants must produce water with a turbidity <1.00 NTU 100% of the time, as required by Provincial Permit.